NONLINEAR SEISMIC RESPONSE ANALYSIS OF HIGH-RISE FLAT PLATE BUILDINGS

by

Fatih Bilen

B.S., Civil Engineering, Boğaziçi University, 2015

Submitted to the Institute for Graduate Studies in
Science and Engineering in partial fulfillment of
the requirements for the degree of
Master of Science

Graduate Program in Civil Engineering

Boğaziçi University

2019

NONLINEAR SEISMIC RESPONSE ANALYSIS OF HIGH-RISE FLAT PLATE BUILDINGS

APPROVED BY:

Assoc. Prof. Kutay Orakçal (Thesis Supervisor)	……
Assoc. Prof. Serdar Soyöz	……
Prof. Alper İlki	……

DATE OF APPROVAL: 29.07.2019

To my family

ACKNOWLEDGEMENTS

Initially, I would like to thank my mother, Belgin Zent and my aunt, Hatice Bilen Buğra. This study would not have been possible without their endless support and their belief throughout my life.

I would like to express my sincere gratitude to my thesis supervisor Associate Professor Kutay Orakçal for his invaluable guidance and help during the preparation of this thesis.

I would like to thank Associate Professor Serdar Soyöz and Professor Alper İlki for participating in my thesis jury and for providing me with precious suggestions related to my study.

Also, I would like to express my special thanks to my friend Cem Tura for all his help and especially his initial suggestion to create the equivalent shear hinge model.

ABSTRACT

NONLINEAR SEISMIC RESPONSE ANALYSIS OF HIGH-RISE FLAT PLATE BUILDINGS

Modern seismic codes allow engineers to design high-rise flat plate buildings, together with an appropriate lateral load resisting system, in regions of high seismicity. Despite increased popularity and usage of the flat plate system in highly seismic zones, slab-column connection design checks are conducted only using a capacity design approach during the design process. Furthermore, nonlinear behavior of slab-column connections is ignored in performance-based design or assessment processes, due to limitations of commercial analysis programs. Therefore, this study was conducted to investigate nonlinear behavior characteristics of flat-plate systems, including slab flexural yielding in column strips, slab flexural yielding in the moment transfer ($c+5h$) region, and possible punching shear failure in the flat plate. In this study, nonlinear response history analyses are conducted on different 3D building model configurations. Slabs are represented using equivalent beam elements (effective beams) in three model configurations. Two additional nonlinear model configurations, one with rigid diaphragm constraints and without any slab elements, and the other with elastic slab elements, are generated as alternative solutions to effective beam modeling of slabs, for checking interstory drift ratios. Three effective beam models are created to compare different modeling and design approaches in various design codes including TEC 2018, ACI 318 and ASCE 41. The so-called overstrength factor is considered as key parameter in two of these models, where overstrength in calculation of slab punching stresses is included in the design process of one model, whereas it is neglected in the other. The last model is created according to design provisions of the new TEC 2018. The nonlinear analysis results show that all five models satisfy necessary strength, stiffness and ductility requirements, though they necessitate different slab reinforcement amounts at the slab-column connections. However, significantly larger column cross-sectional dimensions are required for the model designed according to TEC 2018.

ÖZET

KİRİŞSİZ DÖŞEMELİ YÜKSEK YAPILARIN DOĞRUSAL OLMAYAN DEPREM ANALİZİ

Çağdaş yönetmelikler mühendislere uygun yatay taşıyıcı sistemle beraber ileri deprem bölgelerinde kirişsiz döşemeli yüksek bina tasarlamalarına olanak sağlamaktadır. Kirişsiz döşemeli sistemlerin artan popülerliğine ve kullanımına rağmen, tasarım sürecinde döşeme kolon birleşimlerinin dizaynı ve kontrolleri sadece kapasite tasarımı ilkeleri ile yapılmaktadır. Ayrıca performansa dayalı tasarım sürecinde ve uygulamalarında kolon birleşimlerinin doğrusal olmayan davranışı da mühendislik programlarının yetersizliklerinden dolayı ihmal edilmektedir. Bu sebeple; kolon şeridindeki döşeme eğilme akmasını, moment transfer bölgesindeki ($c+5h$) döşeme eğilme akmasını ve döşemedeki zımbalamayı içeren kirişsiz döşeme sistemlerinin doğrusal olmayan davranışını incelemek için bu çalışma yapılmıştır. Bu çalışmada 3D modellere doğrusal olmayan deprem davranış analizi uygulanmıştır. Üç modelde döşeme elemanları, kiriş elemanları (eşdeğer kirişler) ile temsil edilmiştir. Elastik döşeme elamanı içermeyen rijit diyaframlı ve elastik döşemeli iki ekstra doğrusal olmayan model, eşdeğer kirişli modellere göreli kat ötelemeleri kontrolünde alternatif çözüm olması için oluşturulmuştur. TBDY 2018, ACI 318 ve ASCE 41 gibi farklı yönetmeliklerdeki modelleme ve tasarım yaklaşımlarını karşılaştırmak üzere üç eşdeğer kiriş modeli oluşturulmuştur. İki modelde dayanım fazlalığı önemli bir parametre olarak değerlendirilmiş ve dayanım etkisi bir modelde gözetilirken diğerinde gözetilmemiştir. Son model yeni TBDY 2018'e göre oluşturulmuştur. Modeller değişik donatı oranlarına sahip olmasına karşın, doğrusal olmayan davranış analizleri tüm modellerin gerekli dayanım, rijitlik ve şekil değiştirme koşullarını sağladığını göstermiştir. Fakat TBDY 2018'e göre tasarlanan modelde, yeterli koşulları sağlamak üzere önemli ölçüde daha büyük kolon kesitlerine ihtiyaç duyulmuştur.

TABLE OF CONTENTS

ACKNOWLEDGEMENTS iv
ABSTRACT v
ÖZET vi
LIST OF FIGURES x
LIST OF TABLES xv
LIST OF SYMBOLS xvii
LIST OF ACRONYMS/ABBREVIATIONS xxii
1. INTRODUCTION 1
1.1. General 1
1.2. Background 2
1.2.1. Flat Plate Systems 2
1.2.2. Performance Based Design of High-Rise Buildings 5
1.3. Research Significance 6
1.4. Objective and Scope of the Study 7
1.5. Organization of the Thesis 8
2. THEORY 9
2.1. General 9
2.2. Stiffness of Slab-Column Moment Frames 9
2.3. Slab Moment Transfer and Column Strip Widths 11
2.4. Eccentric Shear Stress Approach in Design 12
2.5. Strength of the Connection 15
2.6. Plastic Rotation Capacity of the Connection 17
2.7. Post Punching Behavior 19
3. MODELING APPROACH FOR SLAB-COLUMN CONNECTIONS 20
3.1. Description 20
3.2. Analytical Frame Model 21
3.2.1. Equivalent Shear Hinge Model 21
3.2.2. Frame Model Properties 24
3.3. Experimental Validation of the Frame Model Using Pushover Analysis 27
4. DESIGN, MODELING, AND ANALYSIS OF A PROTOTYPE TALL BUILDING 30

4.1. Structural Properties 30
4.2. Linear Elastic Modeling 32
4.2.1. Material Properties 33
4.2.2. Gravity Loads 34
4.2.3. Seismic Loads 34
4.2.4. Load Combinations 37
4.2.5. Seismic Masses 38
4.2.6. Structural Members 39
4.2.7. Damping 40
4.2.8. Model 40
4.3. Analysis Results and Design 43
4.3.1. Response Spectrum Analysis 43
4.3.2. Design of Slabs and Punching Shear Checks 43
4.3.2.1. Slab Design Based on Finite Element Analysis. 44
4.3.2.2. Eccentric Shear Stress Method. 47
4.3.3. Drift-Based Check and Comparative Evaluation 54
5. SEISMIC PERFORMANCE OF THE PROTOTYPE STRUCTURE 57
5.1. Nonlinear Modeling 57
5.1.1. Material Properties 57
5.1.1.1. Elastic Material for Fiber Sections. 57
5.1.1.2. Elastic Shear Modulus of Walls. 58
5.1.1.3. Elastic Modulus for Slabs 58
5.1.1.4. Concrete. 58
5.1.1.5. Reinforcement. 61
5.1.2. Gravity Loads 62
5.1.3. Seismic Loads 62
5.1.3.1. Determination of Target Spectrum. 62
5.1.3.2. Selection and Scaling of Earthquake Ground Motion Records. 63
5.1.4. Load Combinations 66
5.1.5. Masses 66
5.1.6. Modeling of Structural Elements 67
5.1.6.1. Structural Walls. 67
5.1.6.2. Columns. 67

5.1.6.3. Coupling Beams. 68
5.1.6.4. Elastic Slabs..... 69
5.1.6.5. Effective Slab-Beams. 69
5.1.7. Damping..... 70
5.1.8. Nonlinear Models..... 71
5.2. Analysis Method and Results 72
5.2.1. Nonlinear Response History Analysis Method..... 72
5.2.2. Nonlinear Response History Analysis Results 72
6. SUMMARY AND CONCLUSIONS 99
6.1. Overview 99
6.2. Conclusion..... 99
6.3. Future Recommendations..... 101
REFERENCES 102

LIST OF FIGURES

Figure 1.1. Floor plan and simplified model of the combined slab-column frame and core wall system (ATC 72-1, 2010). 4

Figure 2.1. Normalize effective stiffness factor for interior slab-column connection (ATC 72-1, 2010). 9

Figure 2.2. Effective slab width. 10

Figure 2.3. Application of effective width model (ATC 72-1, 2010). 11

Figure 2.4. Slab moment transfer and column strip widths. 12

Figure 2.5. Moment transfer at interior slab-column connection. 13

Figure 2.6. Moment transfer at corner slab-column connection 15

Figure 2.7. Modeling slab-column connection. 16

Figure 2.8. Failure mechanisms of slab-column connection. 17

Figure 2.9. Gravity shear ratios versus drift ratio at punching (Kang and Wallace, 2006). 18

Figure 2.10. Post-punching equilibrium. 19

Figure 3.1. Equivalent shear hinge model. 22

Figure 3.2. Kang's torsional hinge model and its force-deformation relationship. 23

Figure 3.3. Proposed equivalent shear hinge model and its force-deformation relationship. 23

Figure 3.4. Shake table test specimen (Kang *et al*., 2009). 24

Figure 3.5. Analytical frame model of the shake table test specimen in CSI Perform 3D. 26

Figure 3.6. Comparison of analytical pushover curves and experimental data for the slab-column frame specimen. 28

Figure 3.7. Comparison of failure mechanisms propagation. 29

Figure 4.1. 3D view of the structure. 30

Figure 4.2. Elevation view of the structure. 31

Figure 4.3. Normal floor plan view. 31

Figure 4.4. Basement floor plan view. 32

Figure 4.5. Design spectra for DD2 level earthquake ground motion. 37

Figure 4.6. 3D ETABS model. 40

Figure 4.7. First three mode shapes. (a) $T_{X,1}$; (b) $T_{Y,1}$; (c) $T_{B,1}$; (d) $T_{X,2}$; (e) $T_{Y,2}$; (f) $T_{B,2}$; (g) $T_{X,3}$; (h) $T_{Y,3}$; (i) $T_{B,3}$ 42

Figure 4.8. Shear stress under earthquake load increased by overstrength factor. 45

Figure 4.9. Moments in the X direction under factored gravity loads. 45

Figure 4.10. Moments in the X direction under earthquake loads. 46

Figure 4.11. Punching shear demand-to-capacity ratios. 46

Figure 4.12. Distribution of unbalanced moments at an interior column. 48

Figure 4.13. Distribution of unbalanced moments at a corner column. 50

Figure 4.14. Distribution of unbalanced moments at a corner column. 51

Figure 4.15. Distribution of unbalanced moments at corner column. 51

Figure 4.16. Distribution of unbalanced moments at a corner column. 53

Figure 4.17. Design story drift ratio versus gravity shear ratio. 56

Figure 5.1. Linearized stress-strain relationship of concrete. 60

Figure 5.2. Stress-strain relationship of reinforcement. 61

Figure 5.3. Target spectra for DD1 ground level motion. 63

Figure 5.4. Mean and target acceleration spectra for DD1 ground motion level. 65

Figure 5.5. Mean and target displacement spectra for DD1 ground motion level. 65

Figure 5.6. Columns modeling. 68

Figure 5.7. Modeling of coupling beams. 69

Figure 5.8. Modeling of effective slab-beam. 70

Figure 5.9. 3D views of models. 71

Figure 5.10. Plan views of models. 72

Figure 5.11. Control points of story drift ratios. 73

Figure 5.12. Interstory drift ratios for all models (a) D1-X, (b) D1-Y, (c) D2-X,(d) D2-Y. 74

Figure 5.13. Plastic rotations of coupling beam (a) Effbeam1, (b) Effbeam2, (c) Effbeam3. 75

Figure 5.14. Demand-capacity ratios of coupling beam (a) Effbeam1, (b) Effbeam2, (c) Effbeam3. 76

Figure 5.15. Structural wall names and locations. 77

Figure 5.16. Structural wall shear forces at (a) P01, (b) P04, (c) P05, (d) P07b, (e) P07c, (f) P08a, (g) P08c. 78

Figure 5.17. Strain measurement locations on floor plan. 80

Figure 5.18. Structural wall strains (a) SG01, (b) SG02, (c) SG09, (d) SG10, (e) SG17, (f) SG18, (g) SG19, (h) SG20. 81

Figure 5.19. Hinge name and locations at slab-column and slab-wall connections. 83

Figure 5.20. Rotations and demand/capacity ratios for effective beam model 1 (a) and (b) MH02, (c) and (d) MH04, (e) and (f) MH06, (g) and (h) MH07..... 84

Figure 5.21. Rotations and demand/capacity ratios for effective beam model 1 (a) and (b) MH12, (c) and (d) MH13. 86

Figure 5.22. Rotations and demand/capacity ratios for effective beam model 1 (a) and (b) SH03, (c) and (d) SH05. 87

Figure 5.23. Rotations and demand/capacity ratios for effective beam model 2 (a) and (b) MH02, (c) and (d) MH04, (e) and (f) MH06, (g) and (h) MH07..... 89

Figure 5.24. Rotations and demand/capacity ratios for effective beam model 2 (a) and (b) MH12, (c) and (d) MH13..... 91

Figure 5.25. Rotations and demand/capacity ratios for effective beam model 2 (a) and (b) SH03, (c) and (d) SH05. 92

Figure 5.26. Hinge names and locations for slab-column and slab-wall connections..... 93

Figure 5.27. Rotations and demand/capacity ratios for effective beam model 3 (a) and (b) MH02, (c) and (d) MH04, (e) and (f) MH07. 94

Figure 5.28. Rotations and demand/capacity ratios for effective beam model 3 (a) and (b) MH12, (c) and (d) MH13..... 96

Figure 5.29. Rotations and demand/capacity ratios for effective beam model 3 (a) and (b) MH03, (c) and (d) MH06, (e) and (f) MH08. 97

LIST OF TABLES

Table 2.1. Maximum allowable values for γ_f 14

Table 2.2. Modeling parameters and acceptance criteria for slab-column connections. . 18

Table 3.1. Dimensions and capacities of slab elements. 25

Table 3.2. Modeling parameters for the slab-column frame. 25

Table 3.3. Types and capacities of connections. 26

Table 4.1. Dimensions of members. 33

Table 4.2. Magnitude of uniform loads. 34

Table 4.3. Spectral acceleration coefficients for the prototype building under DD2 earthquake level 35

Table 4.4. Local soil effect coefficient for short period. 35

Table 4.5. Local soil effect coefficient for one second period. 36

Table 4.6. Design spectral acceleration coefficients. 36

Table 4.7. Load combinations. 38

Table 4.8. Live load contribution factor. 38

Table 4.9. Stiffness modifier of reinforced concrete elements. 39

Table 4.10. Fundamental periods and mass participation ratios. 41

Table 4.11. Governing design combinations. 44

Table 4.12. Slab reinforcement configurations. 52

Table 4.13. Gravity shear ratio details. 54

Table 5.1. Fiber modeling parameters for concrete material. 60

Table 5.2. Steel mechanical properties. 61

Table 5.3. Spectral acceleration coefficients for DD1 at hypothetical project location. . 62

Table 5.4. Design spectral accelerations for DD1 ground motion level. 63

Table 5.5. Ground motion properties for DD1 earthquake level. 66

Table 5.6. Performance limits for tension and compression strains on walls. 80

LIST OF SYMBOLS

A_s	Cross-sectional area of reinforcements
A_s	Cross-sectional area of longitudinal reinforcements
a_i	Spacing of two longitudinal bars for i^{th} pair
b_1	Edge dimension of punching perimeter in the direction of loading
b_2	Edge dimension of punching perimeter in the direction perpendicular to loading
b_o	Width of confined concrete core
b_{eff}	Effective slab width
c	Column width
c_1	Column width in the direction of the applied load
c_2	Column width perpendicular to the direction of the applied load
d	Effective depth
D	Overstrength factor
d_b	Average longitudinal reinforcement diameter in tension
E_c	Concrete tangent modulus of elasticity
E_{ce}	Effective elastic modulus of concrete
$E_d^{(H)}$	Horizontal earthquake load resultant of X and Y directions
$E_d^{(X)}$	Horizontal earthquake load in the X direction
$E_d^{(Y)}$	Horizontal earthquake load in the Y direction
$E_d^{(Z)}$	Vertical earthquake load
$(EI)_e$	Effective flexural rigidity of section
E_s	Modulus of elasticity of reinforcement
E_{sec}	Secant modulus of confined concrete at peak stress
F_1	Local soil effect coefficient for one second period
f_c	Compressive stress of confined concrete

f_{cc}	Compressive strength (peak stress) of confined concrete
f_{ce}	Expected compressive strength of concrete
f_{ck}	Characteristic compressive strength of concrete
f_{co}	Compressive strength of unconfined concrete
f_{ctd}	Design tensile strength of concrete
f_e	Effective confining pressure
f_{ex}	Effective confining pressure on X direction
f_{ey}	Effective confining pressure on Y direction
f_s	Stress of reinforcement
F_S	Local soil effect coefficient for short period
f_{sue}	Expected ultimate strength of reinforcement
f_{sy}	Yield strength of reinforcement
f_{sye}	Expected yield strength of reinforcement
f_{yw}	Yield strength of transverse reinforcement
g	Gravitational constant
G	Dead loads
G_c	Shear modulus of concrete
G_{ce}	Effective shear modulus of concrete
h	Slab thickness
H	Horizontal soil loads
h_{cb}	Depth of coupling beam
h_i	Height for i^{th} story
h_o	Height of confined concrete core
J	Moment of inertia of punching surface area about its geometric center
k_e	Confinement effectiveness coefficient
k_{ex}	Confinement effectiveness coefficient on X direction
k_{ey}	Confinement effectiveness coefficient on Y direction

l_1	Length of slab span in the direction of loading
l_2	Length of slab span in the direction perpendicular to loading
l_n	Clear length of slab span
L_p	Plastic hinge length
L_s	Shear span
$m_j^{(s)}$	Concentrated seismic mass at node j
M_{unb}	Unbalanced moment in the slab-column connection
M_y	Yield Moment
n	Live load contribution factor
N	Number of ground motion pairs
Q	Live loads
Q_e	Efficient live loads
q_u	Service load per unit area
r	Ratio of tangent modulus to difference of tangent and secant modulus
R	Structural system behavior factor
R_{JB}	Closest distance from project location to projection of rupture surface
s	Spacing of transverse reinforcement
S	Snow loads
S_1	Spectral acceleration coefficient for one second period
$S_{ae}(T)$	Elastic design spectral acceleration at period T
S_{aeR}	Spectral acceleration value of ground motion record
S_{aeT}	Spectral acceleration value of target spectrum
S_{D1}	Design spectral acceleration coefficient for one second period
S_{DS}	Design spectral acceleration coefficient for short period
S_S	Spectral acceleration coefficient for short period
S_S	Spectral acceleration coefficient for short period
T	Natural vibration period
T_A	Left corner spectrum period

T_B	Right corner spectrum period
T_L	Limit period for constant displacement range
T_p	Fundamental natural vibration period
u_p	Punching perimeter
v	Shear stress
v_c	Nominal shear stress resisted by concrete
$V_{s,30}$	Shear wave velocity at first 30 m depth of soil
v_u	Factored shear stress
v_{ug}	Factored shear stress due to gravity loads
V_{ug}	Factored shear force due to gravity loads
w_i	Weight of natural period
$w_j^{(S)}$	Concentrated seismic weight at node j
$w_{G,j}^{(S)}$	Concentrated seismic weight at node j from dead loads
$w_{Q,j}^{(S)}$	Concentrated seismic weight at node j from live loads
x	Ratio of any strain to strain at ultimate compressive strength of confined concrete
x_1	Distance from neutral axis of punching surface area to where shear stress is calculated
α	Effective width coefficient
α_{cb}	Angle between diagonal reinforcement and horizontal
β_{eff}	Effective stiffness factor for cracked section
γ_c	Unit weight of concrete
γ_f	Factor used to determine the moment transferred by slab flexure at slab-column connection
γ_v	Factor used to determine the moment transferred by eccentricity of shear at slab-column connection
Δ_i	Designed story drift at i^{th} story

ε_c	Confine concrete strain
$\varepsilon_c^{(CP)}$	Strain limit for collapse prevention
ε_{cc}	Strain at ultimate strength of confined concrete
ε_{co}	Strain at ultimate strength of unconfined concrete
ε_s	Strain at reinforcement
ε_{sh}	Starting strain of strain hardening
ε_{su}	Ultimate strain of reinforcing steel
ε_{sy}	Yielding strain of reinforcement
ε_t	Tensile strain in extreme layer of slab flexural reinforcement
θ	Angle between horizontal and bottom reinforcing steel
$\theta_p^{(CP)}$	Plastic rotation for collapse prevention limit
θ_y	Yield rotation
λ_c	Confined concrete strength modifier
ν_c	Poisson ratio of concrete
ρ_x	Ratio of transverse confining steel volume to volume of confined concrete core on X direction
ρ_y	Ratio of transverse confining steel volume to volume of confined concrete core on Y direction
$\sum X$	Sum of mass participation ratios on X direction
$\sum Y$	Sum of mass participation ratios on Y direction
ϕ	Strength reduction factor
ϕ_u	Ultimate curvature
ϕ_y	Yield curvature

LIST OF ACRONYMS/ABBREVIATIONS

3D	Three Dimensional
ACI	American Concrete Institute
ASCE	American Society of Civil Engineers
ATC	Applied Technology Council
CQC	Complete Quadratic Combination
CSI	Computers and Structures, Inc
CTBUH	Council on Tall Buildings and Urban Habitat
ESSM	Eccentric Shear Stress Method
FEM	Finite Element Method
HCR+	Above Critical Height
HCR-	Below Critical Height
LATBSDC	Los Angeles Tall Buildings Structural Design Council
MSE	Mean Squared Error
NLRHA	Nonlinear Response History Analysis
PBD	Performance-Based design
PEER	Pacific Earthquake Engineering Research Center
RSA	Response Spectrum Analysis
SRSS	Square Root of Sum of the Squares
TEC	Turkish Earthquake Code
TBI	Tall Buildings Initiative
TS	Turkish Standards

1. INTRODUCTION

1.1. General

Population growth rate is increasing every year all over the world. On the other hand, big cities have already reached their natural borders that force them not to expand their borders so that number of constructed high-rise buildings is increased. Besides of high rise building popularity, number of high-rise flat plate buildings itself is increased because of advantages (e.g., cost and functional) of the flat plate systems. Architects' preference to see smooth ceiling rather than ceiling divided with beams into small pieces is another advantage of flat plate systems.

In flat plate systems, slab-column assemblies are typically not used to resist earthquake loads in high seismic zones but are rather designed to support gravity loads. Therefore, slab-column connection design (detailing) needs to guarantee that frames are able to carry gravity loads while the structure is resisting earthquake actions (Moehle, 2015).

Slab-column frames are difficult to model due to the variety of potential failure mechanism at slab-column connections. Failure can be in the so-called "column strip" region, or within the so-called slab "moment transfer" region, or it can be simply punching shear failure along the punching perimeter. Moreover, nonlinear behavior characteristics (e.g., ductility) of the connection is dependent on the gravity-induced punching shear stress demand. Additional factors that make modeling of the slab-column connections complex are the type of connection (e.g., interior, edge and corner), and punching shear reinforcement usage. Today, engineers have access to powerful tools to model and analyze complicated building systems; however, even modern analysis tools are not able to deal with the difficulties in slab-column connection modeling (Kang *et al*., 2009).

The most typical example of this shortcoming is that the commonly-used nonlinear analysis software for tall buildings, CSI Perform3D, does not have torsional link element, which is necessary to simulate the nonlinear behavior of the slab-column connection.

Therefore, in this study, a novel modeling approach is proposed, which is based on representation of a nonlinear torsional link at a slab-column connection, using an equivalent approach that involves an assembly of eccentrically-configured nonlinear shear links. To validate the modeling approach, a two bay plane frame model configuration is first generated using the novel so-called equivalent shear hinge model, and pushover analysis results obtained using the model are compared with experimental results obtained from the literature on a slab-column assembly. After validation of equivalent shear hinge model against prior experimental studies, a realistic 20 storey flat plate building configuration with two basement floors is modeled using the same approach, and is investigated as a case study to evaluate the effect of different slab-column connection configurations on the seismic performance of a tall building configured using different design approaches for the slab-column connections. For the benchmark building, response spectrum analysis is first used to design the structure (linear elastic design) using the finite elements analysis program CSI ETABS. Then, two similar nonlinear models of the structure are generated; one with rigid diaphragms at story levels and the other with elastic shell elements for the slabs. Afterwards, three additional nonlinear model configurations, all with effective beam elements for representing the slabs and with the equivalent shear hinge models at the slab-column connections are generated, representing three different code-compliant design approaches (ACI318 design, ACI318 design considering seismic overstrength, and TEC2018 design) for comparison of building performance. The commonly-used CSI Perform3D software is used to construct all of the nonlinear model configurations and to perform nonlinear response history analyses of the benchmark building. Nonlinear analysis results are interpreted for comparative evaluation of the three design approaches for the slab-column connections.

1.2. Background

1.2.1. Flat Plate Systems

Flat plate system notion was developed during the first years of the 20th century. However, detailed experimental and analytical studies on the nonlinear seismic behavior of slab-column connections were not carried out until very recently. The most relevant studies

in the literature are outlined below. A more detailed evaluation of the recent research studies will be presented in the following chapter of this thesis.

One of earliest studies on calculating the capacity of a slab-column connection due to unbalanced moment in the columns, which is called the eccentric shear stress method, is presented by Stasio and Buren (1960). Later, experimental studies were conducted to develop the eccentric stress method by Hanson and Hanson (1968). This eccentric stress method is still used to calculate capacity of slab-column connections.

An extensive study that emphasizes the nonlinear seismic behavior flat plate frames is performed Kang (2004). Analytical studies of reinforced and post-tensioned concrete flat plate are compared with shake table test of one third of two stories and two-by-two bay slab column structure. The study provides valuable data on slab-column connection behavior under reversed cyclic loads and is a comprehensive study that has led researchers towards generating new modeling methodologies for slab-column connections.

Another experimental study is conducted by Kang and Wallace (2006), where the purpose of the experiments is to show a relationship between gravity punching shear ratios and interstory drift ratios at punching failure. This is a significant study that was used to build backbone curves for slab-column connections in performance assessment guidelines.

Kang *et al.* (2009) presents a comparison of a proposed analytical modeling approach (using nonlinear torsional springs at slab-column connections) with experimental data on slab column frames. This study is significant towards development of reliable modeling approach for slab-column connections. However the developed modeling approach is applied on a simple two-story two-bay slab-column plane frame, and nonlinear static and dynamic analyses are conducted. Therefore, extension of the work is necessary for complex and 3D structures, which is the scope of the present study.

In addition to these studies mentioned in the prior paragraphs, there are various guidelines and standards that address modeling of slab-column frame components and connections. Modeling and Acceptance Criteria for Seismic Design and Analysis of Tall Buildings (ATC 72-1) (Applied Technology Council, 2010) involves case studies for flat

plate buildings with core walls. This report is a significant document for structural engineers. However, to create a simplified model, equivalent slab-beams and equivalent columns are used, which is not possible for more complicated structural configurations (Figure 1.1). In addition to ATC 72-1, Seismic Evaluation and Retrofit of Existing Buildings (ASCE/SEI 41-17) (American Society of Civil Engineers, 2017) is a standard that covers topics such as modeling approaches for representing the stiffness and strength characteristics of slab column moment frames..

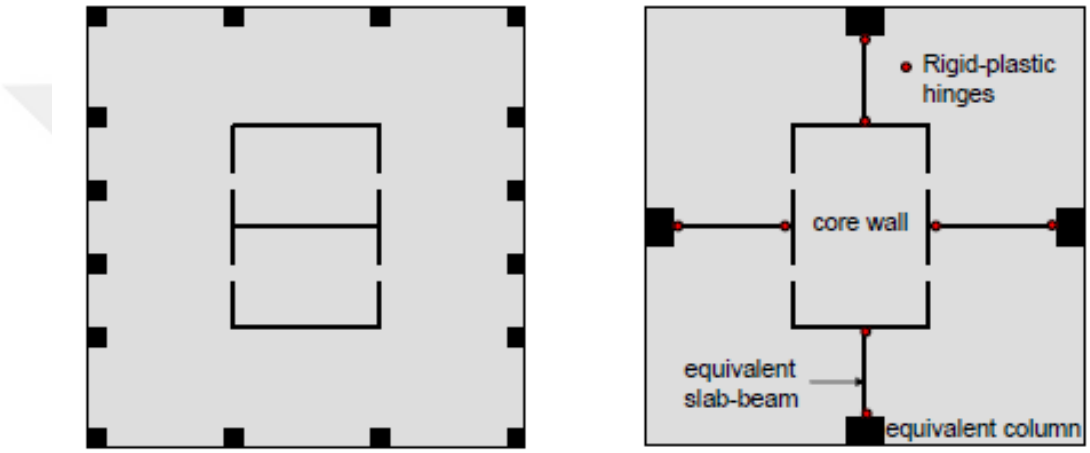

(a) (b)

Figure 1.1. Floor plan and simplified model of the combined slab-column frame and core wall system (ATC 72-1, 2010).

The new Turkish Earthquake Code (TEC 2018) (Disaster and Emergency Management Presidency, 2018) and Building Code Requirements for Structural Concrete and Commentary (American Concrete Institute Committee, 2011) specify different flat plate design approaches, although design can be done using either the finite element method or assuming an eccentric stress method in both codes. The major differences in the design approaches in TEC 2018 and ACI 318-15 are related to (i) consideration of seismic overstrength in design, and (ii) transfer of unbalanced moment at the exterior slab-column connections through slab flexural reinforcement only, as will be described in detail in the next chapter.

1.2.2. Performance Based Design of High-Rise Buildings

Presently, engineers are more capable of producing better designs while spending less computational time with the impact of technological development. Recent advances in technology forces us to renew current design approaches to reach safer and more cost-efficient design. The so-called performance-based design approach objective is to design and analyze tall buildings with predictable and realistic performance under earthquake actions, through nonlinear response history analyses. However, reliable design using the PBD approach depends on how realistic and reliable are the modeling approaches used in analysis. Therefore, there are guidelines and documents to assist structural engineers in modeling of the expected nonlinear behavior of structural members, as well as criteria on assessment of performance levels based on nonlinear deformation levels obtained from analysis results.

Well-known modern PBD documents and guidelines include An Alternative Procedure for Seismic Analysis and Design of Tall Buildings Located in the Los Angeles Region (LATBSDC 2015) (Los Angeles Tall Buildings Structural Design Council, 2015), Recommendations for the Seismic Design of High-Rise Buildings (CTBUH 2008) (Council on Tall Buildings and Urban Habitat, 2008), and Guidelines for Performance Based Seismic Design of Tall Buildings (PEER-TBI2010) (Pacific Earthquake Research Center, 2010). All of these documents include general recommendations on the performance-based design process of high-rise buildings, whereas detailed information on the topic is presented in the Advanced Technology Council Report ATC 72-1 (Applied Technology Council, 2010).

LATBSDC 2015 is published to describe the PBD approach that is recommended to be used for tall buildings in the Los Angeles region. The document is applicable for all type buildings but it is written for especially for tall buildings higher than 160 feet (49 m) from average adjacent ground surface. Adequacy of design can be shown according to the document, if the structure exhibits serviceable behavior under frequent earthquakes and low probability of collapse under extremely rare earthquakes.

PEER-TBI 2010 is another significant document related to the PBD approach. The document covers similar content with LATBSDC 2105. However, the purpose of this guideline is to provide more detailed resources for structural engineers related to the PBD approach for tall buildings.

CTBUH 2008 is another relevant document that aims to set out best-practice principles for seismic design of high rise buildings for various levels of seismic hazard. The document also presents brief information on foundation effects, seismic hazard assessment, and use of energy dissipation components in addition to structural modeling and analysis procedures.

The ATC 72-1 report is a more comprehensive resource related to the PBD approach. The report contains detailed information on topics ranging from general nonlinear modeling concepts (e.g., P-delta effects, damping etc.) to more specific modeling methodologies for structural members (e.g., beams, columns, walls etc.). The report is also crucial in the context of this study, because it also includes details on modeling of slab-column frame component.

The new Turkish Earthquake Code includes a chapter on PBD of tall building systems subjected to earthquake actions. That chapter includes similar subjects with other codes. In TEC 2018, PBD is mandatory for structure that exceeds 70 m in high seismic zones.

1.3. Research Significance

Flat plate buildings are nowadays very common structural systems located in all types of seismic zones. A flat plate floor system is typically not designed a lateral force resisting system; however it has maintain its capacity to resist gravity loads safely under large earthquake-induced displacements. Therefore, the nonlinear seismic behavior and deformation capacity of slab-column frames and connections are still important. However, nonlinear behavior of slab-column assemblies are typically not considered in performance-based design applications, due to incapability of commercial nonlinear analysis programs to simulate their seismic behavior, even for simple floor plan configurations. To conduct a

more reliable seismic performance assessment for such systems, introduction of a new and efficient modeling approach for flat plate systems are essential. Furthermore, in the design phase of slab-column connections based on linear elastic analysis results, although slab-column connection design is generally conducted using an eccentric shear stress approach in all modern design codes, there are still uncertainties in and variations between code requirements including whether or not to consider seismic overstrength in design and how to design exterior slab-column connections. Therefore, development of a nonlinear modeling and performance assessment approach for slab-column connections is also necessary to evaluate these uncertainties in code-compliant design approaches, so that necessary improvements can be made on the design code specifications.

1.4. Objective and Scope of the Study

The first purpose of this study is to propose a new modeling method, which is applicable for implementation in commercial nonlinear analysis software, in order to simulate the stiffness, strength, and ductility characteristics of slab-column assemblies in flat plate buildings, to better capture the nonlinear seismic response attributes of such structures, and to identify possible failure modes at the slab-column connections. A novel and simple modeling approach is proposed, and is validated against with existing experimental data presented in the literature. The second objective is to use the proposed modeling approach in nonlinear seismic performance assessment of a realistic building configuration, for comparing the adequacy of alternative designs based on different seismic codes, with emphasis on slab and slab-column connection design. Within the scope of this work, a total of five nonlinear models (in CSI-Perform 3D software) of a high-rise building with flat plate floor system are generated. Two of the models, one with a rigid diaphragm constraint at the story levels (without and slab elements) and the other with elastic slab elements with cracked section modulus, are constructed as industry-standard model configurations for checking interstory drift ratios. Then, three additional models are generated, in which slabs are represented by effective beam elements and the slab-column connections are modeled using the proposed modeling approach in this study. The slab-column connections in these three model configurations are designed based on three different seismic code approaches, the first of which is the ACI318 approach, the second is the ACI318 considering also seismic overstrength, and the third is the TEC2018 approach.

Nonlinear response history analysis is conducted on all five models, and significant response quantities (e.g., story drift ratios, plastic rotation demand-to-capacity ratios at the slab-column connection hinges, wall shear forces, wall longitudinal strains, etc.) obtained from analysis results are compared with each other.

1.5. Organization of the Thesis

This Thesis comprises six chapters. In Chapter 1, general information on the topic is provided, together with the objectives and scope of this study. Relevant theory, concepts, terms, and definitions are described in Chapter 2. The proposed nonlinear modeling approach for slab-column connections is presented in Chapter 3, together with experimental validation of the modeling approach against experimental data obtained from the literature on shake-table testing of a slab-column frame specimen. Linear elastic analysis and different code-compliant designs of a prototype flat plate building structure are presented in Chapter 4. The nonlinear modeling and nonlinear response history analysis procedures conducted for the building structure, as well as comparative evaluation of the analysis results are provided in Chapter 5. Finally, concluding remarks and suggestions for future studies are presented in Chapter 6.

2. THEORY

2.1. General

In this chapter, relevant theory, concepts, terms, and assumptions on the stiffness, strength, nonlinear behavior, and deformation capacity of slab-column frames, as well as, frequently-used design procedures and equations are presented, to clarify the conceptual issues related to the behavior and design of slab-column assemblies and connections.

2.2. Stiffness of Slab-Column Moment Frames

To obtain a reliable nonlinear response prediction of a structure, the analytical model of the structure should be as realistic as possible, ideally with all the structural members included in the model. Allen and Darvall (1977) suggest using effective beam elements instead of using plate elements to represent slabs rigidity in analytical models. Their study shows that the stiffness of slab is dependent on column width to slab span ratio (c_1 / l_1) and slab aspect ratio (l_1 / l_2) (Figure 2.1). Later, Equations 2.1 and 2.2 are developed for interior and exterior connections respectively by Hwang and Moehle (2000).

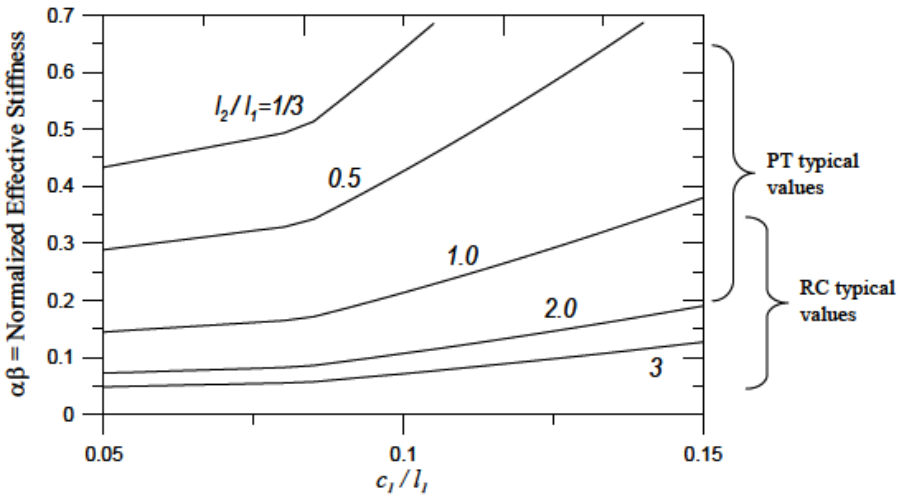

Figure 2.1. Normalize effective stiffness factor for interior slab-column connection (ATC 72-1, 2010).

$$\alpha l_2 = 2c_1 + \frac{l_1}{3} \tag{2.1}$$

$$\alpha l_2 = c_1 + \frac{l_1}{6} \tag{2.2}$$

Effective stiffness factor (β_{eff}) should be also applied for cracking due to temperature and shrinkage. Effective stiffness factor for a cracked section can be taken as $1/3$ or calculated with Equation 2.3 (Hwang and Moehle, 2000). In the end, effective slab width (b_{eff}) can be expressed in Equation 2.4 and Figure 2.2 to represent slab elements.

$$\beta_{eff} = 4c_1/l_1 \geq 1/3 \tag{2.3}$$

$$b_{eff} = \alpha\beta l_2 \tag{2.4}$$

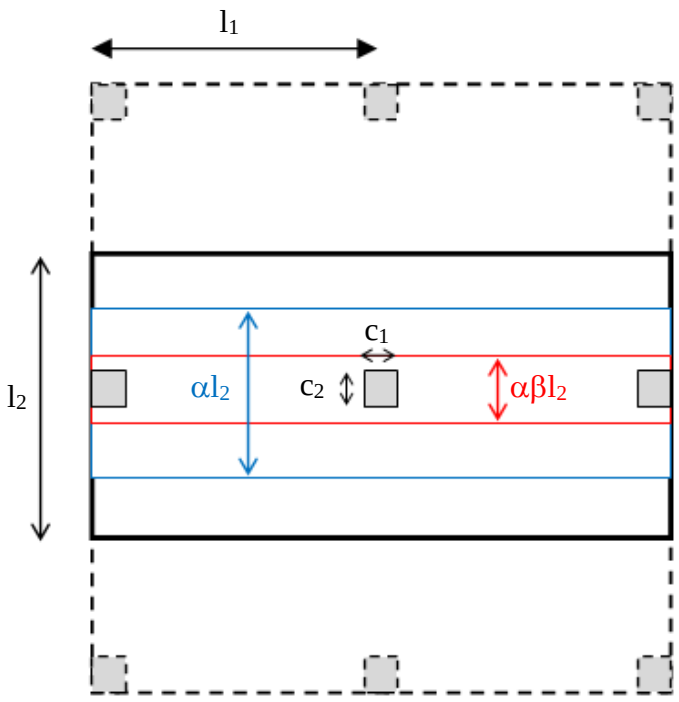

Figure 2.2. Effective slab width.

There is no confirmed formulation on determination of effective beam width for slab-wall connections. However, a suggestion exists in an example in ATC 72-1 (Applied Technology Council, 2010). Effective width coefficient (α) is taken as 1 in the wall's weak direction in that example (Figure 2.3). And the coefficient varies between 0.5 and 0.75 for RC slab-column connections. Based on the reasoning that the effective width coefficient must be larger for slab-wall connections, in this thesis, the coefficient is taken as 0.75 (upper limit for slab-column connections) in the wall's strong direction and 1.0 in the wall's weak direction.

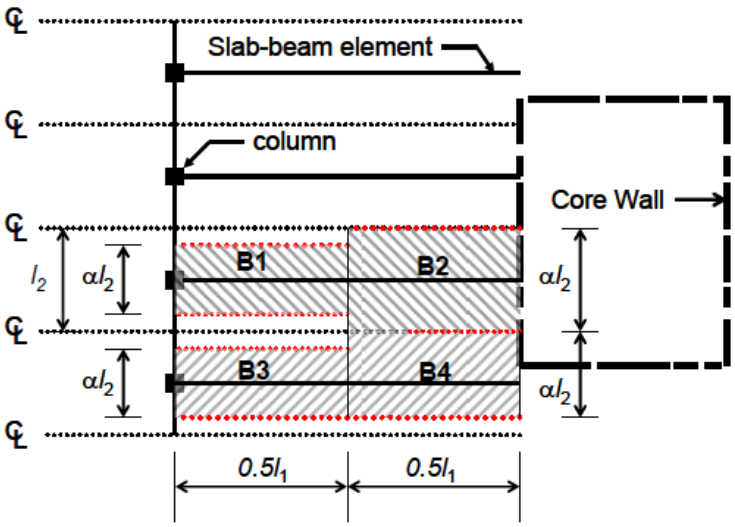

Figure 2.3. Application of effective width model (ATC 72-1, 2010).

2.3. Slab Moment Transfer and Column Strip Widths

A column strip is defined as sum of the slab widths on each side of a column lesser of $0.25l_2$ and $0.25l_1$, where the column strip should be able to resist moment under gravity loads and earthquake loads at the slab support (Figure 2.4). On the other hand, a portion of the unbalanced moment developing at the two consecutive column end sections (top section of lower story column and bottom section of and lower story column) is transferred to the slab by the so-called slab "moment transfer width" ($c_2 + 5h$ for interior, $c_2 + 2.5h$ exterior connections) (ACI 318M-14, 2015).

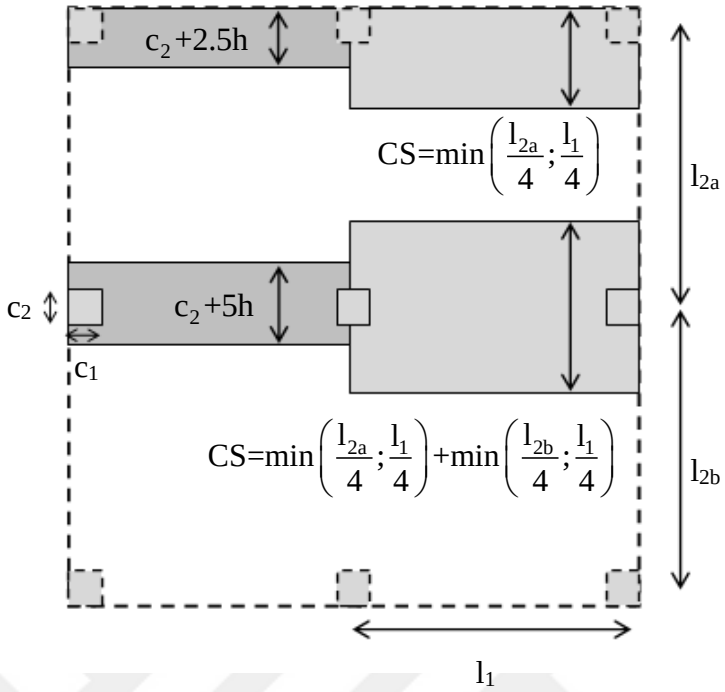

Figure 2.4. Slab moment transfer and column strip widths.

2.4. Eccentric Shear Stress Approach in Design

The so-called "eccentric shear stress" procedure is first introduced by Stasio and Buren (1960). In this method, the unbalanced moment at the connection is transferred as the sum of linearly distributed shear stresses in the slab along the punching perimeter, and the bending moment in the on slab within the moment transfer width (Figure 2.4). Unbalanced moment equals to the difference (or sum) of moments at bottom column end above the connection and at the top column end below the connection, if the signs of the column moments are the same (or different). The axis along which slab shear stress is equal to zero is assumed to pass through the geometric centroid of the punching surface area ($u_p d$). The connection thus satisfies total moment equilibrium. The portions by which the unbalanced moment will be transferred as bending moment to the slab within the moment transfer region and as moment resultant of shear stresses in the slab along the punching surface are described using empirical factors γ_f and γ_v. Therefore, $\gamma_f M_{unb}$ equals to the sum of the adjacent slab moments, $M^{+}_{u,c+5h}$ and $M^{-}_{u,c+5h}$, whereas $\gamma_v M_{unb}$ equals to the moment resultant of the distributed shear stresses in the slab about the

geometric centroid of the punching surface area. The factors' formulations are provided below:

$$\gamma_f = \frac{1}{1+\frac{2}{3}\sqrt{\frac{b_1}{b_2}}} \tag{2.5}$$

$$\gamma_v = 1-\gamma_f \tag{2.6}$$

Maximum shear stress can be calculated as sum of shear stresses due to gravity load and shear stress due to the portion of the unbalanced moment, by Equation 2.7 (Figure 2.5). Earthquake effect is not one-directional; therefore to consider the effect in the other direction, unbalanced moment from earthquake loading in the other direction needs to be also considered using the equation below.

$$v_u = \frac{V_{ug}}{u_p d} \pm \frac{\gamma_v M_{unb} x_1}{J}\left[\pm \frac{\gamma_v M_{unb} x_1}{J}\right] \text{ (For earthquake loading in } x \text{ and y directions)} \tag{2.7}$$

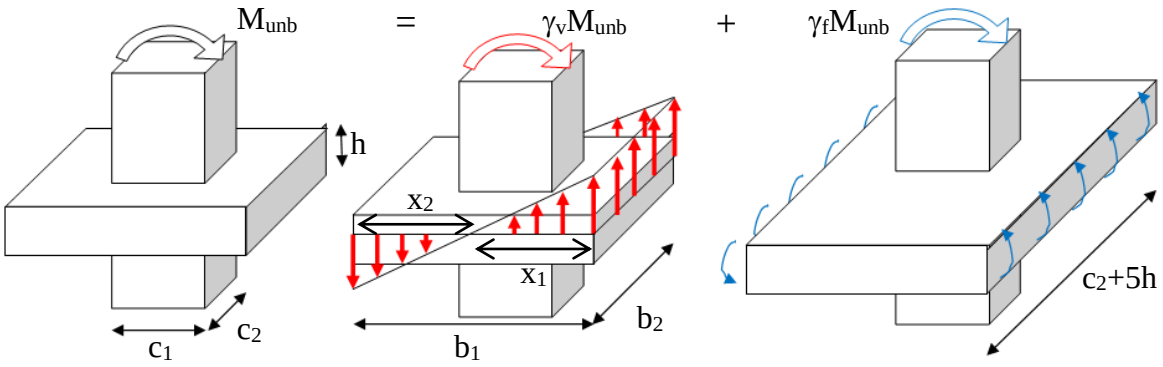

Figure 2.5. Moment transfer at interior slab-column connection.

Where, x and J are calculated for interior connections using Equations 2.8 and 2.9.

$$x_1 = x_2 = b_1/2 \tag{2.8}$$

$$J = 1/6 b_1^3 d + 1/6 b_1 d^3 + 1/2 b_1^2 b_2 d \quad (2.9)$$

The eccentric shear stress method can be applied easily to interior column connections. However, for edge column connections in the perpendicular direction to the edge and for corner column connections, excessive shear stresses may be calculated using the model, due to the shifted centroidal axis of punching surface area (Figure 2.6). In such cases, using punching shear reinforcement at the connection, increasing the slab thickness, or increasing column dimensions may be solutions to reduce the excessive stress demand to the concrete design tensile strength. However, in most cases, these shear stress demands are too excessive to reach a feasible design.

There is another way to deal with this design problem addressed in ACI 318M-14 (2015). For edge or corner column connections, γ_f is permitted to be modified up to a value of 1.0 under certain conditions, which means the total unbalanced moment is going to be resisted only by flexural reinforcement in the slab, within the moment transfer width ($c_2 + 2.5h$ for corner connection) when γ_f is taken as 1.0 in design calculations. Therefore, since the γ_v value is zero, none of the unbalanced moment is transferred as shear stresses in the slab, meaning that punching shear check in the slab is not necessary. However, this can be applied when the gravity load induced punching shear stresses are limited and tensile strain at extreme layer of slab flexural reinforcement (ε_t) in slab at nominal strength is also more than limits to design under reinforced sections for providing required ductility at slab-column connections. The limitations are presented in Table 2.1.

Table 2.1. Maximum allowable values for γ_f.

Column Location	Span Direction	V_{ug}	ε_t (within slab transfer width)	Maximum Modified γ_f
Corner Column	Either Direction	$\leq 0.5\phi V_c$	≥ 0.004	1.0
Edge Column	Perpendicular to the Edge	$\leq 0.75\phi V_c$	≥ 0.004	1.0

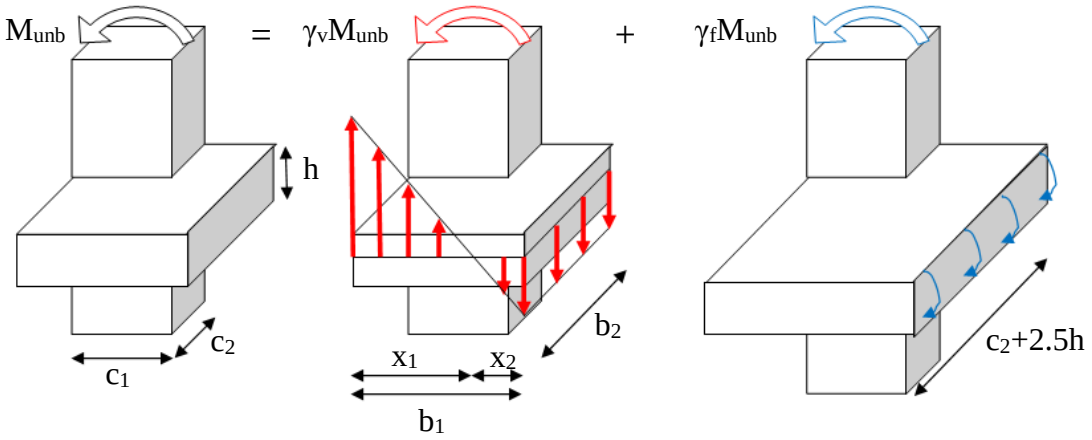

Figure 2.6. Moment transfer at corner slab-column connection

2.5. Strength of the Connection

Slab-column connections can be modeled using a combination of column strip (CS) hinges in the slabs and torsional hinges at the connections. CS hinges are placed at the end of the effective beam ends to represent nonlinear slab behavior. Punching shear failure and/or failure due to bending within the $c+5h$ width is represented using a torsional hinge that connects the "beam intersection joint" to the "column intersection joint" for simulating the nonlinear behavior of connection (Figure 2.7). In this section, three different failure mechanisms defined for the slab-column connection are discussed, which are called inappropriate design (punching failure), weak connection (flexural yielding in the $c+5h$ region), and strong connection (flexural yielding of the column strip).

If the unbalanced moment capacity M_{unb}, which is calculated using Equation 2.10 (corresponding to punching shear failure), is smaller than the sum of two adjacent slab moment transfer width capacities (only one in exterior connection) divided by γ_f, then connection design is inappropriate to exhibit ductile deformation and is susceptible to punching shear failure. On the other hand, in a weak connection, sum of the two adjacent (only one in exterior connection) CS moment capacities is higher than M_{unb} calculated from Equation 2.11 (or Equation 2.12). However, M_{unb} calculated from Equation 2.11 or 2.12 is less than that calculated from Equation 2.10. Finally, in a strong connection, the

total moment capacity of the CS hinges does not exceed the either the M_{unb} capacity calculated from Equation 2.11 (2.12) or the M_{unb} calculated from Equation 2.10.

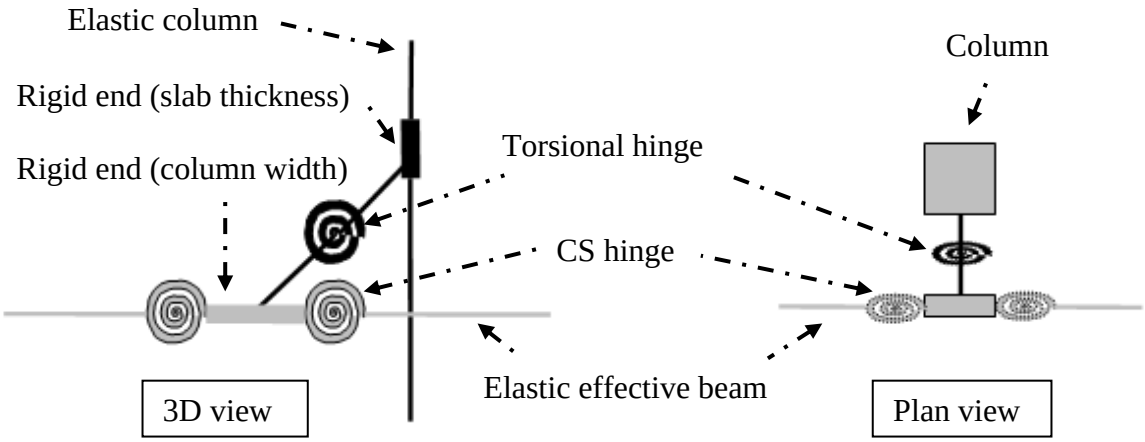

Figure 2.7. Modeling slab-column connection.

$$M_{unb,v} = \left(v_c - \frac{V_g}{u_p d} \right) \frac{J}{\gamma_v x} \tag{2.10}$$

$$M_{unb,f} = \frac{M^{+}_{c+5h} + M^{-}_{c+5h}}{\gamma_f} \qquad \text{for interior connections} \tag{2.11}$$

$$M^{\pm}_{unb,f} = \frac{M^{\pm}_{c+5h}}{\gamma_f} \qquad \text{for exterior connections} \tag{2.12}$$

The behavioral modeling method described in the prior paragraphs is conceptually applicable. However, in commercial analysis programs (e.g., CSI Perform 3D), using both CS hinges in the slabs and torsional hinges at the connections tends to provide erroneous analysis results due to software incapabilities. In CSI Perform 3D for example, when one of plastic hinges at the connection reaches capacity, the remaining hinges continue to transfer increased moment, whereas equilibrium dictates that they should not. Therefore, using only torsional hinges that represent the controlling nonlinear behavior characteristics

of the connection is a more practical approach for modeling and analysis, as also recommended in ASCE 41-17.

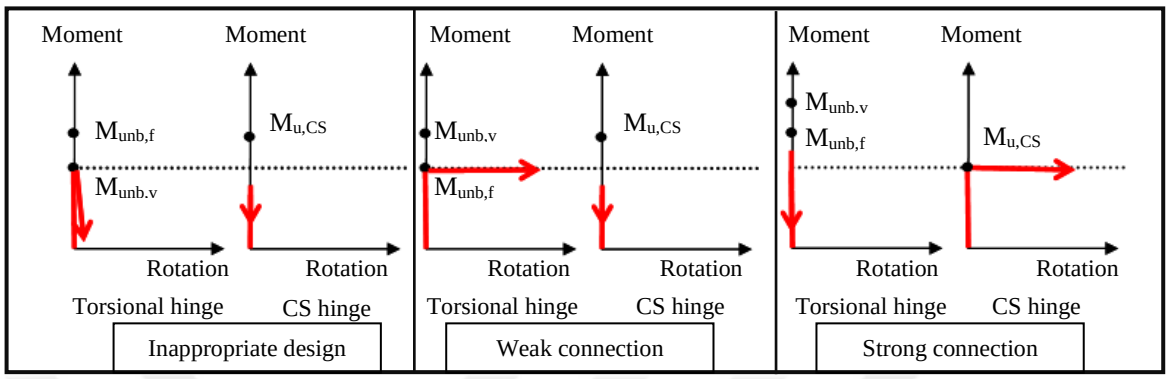

Figure 2.8. Failure mechanisms of slab-column connection.

2.6. Plastic Rotation Capacity of the Connection

Punching shear failure under earthquake actions has been shown to be dependent on not only shear stresses developing in the slab (realistic calculation of which is unlikely), but also (and more systematically) on the drift ratio demands on the building stories. Drift ratio at punching shear failure is also shown to be highly dependent on the gravity induced shear stress level in the slab around the connection. Kang and Wallace (2006) provide a summary of test data with different gravity shear ratios on different connection types. In their study, best-fit line minus one standard deviation for test data follows almost the same line in ACI 318M-14, which represents Equation 2.13 (Figure 2.9).

$$\Delta_i / h_i = 0.035 - 0.05\left(\frac{v_{ug}}{\phi v_c}\right) \tag{2.13}$$

Moreover, plastic rotation capacities, are presented in ASCE 41-17 as modeling parameters for slabs and slabs-column connections, which are derived from test data with the assumption of column rotations are negligible and elastic rotations are around 0.01 radians for RC slabs (Elwood *et al.*, 2007). The modeling parameters and acceptance criteria are listed in Table 2.2.

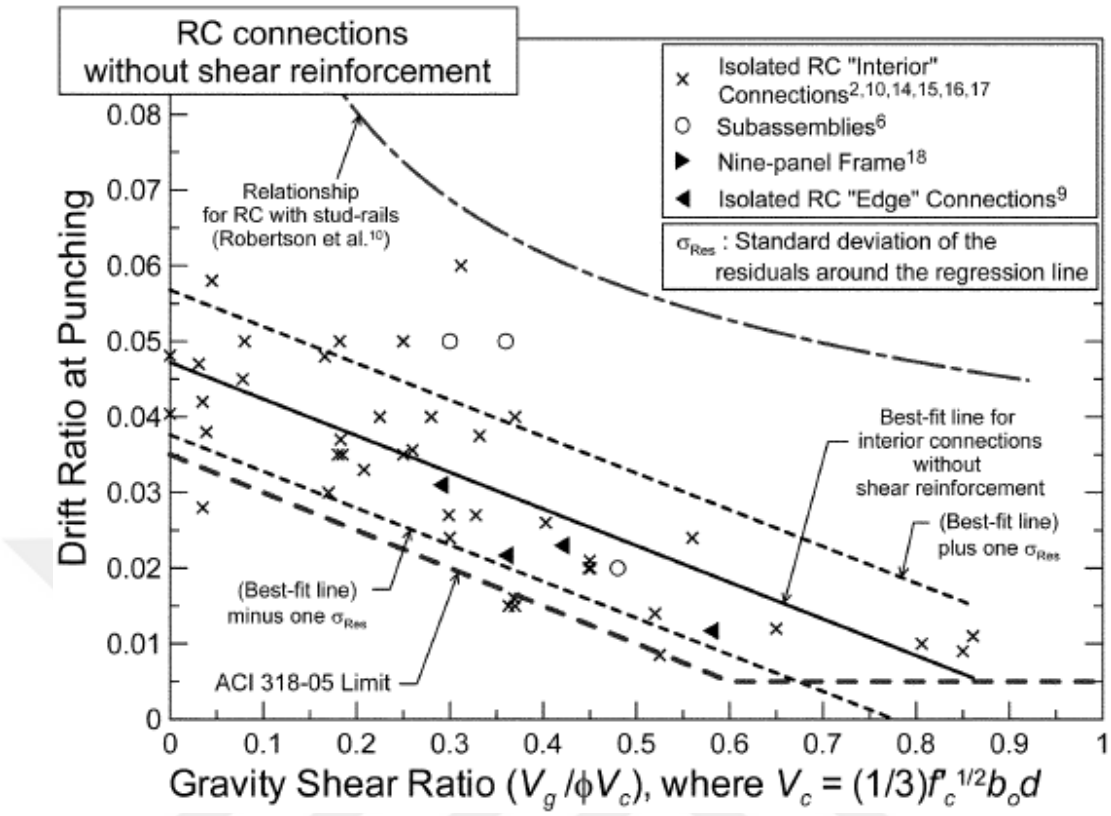

Figure 2.9. Gravity shear ratios versus drift ratio at punching (Kang and Wallace, 2006).

Table 2.2. Modeling parameters and acceptance criteria for slab-column connections.

Conditions		Plastic Rotations (rad)		Strength Loss Ratio	Performance Acceptance Criteria (rad)		
V_g/V_c	Continuity Reinforcement	a	b	c	IO	LS	CP
0	Yes	0.035	0.05	0.2	0.01	0.035	0.05
0.2	Yes	0.03	0.04	0.2	0.01	0.03	0.04
0.4	Yes	0.02	0.03	0.2	0	0.02	0.03
≥0.6	Yes	0	0.02	0	0	0	0.02
0	No	0.025	0.025	0	0.01	0.02	0.025
0.2	No	0.02	0.02	0	0.01	0.015	0.02
0.4	No	0.01	0.01	0	0	0.008	0.01
0.6	No	0	0	0	0	0	0
>0.6	No	0	0	0	-	-	-

2.7. Post Punching Behavior

Punching failure can cause sudden loss of load carrying capacity at a connection. After failure of a connection, vertical load resisted by the connection is redistributed among nearest connections. In some cases, adjacent connections may fail under increased vertical loads, which may lead to progressive collapse of structure. To avoid progressive collapse of a flat plate system even when the connections lose their load carrying capacity, continuous bottom reinforcement passing through punching cone needs to be placed. Hwang and Moehle (2000a) show that bottom reinforcement passing through punching cone as integrity (continuity) reinforcement is more effective than top bars, due to the possibility of concrete cover spalling (Figure 2.10).

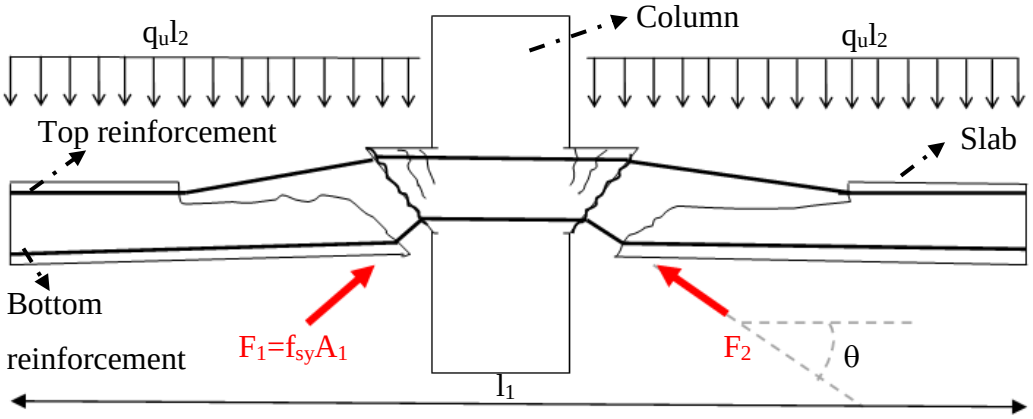

Figure 2.10. Post-punching equilibrium.

Continuity reinforcement must satisfy force equilibrium in the vertical direction after punching failure. Resisting forces must be equal to the applied service loads. The resultant vertical service load ($q_u l_1 l_2$) corresponds to uniformly distributed load on the tributary area of a column, and the resisting force ($\phi 4 f_{sy} \sin\theta A_s$) equals to the resultant vertical force provided by the reinforcement along the four punching perimeter faces of an interior connection, for example. The required amount of continuity reinforcement is calculated using Equation 2.14 (Moehle, 2015), where the angle θ can be taken as 30° degrees.

$$A_{s,\min} = \frac{q_u l_1 l_2}{\phi 4 f_{sy} \sin\theta} \tag{2.14}$$

3. MODELING APPROACH FOR SLAB-COLUMN CONNECTIONS

3.1. Description

In the light of previously discussed concepts on flat plate floor systems, generating an analytical model for capturing the nonlinear behavior of the slabs and slab-column connections appears to be possible. However, in current practice, it is almost impossible due to incapabilities of commercial analysis programs as well as complex configurations of real-life building structures. Therefore, the first approach to assess the seismic performance of such structural systems is to do the performance checks manually, based on story drift ratios obtained from nonlinear analysis. Performance evaluation of the slab-column connections can be conducted by manually reviewing analysis results including story drift ratios and unbalanced moments in the columns. Potential failure modes can thus be detected; however, it must be noted that analysis results will not be valid after first failure has occurred. This method is obviously not for projects with time constraints. Kang *et al.* (2009) proposes a second approach that involves nonlinear modeling of the slab-column connections using torsional hinges. In that study, it is clearly stated that commercial nonlinear analysis software is not adequate for such modeling. Therefore, they implemented their proposed modeling methodology in the OpenSees platform, to analyze a simple slab-column frame assembly and compare model results with test data. They have stated that simpler and more efficient modeling methodologies are necessary to analyze complex real-life structures.

In this thesis, the modeling approach by Kang *et al.* (2009) is simplified and implemented in commercial analysis software (CSI Perform 3D), using a novel equivalent shear hinge modeling approach to replace the original torsional hinge model, so that the nonlinear behavior and performance of real-life flat plate building structures can be assessed both reliably and efficiently.

CSI Perform 3D analysis software can be used for both nonlinear response history analysis and nonlinear static (pushover) analysis. However, there is not a torsional hinge element to transfer unbalanced moments from columns to the slab in the software.

Therefore, in this study, an equivalent shear hinge model is proposed to effectively replicate a torsional hinge in CSI Perform 3D. Nonlinear static analysis is conducted to validate equivalent shear hinge modeling approach and to compare model results with not only results of more detailed analytical models in the literature (Kang *et al.* 2009), but also data from shake table experiments.

3.2. Analytical Frame Model

3.2.1. Equivalent Shear Hinge Model

An equivalent shear hinge modeling approach is proposed in this study to simulate the nonlinear behavior of slab-column connections, due to absence of a torsional hinge in commercial analysis programs. Two different behavior (or failure) modes, including punching shear failure along the punching perimeter (brittle) and reaching the bending moment capacity (ductile) within the slab moment transfer width ($c+5h$) due to unbalanced column moments at the connection can be represented using the equivalent shear hinge model proposed. Unbalanced moment and joint rotations are converted to couple forces and transverse (shear) displacements respectively, in the equivalent shear hinge model formulation (Figure 3.1). The unbalanced moment is basically the shear hinge force multiplied by the moment arm (Equation 3.1) and shear displacement is joint (torsional) rotation divided by half the moment arm as per the small angle theorem (Equation 3.2).

$$M_{unb} = Fl \tag{3.1}$$

$$\Delta = \frac{\theta l}{2} \tag{3.2}$$

Force and moment equilibriums are satisfied in the equivalent shear hinge model. Torsional releases are placed at the ends of rigid beams to preserve stability of model and to stop forming undesirable torsion at the model. Plastic rotation capacities and performance criteria are taken from ASCE 41 table (Table 2.2).

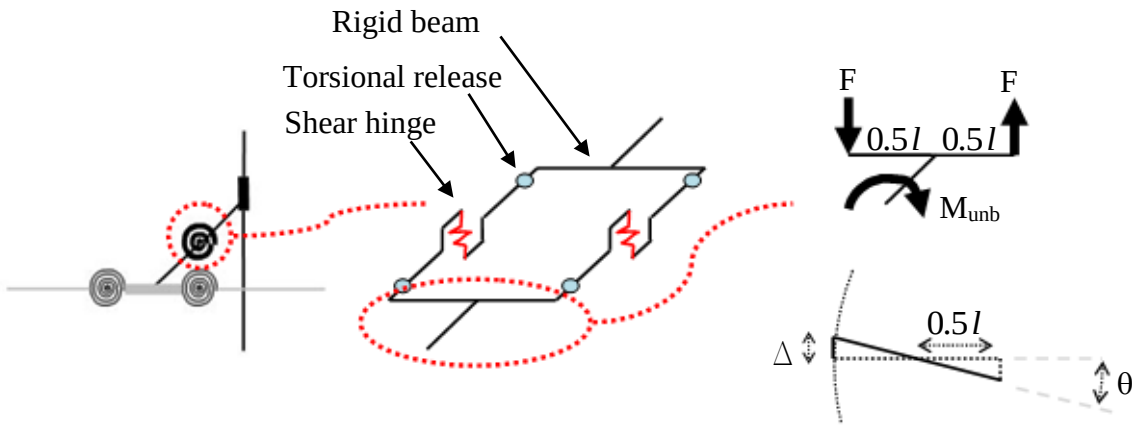

Figure 3.1. Equivalent shear hinge model.

Dissipated energy must also be equal in two modeling approaches (Kang and proposed model). Area under Kang's model must be equal to sum of areas under equivalent shear hinges (Equation 3.3). To compare areas, simplified force-deformation relationship of Kang's model is shown in Figure 3.2, whereas strain hardening is also included in analytical plane frame model of Kang.

$$A_1 = 2A_2 \tag{3.3}$$

Left side of Equation 3.3 may be rewritten as (Figure 3.2):

$$Ma = 2A_2 \tag{3.4}$$

Right side of Equation 3.3 may be reorganized as Equation 3.5 (Figure 3.3).

$$Ma = 2\left(V\Delta_a\right) \tag{3.5}$$

Equation 3.6 is obtained when shear hinge force and shear force are transformed using Equations 3.1 and 3.2.

$$Ma = 2\left(\frac{M}{l}\frac{al}{2}\right) \tag{3.6}$$

Previous equation can be simplified as Equations 3.7.

$$Ma = Ma \tag{3.7}$$

Two areas (dissipated energy) from two different models are equal as required. Therefore proposed equivalent shear hinge model dissipates equal energy with model of Kang.

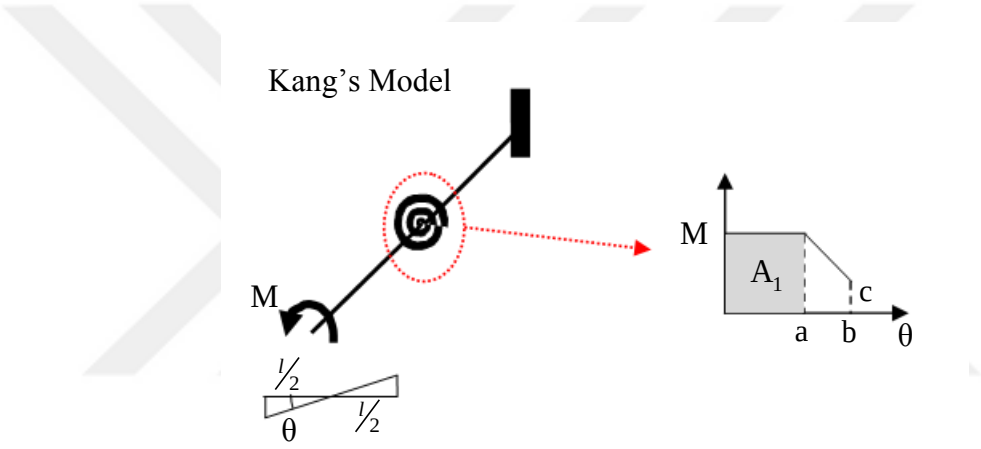

Figure 3.2. Kang's torsional hinge model and its force-deformation relationship.

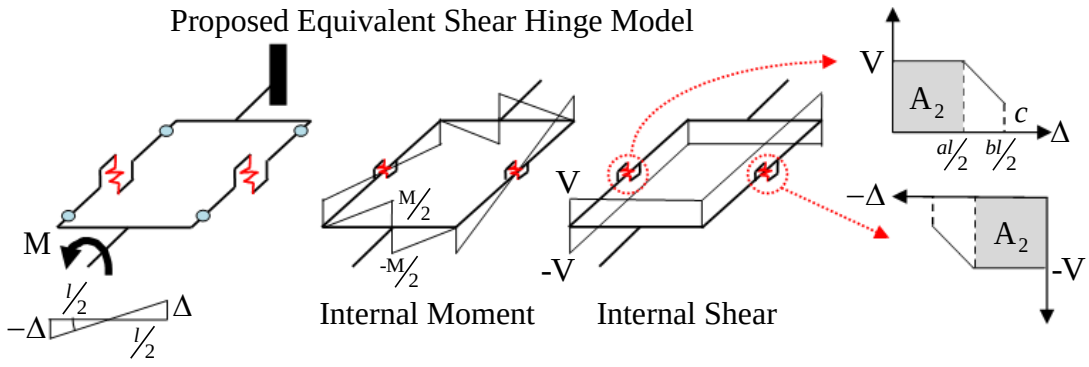

Figure 3.3. Proposed equivalent shear hinge model and its force-deformation relationship.

3.2.2. Frame Model Properties

An analytical plane frame model of the approximately one-third scale copy of RC flat plate slab column assembly specimen subjected to shake table tests is first developed. A summary of the specimen properties is explained in following. Detailed information on the specimen and the test can be found in the study of Kang *et al.* (2009) (Figure 3.4).

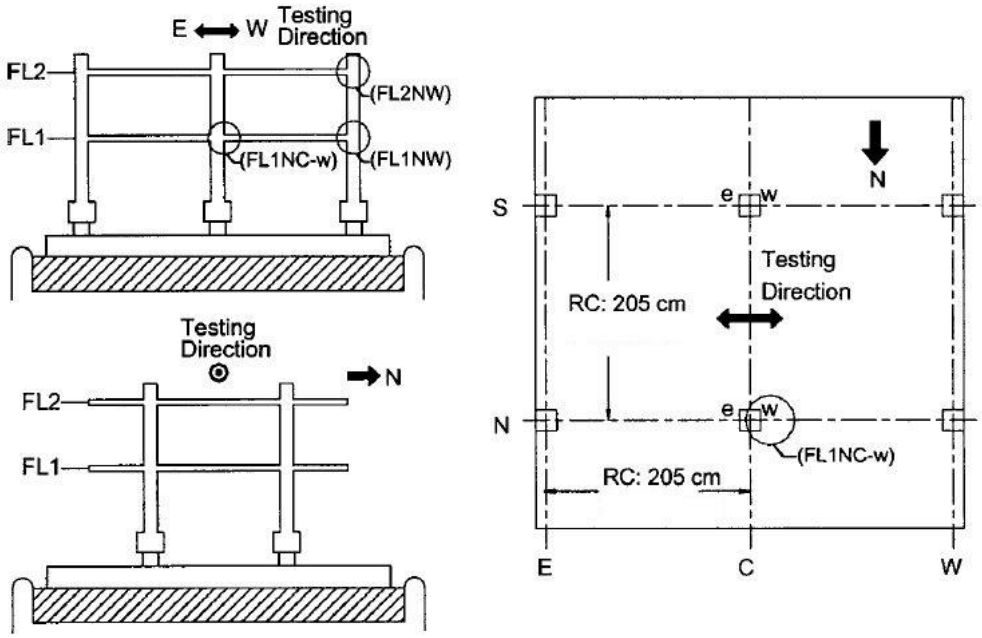

Figure 3.4. Shake table test specimen (Kang *et al*., 2009).

The two-story two-bay by two-bay flat plate RC frame specimen has 2.06m span length and 89mm slab thickness. The specimen has square columns with 203x203 mm cross-sections. Concrete compressive strength is 27.6 MPa. Grade60 #3 (ϕ9.5) slab reinforcement and #4 (ϕ12.7) column reinforcement is used in construction.

In modeling of the specimen plastic hinges are assigned at the end of columns and column strips. Dimensions and capacities of effective slab width (for stiffness), slab moment transfer width ($c+5h$), and column strips are listed in Table 3.1. α and β are taken as 0.75 and 0.33 in modeling for equivalent stiffness.

Table 3.1. Dimensions and capacities of slab elements.

Name of Members	Dimensions (mm)	Positive Moment Capacity (kN.m)	Negative Moment Capacity (kN.m)
Full Span	2057	-	-
Eff. Slab Width	1543 (αl) 509 ($\alpha\beta l$) α =0.75, β =0.33	-	-
CS	1029	23.5	28.9
$c+5h$	648	16.9	21.3

Gravity shear stress ratios in the slabs are calculated as 0.25 for the interior and 0.2 for the exterior connections. Plastic rotation capacities of the torsional hinges at the connections and moment hinges in the column strips (CS) are defined according to ASCE 41-17 recommendations where it is assumed that continuity reinforcement is available (Table 3.2).

Table 3.2. Modeling parameters for the slab-column frame.

Conditions		Plastic Rotations (rad)		Strength Loss Ratio	Performance Acceptance Criteria (rad)		
V_g/V_c	Continuity Reinforcement	a	b	c	IO	LS	CP
0.20	Yes	0.03	0.04	0.2	0.01	0.03	0.04
0.25	Yes	0.0275	0.0375	0.2	0.0075	0.0275	0.0375

γ_f is taken 1 in the calculations for the exterior connections, which means total unbalanced moment is resisted by the slab within the moment transfer width. Therefore, there is no possibility of nonlinear behavior of the CS hinges, since the flexural capacity of the moment transfer region ($c+5h$) is smaller. Hence, exterior connections of the specimen are modeled as weak connections. Capacity of the interior connections is calculated from the minimum of the results of Equation 2.10 and Equation 2.11. In the calculation of the interior connection unbalanced moment capacity, γ_f is taken as 0.75 (γ_f

is same in Kang's model). Interior connections are also weak connections because their unbalanced moment capacity is lower than the total capacity of two adjacent column strip (CS) hinges (Table 3.3). one of the equivalent shear hinge or column strip (CS) hinge is assigned to slab-column connections to make model simplified as suggested ASCE 41.

Table 3.3. Types and capacities of connections.

Connection Location	Capacity	Adjacent CS Capacity	Connection Type
Interior, $\gamma_f = 0.75$	Min. of (50.9;68.7)	23.5+28.9	Weak
Exterior, $\gamma_f = 1$	+16.9 -21.3	+23.5 -28.9	Weak

The analytical frame model is generated with the parameters explained in the prior paragraphs, using the proposed equivalent shear hinge approach in CSI Performed 3D software (Figure 3.5). Description of the modeling approach is presented only briefly in this chapter, since it will be described in more detail in the following chapter for a real-life tall building structure.

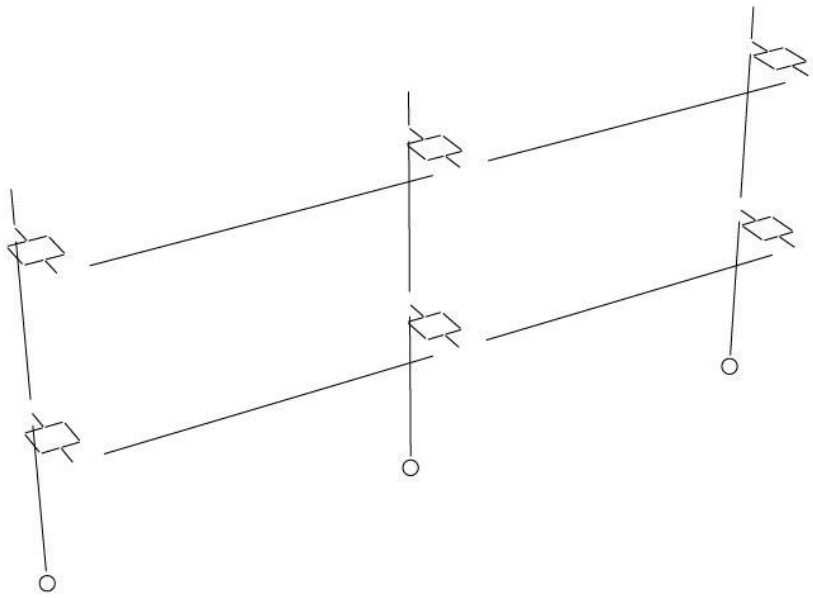

Figure 3.5. Analytical frame model of the shake table test specimen in CSI Perform 3D.

3.3. Experimental Validation of the Frame Model Using Pushover Analysis

Pushover analysis is a nonlinear static analysis method for evaluating the force-displacement behavior of a structural system. After application of gravity loads, the structure is subjected to displacement-controlled and proportionally-applied lateral loads that gradually increase until a target displacement level is reached. Lateral load distribution may be proportional to mass distribution or mode shape. Pushover analysis is used to validate the analytical modeling approach proposed (equivalent shear hinge model in CSI Perform 3D), against experimental data obtained from the shake table tests of the slab-column frame specimen, as well as the more detailed analysis conducted previously by Kang *et al.* (2009) using OpenSees.

Pushover analysis results obtained using the modeling approach adopted in this study for the two-story two-bay frame specimen is compared with pushover analysis results and shake table test results reported for the specimen by Kang *et al.* (2009) (Figure 3.4). Base shear versus top drift ratio responses are obtained from the pushover analyses, under lateral load ratios of 1:2 and 2:1, in both sets of analysis results. The shake table test data shown in the figure was already processed by Kang *et al.* (2009) to be suitable for comparison with nonlinear static analysis results. According to Kang *et al.* (2009), force configuration 1:2 gives better results within linear range, while force configuration 2:1 gives better results within the nonlinear range. It can be observed from Figure 3.6 that analysis results obtained using the proposed modeling approach with equivalent shear hinges at the slab-column connections are consistent with both the analytical results and experimental data presented by Kang *et al.* (2009) for the test specimen, in terms of lateral stiffness, lateral load capacity, and ductility (drift capacity) of the slab-column frame assembly.

Yielding and failure mechanism propagation is very similar Kang and proposed plane frame models under pushover analysis with 2:1 force configuration (Figure 3.7). Yielding of columns at the base can be seen at different instants due to different modeling approaches. In this study columns are modeled using PMM hinges, whereas distributed plasticity (fiber model) approach is used in the study of Kang *et al.* (2009). Slab yielding in column strip, slab yielding in moment transfer width and punching failure can be observed in Kang's frame model because of using both torsional hinge and column strip (CS) hinge

in OpenSees platform. Including strain hardening is another reason to increasing variety of failure mechanisms in Kang's model. However, in order to create simpler and applicable method to commercial programs, either equivalent shear hinge model or column strip (CS) hinge is assigned to the slab-column connections. And the whole connections are also weak. Therefore, reaching to the ultimate tensile strain in slab moment transfer width after observing slab yielding in moment transfer width is the only failure mechanism in model that is generated using equivalent shear hinges.

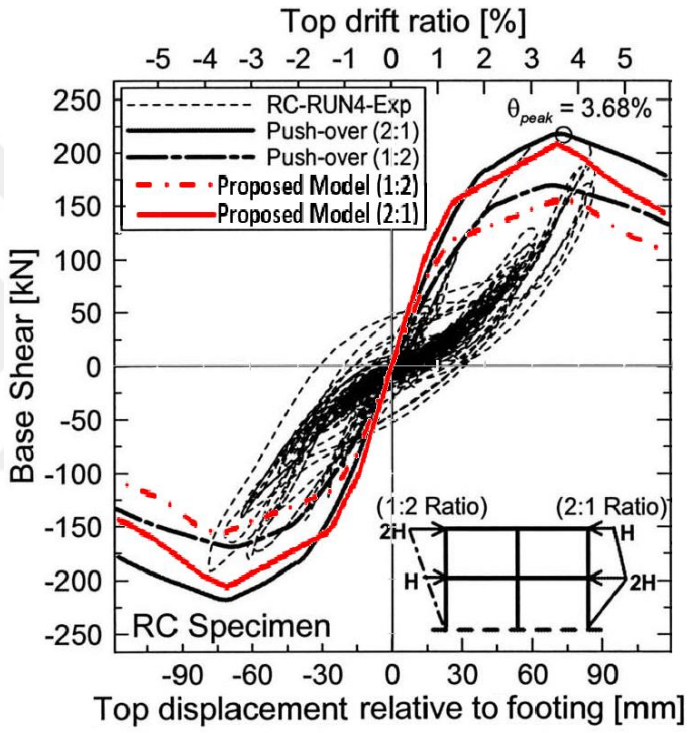

Figure 3.6. Comparison of analytical pushover curves and experimental data for the slab-column frame specimen.

Yielding propagation of first five joints is almost the same with respect to their locations and top drift ratios in two models (Figure 3.7). Then, column strips' yielding is seen in Kang's model. There is not any column strip hinge in the other model so there is not any yielding of column strip point in Figure 3.7. Afterwards, failures are observed for models. Failure mechanisms are different due to different modeling approaches. In this study, rigid perfectly plastic hinges are assigned to the slab-column connections. Therefore, reaching ultimate tensile strain in moment transfer with is the failure mechanism. On the other hand, rigid with strain hardening hinges are assigned to joints so

failure can be due to reaching punching shear capacity or ultimate tensile strain in moment transfer width in Kang's model.

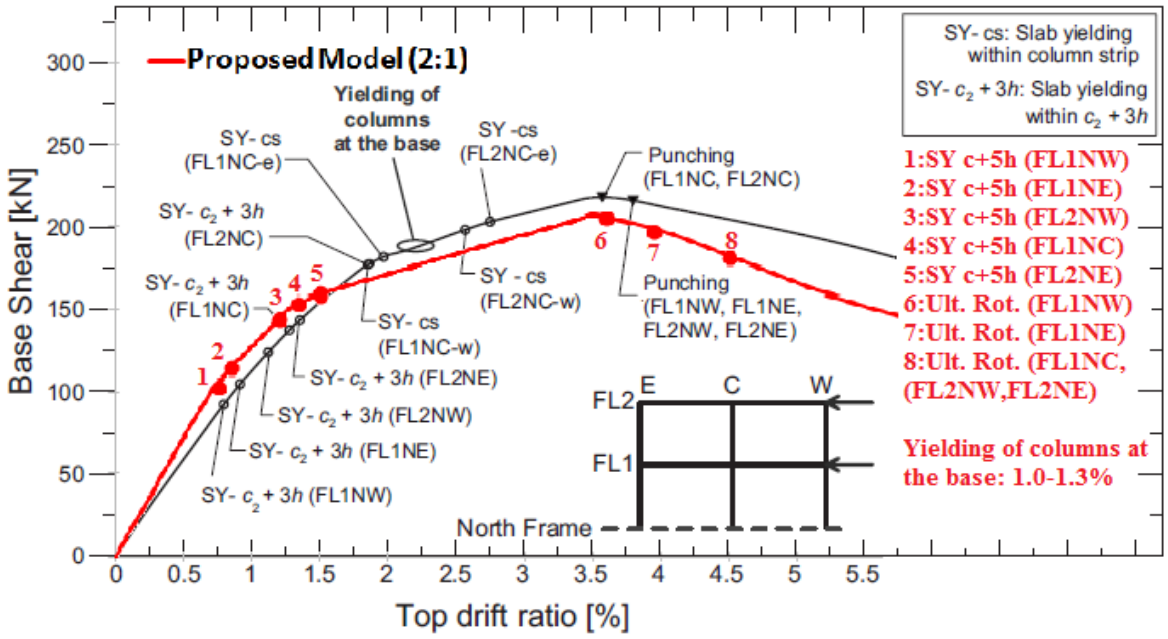

Figure 3.7. Comparison of failure mechanisms propagation.

4. DESIGN, MODELING, AND ANALYSIS OF A PROTOTYPE TALL BUILDING

4.1. Structural Properties

The hypothetical reinforced concrete flat plate tall building investigated in this study consists of 21 (one as roof) stories above and 2 stories below the ground surface. Total height of building is 80.5 m from the foundation to the roof, and each story has 3.5 m height (Figure 4.1 and Figure 4.2). Two C-shaped core walls connected with coupling beams and six rectangular walls placed around perimeter of structure are used as the lateral load resisting system. Columns are used mainly to resist gravity loads. Typical plans for normal floors and basement floors can be seen in Figure 4.3 and Figure 4.4. Plan area of normal floors and basement floors are 1681 m^2 and 3249 m^2, respectively. The intended purpose of the normal floors and the basement floor are assumed to be residential areas and parking lots, respectively.

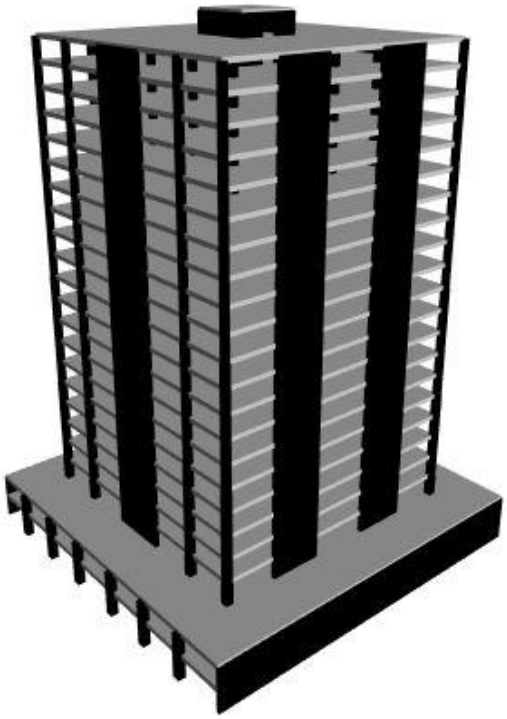

Figure 4.1. 3D view of the structure.

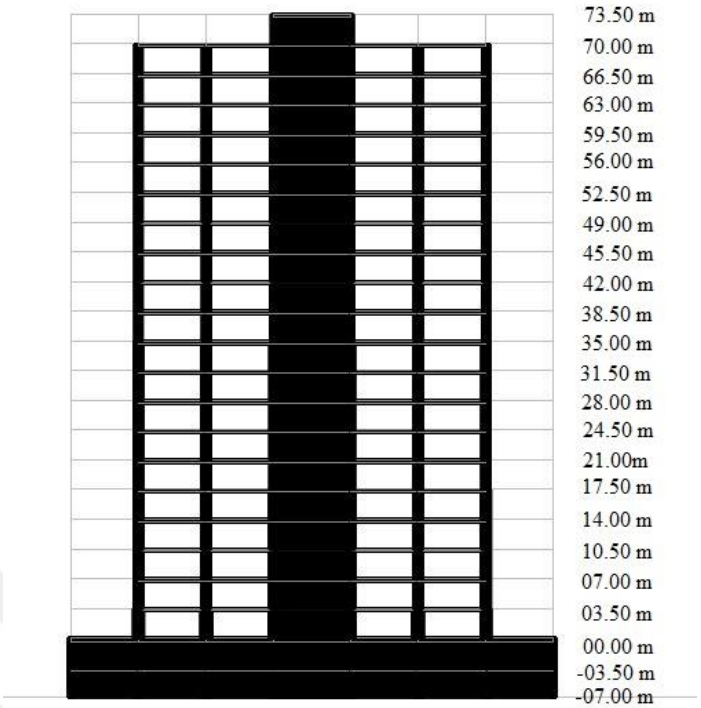

Figure 4.2. Elevation view of the structure.

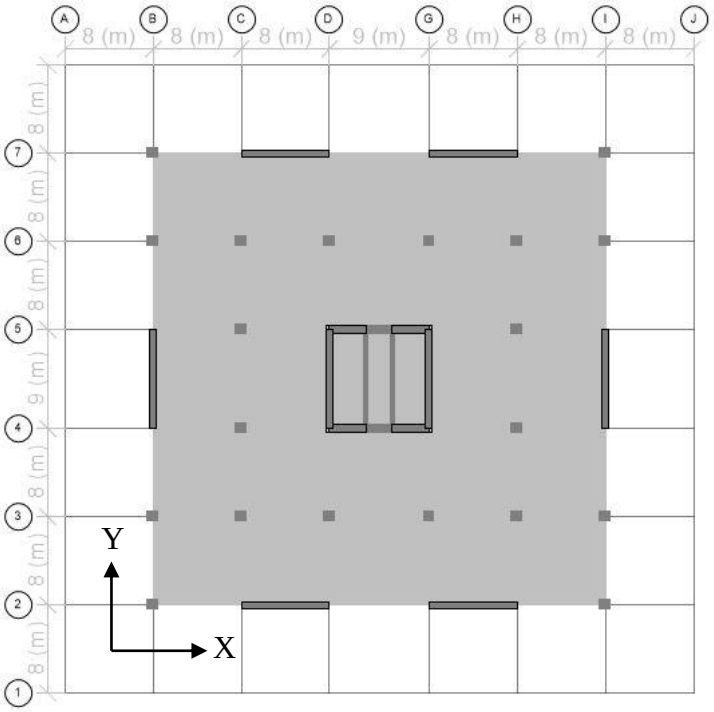

Figure 4.3. Normal floor plan view.

Based on linear elastic design procedure, thicknesses of core walls and perimeter walls are 700 mm at the ground level, and their thickness reduces gradually along building height to 50 mm. Coupling beam cross sections are 70 cm x 120 cm at all story levels. Columns cross section start with 120 cm x 120 cm at ground level, and decrease to 90 cm x 90 cm at the top floor. Finally, overall depth of the flat plate slabs is 30 cm throughout the building. Exceptions and details are listed in Table 4.1.

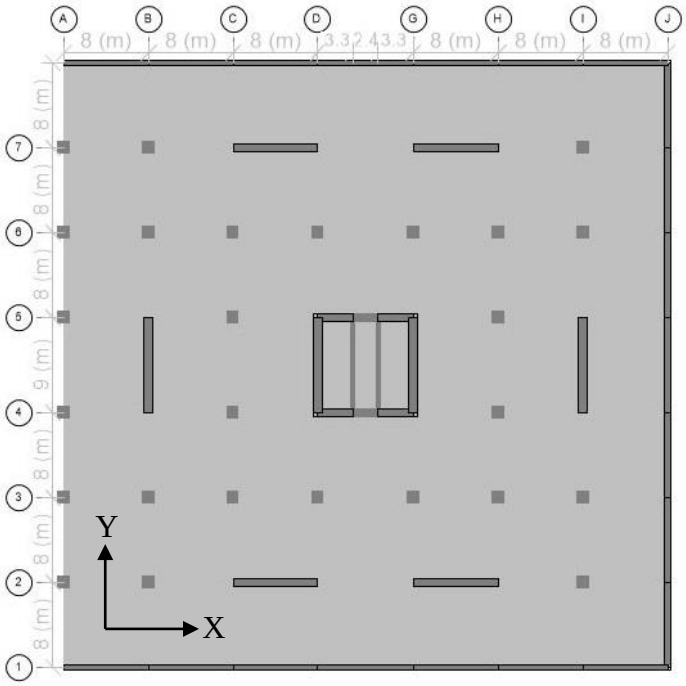

Figure 4.4. Basement floor plan view.

Clear cover is taken 35 mm in the columns and walls, 25 mm in the beams, and 20 mm in the slabs in order to provide resistance to fire and atmospheric effects.

4.2. Linear Elastic Modeling

A linear elastic model of the structure is first created using CSI ETABS software. Element modeling approaches and effective section rigidities of the structural elements comply with TEC 2018. Line elements are used for modeling of the columns and beams, whereas shell elements are used for the slabs and the walls. Seismic masses are defined according to TEC 2018, considering live load participation factors. Requirements for

Design and Construction of Reinforced Concrete Structures (TS 500) (Turkish Standards Institute, 2000) is used to define the concrete modulus of elasticity. Uniformly distributed live loads values are assigned based on Design Loads for Buildings (TS 498) (Turkish Standards Institute, 1997).

Table 4.1. Dimensions of members.

Type of member	2B-1B	1N	2N-5N	6N-10N	11N-20N(21N)
	-7 to 0	0 to 3.5	3.5 to17.5	17.5 to 35	35 to 70 (73.5)
	Member Thickness (Cross Sections)(cm) at Floors and Elevations (m)				
Columns	120	120	110	100	90
Coupling Beams	80x120	70x120	70x120	70x120	70x120
Slabs	40	30	30	30	30
Perimeter Walls	80	70	70	60	50
Core Walls in X dir.	80	70	70	70	70
Core Walls in Y dir.	80	70	70	60	50
Basement Walls	50	-	-	-	-

4.2.1. Material Properties

Elastic modulus of concrete is necessary for linear elastic analysis. Reinforcement yield strength required in later design stages. In the model of the prototype building, C50 class concrete is assumed, which has a characteristic compressive strength $f_{ck} = 50$ MPa. Modulus of Elasticity of C50 class concrete is calculated as $E_c = 37000$ MPa from Equation 4.1 (TS 500). Shear Modulus of C50 class concrete is calculated as $G_c =$ 15417 MPa from Equation 4.2 (TS 500) by taking Poisson Ratio as $\nu_c = 0.2$ (TS 500). Unit weight of concrete is taken as $\gamma_c = 25$ kN/m^3 in dead load calculations.

$$E_c = 3250\sqrt{f_{ck}} + 14000 \tag{4.1}$$

$$G_c = \frac{E_c}{2(1+\nu_c)} \tag{4.2}$$

4.2.2. Gravity Loads

The structural model is subjected to dead loads and live loads the seismic mass of the structure is defined to be compatible with the assigned loads by the computer program. Correct determination of the magnitude and distribution of the loads and masses is crucial to reliable analysis results. In this study, self-weights of members are calculated by the CSI ETABS analysis software and remaining dead loads are assigned to slabs as uniformly distributed loads. Live loads magnitudes are taken from TS 498. Live load participation factors are considered in seismic mass calculations. Magnitude of all loads are listed in Table 4.2.

Table 4.2. Magnitude of uniform loads.

Type of Load	Uniform Load (kN/m^2)
Floor finishes, bedding and ceiling plaster	2.20
Partition Walls	1.50
Live Load Residential	2.00
Live Load Corridor	3.50
Live Load Basement	5.00
Live Load Roof	1.50
Snow Load	0.75

4.2.3. Seismic Loads

In linear elastic design process, the so-called DD2 earthquake hazard level is used to define the design spectrum according to TEC 2018. DD2 level is defined in TEC 2018 as the standard design earthquake ground motion with a probability of exceedance of 10% in 50 years and reoccurrence period of 475 years. Short period and long period spectral acceleration coefficients are needed to construct the design spectrum. These spectral acceleration coefficients are obtained from Turkish Earthquake Hazard Map website (Disaster and Emergency Management Presidency, 2018) for the hypothetical construction site at coordinates 41°00’00.0”N, 28°42’00.0”E. Spectral acceleration coefficients for this site are for a reference soil condition that falls between ZB and ZC soil classes with first 30m depth shear wave velocity ($V_{s,30}$) of 760 m/s, under the DD2 earthquake level, and for

5% damping. The spectral acceleration coefficients assumed for the prototype building are listed in Table 4.3.

Table 4.3. Spectral acceleration coefficients for the prototype building under DD2 earthquake level

	S_S	S_1
DD2	1.176	0.319

Spectral accelerations coefficients are then used to calculate design spectral acceleration coefficients, using Equation 4.3 and 4.4, considering local soil conditions at the hypothetical construction site. Assuming that the local soil class is ZC, local soil effect coefficients according to TEC 2018 are obtained as $F_s = 1.2$ for short period and $F_1 = 1.5$ for one second period, from Table 4.4 and 4.5.

$$S_{DS} = S_S F_S \tag{4.3}$$

$$S_{D1} = S_1 F_1 \tag{4.4}$$

Table 4.4. Local soil effect coefficient for short period.

Local Soil Class	Local Soil Effect Coefficient for short period, F_s					
	$S_s \leq 0.25$	$S_s = 0.50$	$S_s = 0.75$	$S_s = 1.00$	$S_s = 1.25$	$S_s \geq 1.50$
ZA	0.8	0.8	0.8	0.8	0.8	0.8
ZB	0.9	0.9	0.9	0.9	0.9	0.9
ZC	1.3	1.3	1.2	1.2	1.2	1.2
ZD	1.6	1.4	1.2	1.1	1.0	1.0
ZE	2.4	1.7	1.3	1.1	0.9	0.8
ZF	Site specific soil behavior must be done.					

Table 4.5. Local soil effect coefficient for one second period.

Local Soil Class	Local Soil Effect Coefficient for one second period, F_1					
	$S_s \leq 0.10$	$S_s = 0.20$	$S_s = 0.30$	$S_s = 0.40$	$S_s = 0.50$	$S_s \geq 0.60$
ZA	0.8	0.8	0.8	0.8	0.8	0.8
ZB	0.8	0.8	0.8	0.8	0.8	0.8
ZC	1.5	1.5	1.5	1.5	1.5	1.4
ZD	2.4	2.2	2.0	1.9	1.8	1.7
ZE	4.2	3.3	2.8	2.4	2.2	2.0
ZF	Site specific soil behavior must be done.					

Design spectral acceleration coefficients are presented in Table 4.6. Finally, elastic design spectrum and the reduced design spectra with which is based on the structural system behavior factors in each direction are generated for the DD2 earthquake level as shown in Figure 4.5, using Equations 4.5, 4.6, 4.7 and 4.8.

Table 4.6. Design spectral acceleration coefficients.

	S_{DS}	S_{D1}
DD2	1.411	0.479

$$S_{ae}(T) = \left(0.4 + 0.6\frac{T}{T_A}\right) S_{DS} \qquad (0 \leq T \leq T_A) \tag{4.5}$$

$$S_{ae}(T) = S_{DS} \qquad (T_A \leq T \leq T_B) \tag{4.6}$$

$$S_{ae}(T) = \frac{S_{D1}}{T} \qquad (T_B \leq T \leq T_L) \tag{4.7}$$

$$S_{ae}(T) = \frac{S_{D1} T_L}{T^2} \qquad (T_L \leq T) \tag{4.8}$$

where corner periods T_A, T_B and limit period for constant displacement range T_L are given by Equation 4.9.

$$T_A = 0.2\frac{S_{D1}}{S_{DS}} \qquad T_B = \frac{S_{D1}}{S_{DS}} \qquad T_L = 6\ s \tag{4.9}$$

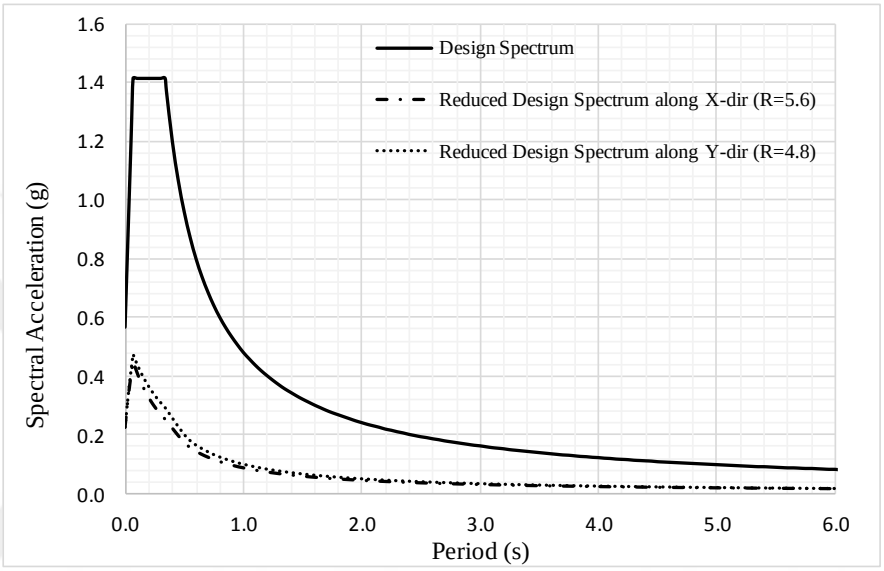

Figure 4.5. Design spectra for DD2 level earthquake ground motion.

According to TEC 2018, vertical acceleration response spectrum must also be constructed in some cases. However, vertical earthquake effect is included only as equivalent static vertical load, calculated using Equation 4.9, if the structure does not have columns supported by beams, inclined columns, beams with spans larger than 20 m, or cantilever beams longer than 5 m.

$$E_d^{(Z)} \approx (2/3)S_{DS}G \tag{4.9}$$

4.2.4. Load Combinations

Load combinations are derived to generate the most critical scenario, which the structure or a structural member may subjected to, under different loading conditions. Therefore, several load combinations are entered into CSI ETABS software to obtain

envelopes for accurate design. Combinations are shown in Table 4.7 with respect to TS 500 and TEC 2018.

Table 4.7. Load combinations.

Design Combinations
$1.4G+1.6Q$
$0.9G+1.6H$
$G+Q+0.2S+E_d^{(H)}+0.3E_d^{(Z)}$
$0.9G+H+E_d^{(H)}-0.3E_d^{(Z)}$

4.2.5. Seismic Masses

Seismic masses are important to simulate the dynamic response of a structure. Dead loads are permanent loads so that they directly contribute to seismic mass. However, the structure may not be fully loaded with design live loads when an earthquake occurs. For this reason, live loads are reduced by live load participation factors before they are added to seismic masses. Live load reduction factors are listed in Table 4.8 with respect to TEC 2018.

Table 4.8. Live load contribution factor.

Load Type	Live Load Contribution Factor (n)
Live Load Residential	0.3
Live Load Parking Lot	0.3
Snow Load	0.3

In CSI ETABS software, masses of structural that are modeled using shell elements are assigned to joints as concentrated masses, according to the distributed masses in the tributary areas of the joints. Mass of a finite element joint is calculated using Equation 4.10 and 4.11, as a combination of dead and live loads.

$$w_j^{(S)} = w_{G,j}^{(S)} + n w_{Q,j}^{(S)} \tag{4.10}$$

$$m_j^{(S)} = \frac{w_j^{(S)}}{g} \tag{4.11}$$

4.2.6. Structural Members

Structural members can be represented using different modeling approaches in finite element modeling. In common practice, beams and columns are modeled as frame (line) finite elements that consist of two nodes with six degree of freedom connected to each other with a line element. Walls and slabs are usually modeled with four node area objects that show both plate and membrane behavior.

Table 4.9. Stiffness modifier of reinforced concrete elements.

RC Structural Element	Effective Rigidity	
Wall-Slab (In Plane)	Axial	Shear
Structural Wall	0.50	0.50
Basement Wall	0.80	0.50
Slab	0.25	0.25
Wall-Slab (Out of Plane)	Bending	Shear
Structural Wall	0.25	1.00
Basement Wall	0.50	1.00
Slab	0.25	1.00
Line Element	Bending	Shear
Coupling Beam	0.15	1.00
Moment Frame Beam	0.35	1.00
Moment Frame Column	0.70	1.00
Wall (Modeled as Equivalent Line Element)	0.50	0.50

Additionally, taking gross section rigidities is not realistic and provides an overestimation of structural rigidity for reinforced concrete structures under earthquake actions. For this reason, stiffness modifiers must be applied to sections to represent

cracking of concrete under tension due to reversed cyclic loads. The stiffness modifiers are tabulated in Table 4.9.

4.2.7. Damping

Viscous damping is an equivalent damping parameter defined for a structure that represents energy dissipation of the structure, the materials, the joints, and the nonstructural components, due to internal friction effects developing in the structure during even the linear elastic response stage. Differently from nonlinear response history analysis, there is no hysteretic behavior of the members in linear elastic analysis. Therefore, viscous damping does not represent dissipated energy due to nonlinear behavior. 5% constant modal damping is defined in the linear response spectrum analysis, with respect to TEC 2018.

4.2.8. Model

The linear elastic model of the building shown in Figure 4.6 was generated in compliance with the aforementioned modeling parameters. Fixed supports are assigned at the base of the building, instead of including foundation and soil springs in the model. Semi-rigid diaphragms are assigned to each floor level to regard accidental eccentricity of 5%. CSI ETABS software considers effect of accidental eccentricity automatically. At the slab-column connections, rigid end zones are assigned to omit double counting of masses.

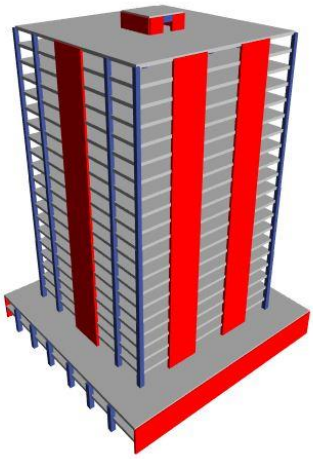

Figure 4.6. 3D ETABS model.

Natural vibration periods and model shapes are calculated using Ritz-Vector analysis in CSI ETABS. According to Ritz-Vector analysis, first three mode shapes of two directions and torsion are $T_{X,1} = 3.081$ s, $T_{Y,1} = 3.065$ s, $T_{B,1} = 2.385$ s, $T_{X,2} = 0.757$ s, $T_{Y,2} = 0.639$ s, $T_{B,2} = 0.577$ s, $T_{X,3} = 0.332$ s, $T_{Y,3} = 0.272$ s, $T_{B,3} = 0.244$ s and are shown in Figure 4.7. 95% mass participation ratios in both directions is reached at the 20th mode. Natural periods and mass participation ratios for the modes are listed in Table 4.9.

Table 4.10. Fundamental periods and mass participation ratios.

Mode No.	Period (s)	Mass Participation Ratio on X dir.	Mass Participation Ratio on Y dir.	$\sum X$	$\sum Y$
1	3.081	0.697	0.000	0.697	0.000
2	3.065	0.000	0.681	0.697	0.681
3	2.385	0.000	0.000	0.697	0.681
4	0.757	0.176	0.000	0.874	0.681
5	0.639	0.000	0.201	0.874	0.882
6	0.577	0.000	0.001	0.874	0.883
7	0.332	0.063	0.000	0.937	0.883
8	0.272	0.000	0.064	0.937	0.947
9	0.244	0.000	0.000	0.937	0.947
10	0.199	0.029	0.000	0.966	0.947
11	0.167	0.000	0.026	0.966	0.973
12	0.142	0.013	0.000	0.979	0.973
13	0.142	0.001	0.000	0.980	0.973
14	0.123	0.000	0.011	0.980	0.984
15	0.113	0.007	0.000	0.986	0.984
16	0.101	0.000	0.005	0.986	0.989
17	0.100	0.000	0.001	0.986	0.990
18	0.096	0.003	0.000	0.990	0.990
19	0.088	0.000	0.003	0.990	0.992
20	0.084	0.002	0.000	0.992	0.992

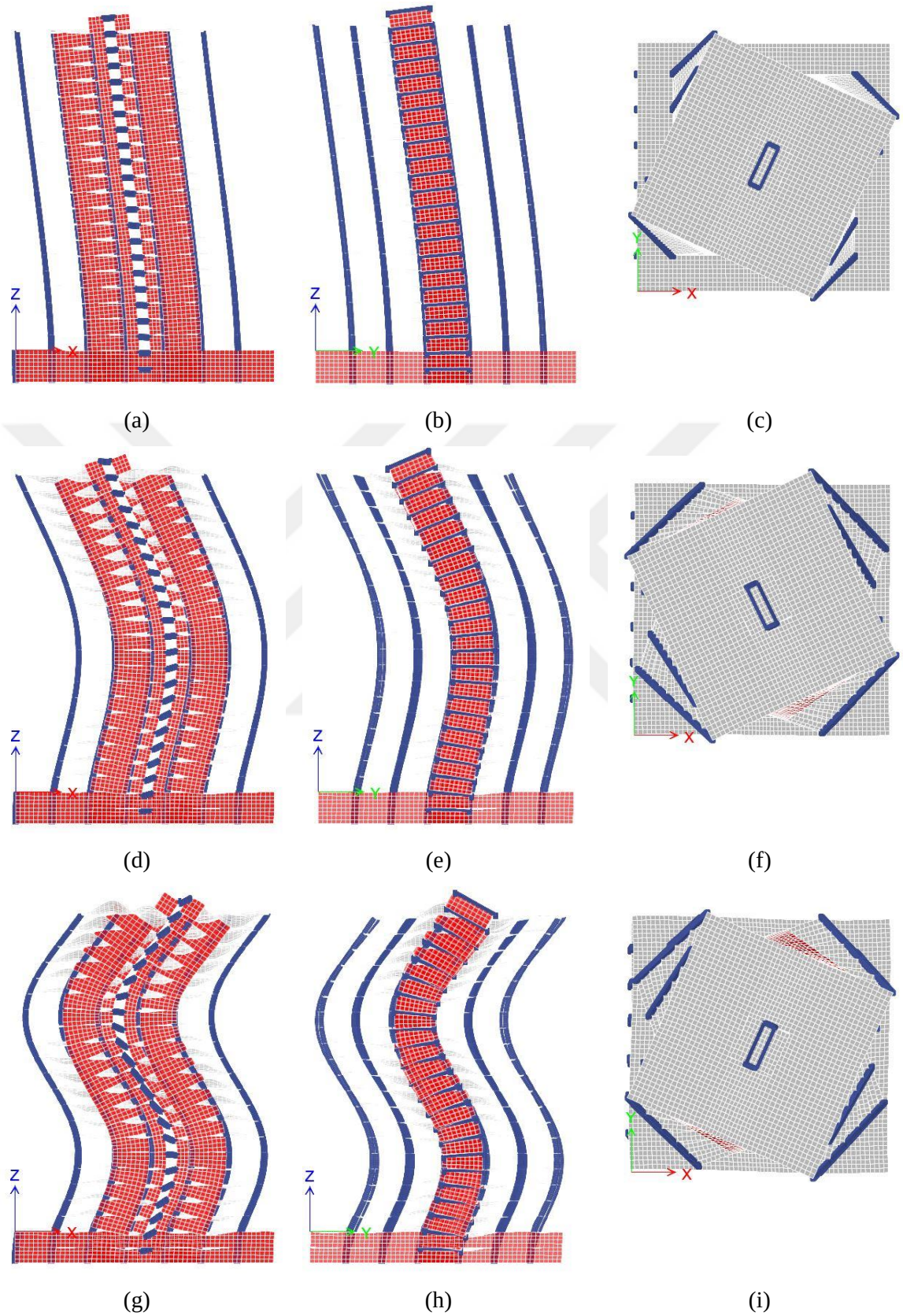

Figure 4.7. First three mode shapes. (a) $T_{X,1}$; (b) $T_{Y,1}$; (c) $T_{B,1}$; (d) $T_{X,2}$; (e) $T_{Y,2}$; (f) $T_{B,2}$; (g) $T_{X,3}$; (h) $T_{Y,3}$; (i) $T_{B,3}$.

4.3. Analysis Results and Design

4.3.1. Response Spectrum Analysis

Response spectrum analysis (RSA) is used for linear elastic design process of prototype building. Motivation of RSA is to compute the peak seismic response of the structure that is valuable especially in the elastic design procedure. Peak responses for each natural mode of vibration, which do not necessarily develop at the same moment in time, are calculated using the design spectrum. Then, calculated responses are combined with a modal combination rule that is square root of sum of squares (SRSS) or complete quadratic combination (CQC). Therefore, demands calculated using RSA results are not exact values for the MDF system, but are accurate enough for design purposes. In this study, the RSA method is applied for design of the high-rise flat plate building.

4.3.2. Design of Slabs and Punching Shear Checks

Determination of optimum dimensions and reinforcement quantities for both slabs and other members is the first step towards a reliable design that satisfies necessary seismic performance criteria. Although there are some rules of thumb to decide on the slab thickness, two different design approaches are discussed to calculate the slab thickness and necessary slab reinforcement amounts based on RSA results.

As a preliminary design, slab thicknesses are defined as 300 mm using Equation 4.12 in TS 500. Punching shear stress upper limit is calculated as $f_{ctd} = 1.65\,\text{MPa}$ for C50 class concrete using Equation 4.13 (TEC 2018).

$$h \geq l_n/30 \qquad h \geq 180\,mm \tag{4.12}$$

$$f_{ctd} = \frac{0.35\sqrt{f_{ck}}}{1.5} \tag{4.13}$$

4.3.2.1. Slab Design Based on Finite Element Analysis. Design calculations for the slab and slab-column connections at the 52.5 m level are presented in this section and in the next section using two alternative design approaches. In the calculations, only the X direction is presented for clarity. Shear stresses in the slab under loading in X direction (S_{13}) are lower than the design tensile strength of concrete along almost the entire slab under load combination 3, which is the most critical combination (Table 4.11). While checking the slab shear stress, overstrength factor D is considered, based on TEC 2018. Half of the 1 m x 1 m meshes near the corner and edge columns are just above the design tensile strength. However, stress jumps around columns may be neglected when the average shear stress in a single mesh is considered. Therefore, these local stress amplifications can be deemed acceptable (Figure 4.8).

Table 4.11. Governing design combinations.

Combination number	Combination
1	$1.4G+1.6Q$
2	$G+Q+0.2S+E_d^{(X)}+0.3E_d^{(Y)}+0.3E_d^{(Z)}$
3	$G+Q+0.2S+D(E_d^{(X)}+0.3E_d^{(Y)})+0.3E_d^{(Z)}$

Slab reinforcement can be designed as ϕ10/150 mm (527 mm^2/m) top reinforcement, ϕ14/150 mm (1027 mm^2/m) additional top reinforcement at slab supports, and ϕ12/150 mm (753 mm^2/m) bottom reinforcement, with a positive moment capacity of $M^+ \approx 73$ kN.m/m, and a negative moment capacity (at slab supports) of $M^- \approx 150$ kN.m/m.

Positive moment capacity is higher than the demands for moments under factored gravity loads, which is the governing combination 1 (Figure 4.9). Under combination 2 (Table 4.11), negative moments are just above the negative moment capacity, but localized moment amplifications can be neglected. Distribution of M_{unb} cannot be noticed in the FEM results; therefore $\gamma_f M_{unb}$ *and* $\gamma_v M_{unb}$ must be calculated manually using the eccentric shear stress method.

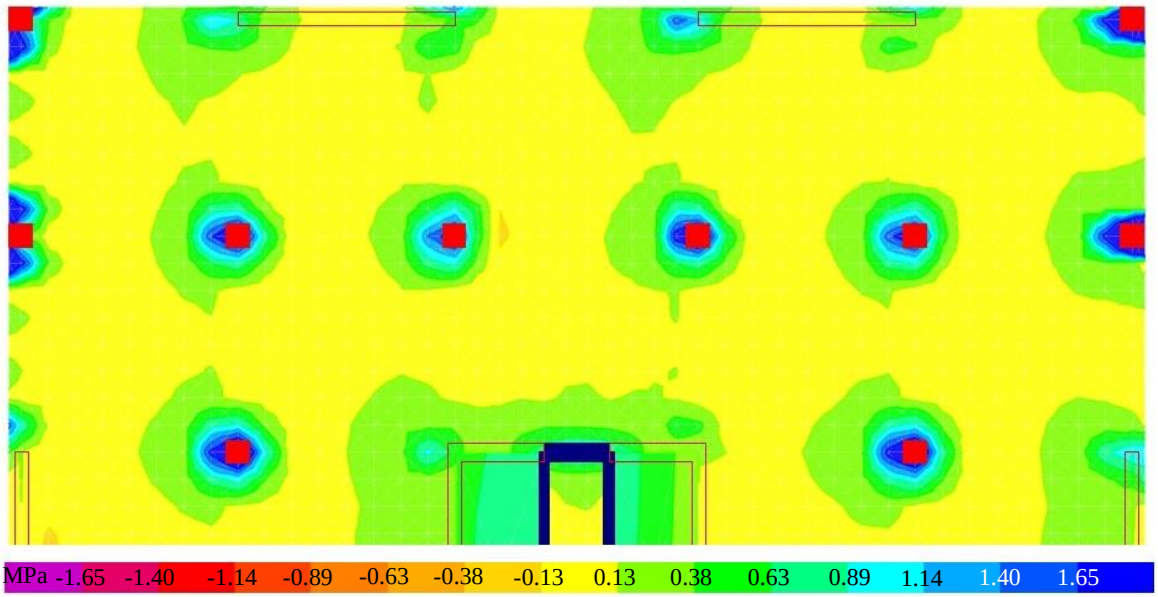

Figure 4.8. Shear stress under earthquake load increased by overstrength factor.

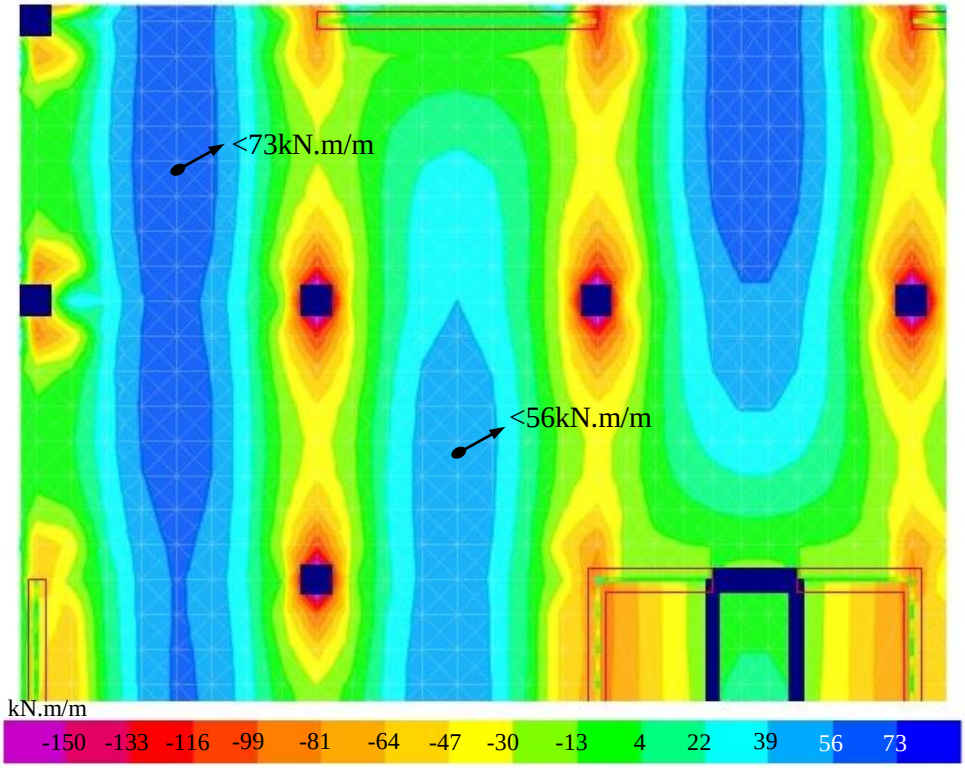

Figure 4.9. Moments in the X direction under factored gravity loads.

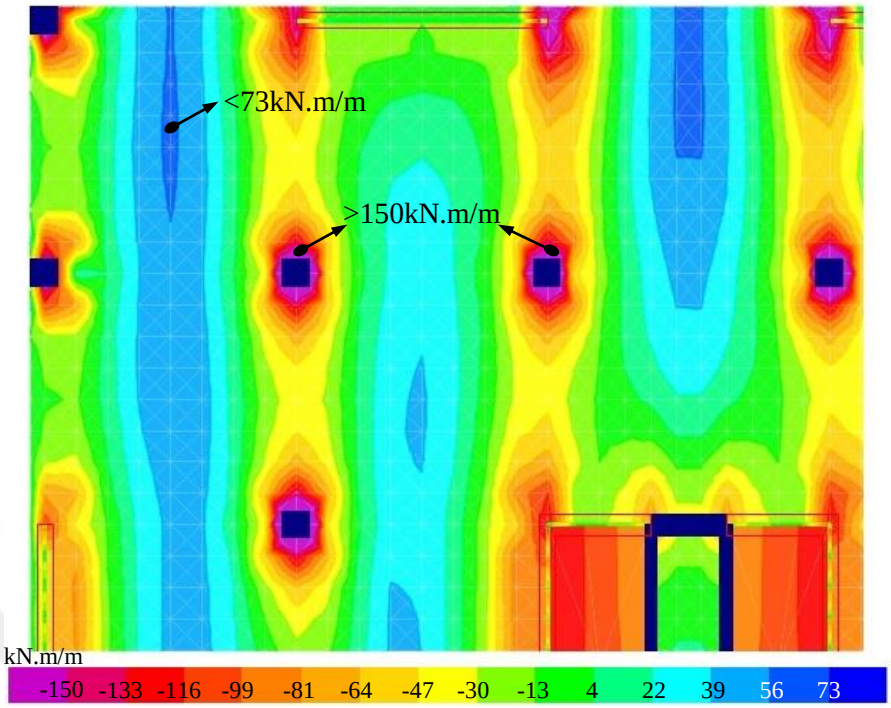

Figure 4.10. Moments in the X direction under earthquake loads.

Design of slab and the slab-column connections is close to design limits in the FEM method. Slab design of is also checked automatically in CSI ETABS. The software calculates punching demand-to-capacity ratios automatically according to TS 500, and it shows similar results with FEM analysis, as shown in Figure 4.11.

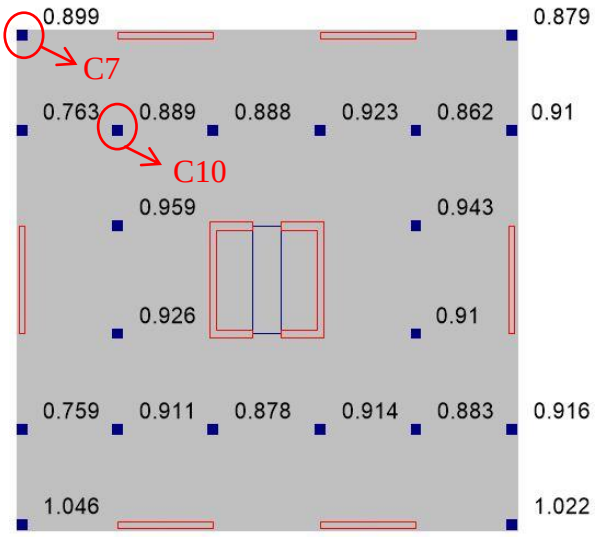

Figure 4.11. Punching shear demand-to-capacity ratios.

4.3.2.2. Eccentric Shear Stress Method. In the recently-published TEC 2018, shear stress distribution in the slab can be calculated using the eccentric shear stress method, with the assumption of $\gamma_f M_{unb}$ resisted by flexural reinforcement and $\gamma_v M_{unb}$ resisted by shear stresses around punching perimeter. Maximum calculated shear stress from the method is used in punching shear check of the slab. Using only the FEM results in design and punching shear check may not be sufficient. It is better to also use the eccentric shear stress method in design.

Representatively, slab-column connection design at an interior column (C10) and a corner column (C7) are conducted using the eccentric shear stress method at 52.5m elevation. However, three different design approaches are considered. In the first approach, structural system overstrength factor (*D*) is used in the shear stress calculations and γ_f is taken as 1.0 at the exterior connections. In second approach, *D* is neglected and γ_f is again taken as 1.0 at exterior connections, which is similar to the ACI 318 design approach. Finally, in the third approach, *D* is used in the calculations and γ_f is calculated using Equation 2.5 for both exterior and interior connections, which is the design approach specified in TEC 2018.

In the calculations for the first approach, the interior slab-column connection C10, which has 90 cm x 90 cm dimensions, 4680 mm punching perimeter (u_p), and 270 mm effective slab depth, is subjected to 1073 kN axial load difference. This unbalanced axial load is transferred to the punching surface as 0.85 MPa uniformly-distributed gravity shear stresses, calculated using Equation 4.14 (Figure 4.12). C10 column has factors $\gamma_f \approx 0.6 \; and \; \gamma_v \approx 0.4$, calculated by Equation 2.5 and 2.6 respectively. Under loading combination 3 (Table 4.11), M_{unb} is 820 kN.m in the loading direction and M_{unb} is 424 kN.m in direction perpendicular to loading direction. The punching shear portion of those unbalanced moments, $\gamma_v M_{unb}$, cause shear stresses of 0.66 MPa and 0.34 MPa in the loading direction and perpendicular to loading direction, respectively (Equation 4.15).

$$v = \frac{V_{ug}}{u_p d} \tag{4.14}$$

$$v = \frac{\gamma_v M_{unb} x}{J} \tag{4.15}$$

The maximum total shear stress is therefore 1.85 MPa, which is exceeds the design tensile strength of concrete. However, this stress level is similar with FEM results and it can be solved by using punching shear reinforcement in the slab.

A portion of the unbalanced moment, $\gamma_f M_{unb}$ of 492 kN.m, should resisted by the sum of the two adjacent slab moment capacities within the moment transfer width $(c+5h)$ Required moment capacity may be calculated as $205\,\text{kN.m/m}$ using Equation 4.16 for the direction of loading under combination 3 (Table 4.11), which is lower than the sum of the two slab moment transfer capacities calculated using FEM analysis $(150+73\,\text{kN.m/m})$. Slab flexural reinforcement calculation in the other direction must be made separately under the appropriate loading combination in the direction of the moment transfer.

$$M^{+}_{c+5h} + M^{-}_{c+5h} = \frac{\gamma_f M_{unb}}{c+5h} \quad [\text{kN.m/m}] \tag{4.16}$$

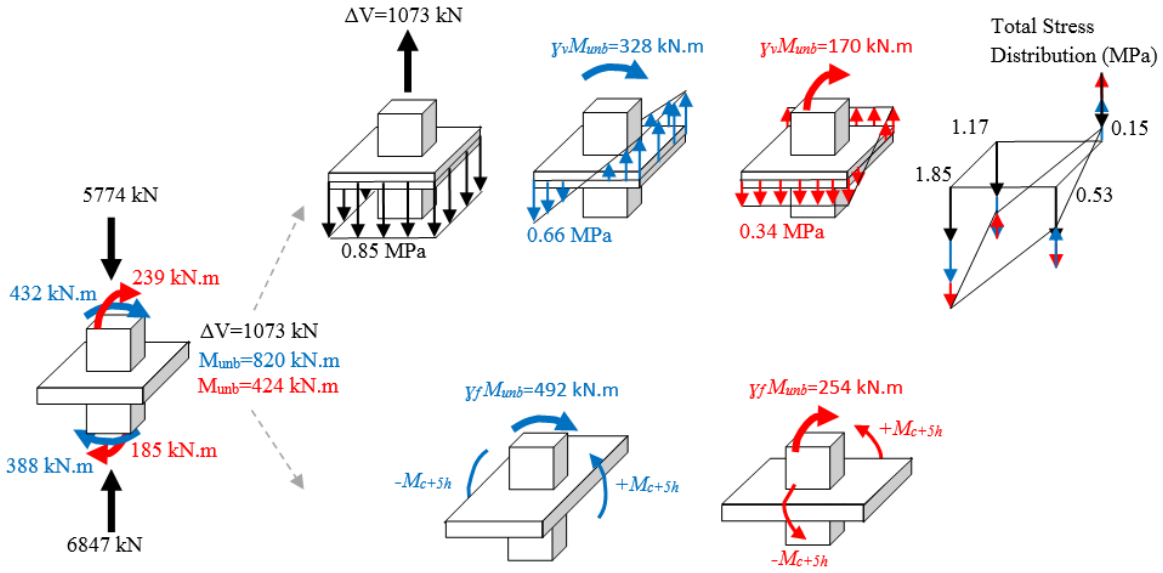

Figure 4.12. Distribution of unbalanced moments at an interior column.

Corner slab-column connection of C7, which has 90 cm x 90 cm dimensions, 2070 mm punching perimeter (u_p), and 270 mm effective slab depth, is subjected to 312 kN axial load difference. This unbalanced axial load causes 0.56 MPa uniformly distributed gravity shear stress calculated using Equation 4.14. Gravity shear stress ratio can be calculated as 0.32. γ_f can be taken 1 for the corner column C7 because gravity shear stress ratio is lower than the permitted value, 0.5, according to ACI 318 using Equation 4.17. Under loading combination 3 (Table 4.11), unbalanced moments, M_{unb}, are 917 kN.m and 380 kN.m in the loading direction (for positive and negative directions), and 452 kN.m and 24 kN.m in perpendicular to loading direction.

$$v_{ug} < 0.5\phi v_c \tag{4.17}$$

All of the unbalanced moment, $\gamma_f M_{unb}$ of 917 kN.m, should resisted by top flexural reinforcement within the slab moment transfer width ($c+2.5h$) for the corner C7 connection, and all of the unbalanced moment under loading in the opposite direction, $\gamma_f M_{unb}$ is 380 kN.m, should resisted by bottom flexural reinforcement within the slab moment transfer width ($c+2.5h$). Required moment capacities are 555 kN.m/m and 230 kN.m/m for top and bottom flexural reinforcement under combination 3 (Equation 4.18 and Table 4.11). Slab flexural reinforcement designed based on FEM analysis results is not sufficient to resist these moments; therefore, slab reinforcement revision must be conducted. Distribution of unbalanced moments can be seen in Figure 4.13.

$$M^{\mp}_{c+2.5h} = \frac{\gamma_f M^{\mp}_{unb}}{c+2.5h} \quad [\text{kN.m/m}] \tag{4.18}$$

At this stage, it would be worthwhile to investigate whether design based on FEM analysis results would sufficient the same corner column connection C7, if it was designed using the TEC 2018 code, taking $\gamma_f \approx 0.6$ instead of 1. In that case, this unbalanced axial axial load again causes 0.56 MPa uniformly distributed gravity shear stress, but the column has factors $\gamma_f \approx 0.6 \; and \; \gamma_v \approx 0.4$ calculated by Equation 2.5 and 2.6 respectively. Under

loading combination 3 (Table 4.11), unbalanced moments, M_{unb}, are 917 kN.m and 380 kN.m in the loading direction, and 452 kN.m and 24 kN.m perpendicular to the loading direction. $\gamma_v M_{unb}$, causes shear stresses of 4.46 MPa and 2.20 MPa in the loading direction and perpendicular to loading direction, respectively (Equation 4.15).

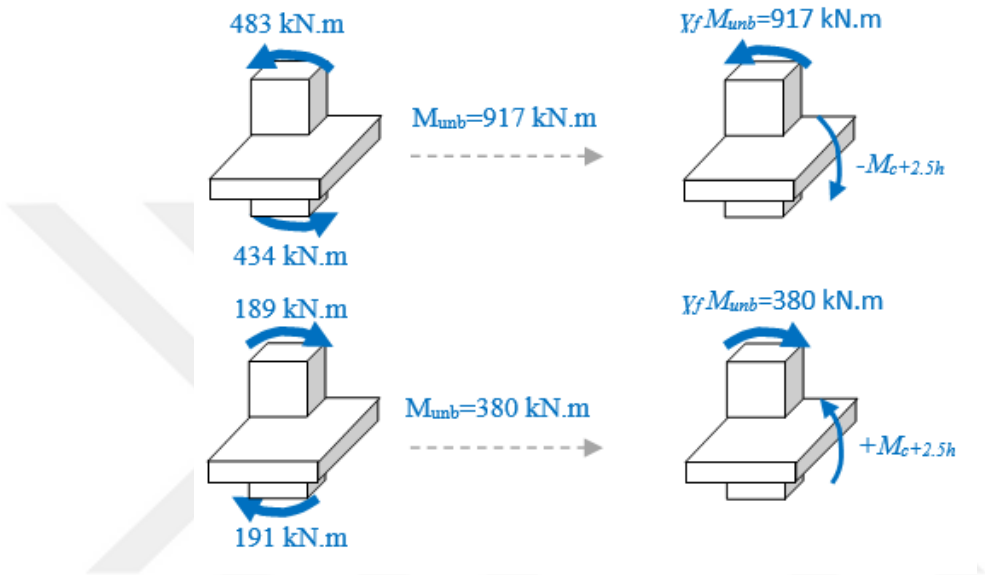

Figure 4.13. Distribution of unbalanced moments at a corner column.

The maximum total shear stress is therefore 3.17 MPa which is much higher than the concrete design tensile strength of 1.65 MPa (Figure 4.14). Moreover, the calculated stress level is also higher than $1.5 f_{ctd}$ which is the maximum shear stress limit with punching shear reinforcement. Therefore, column cross-sectional directions or slab thickness needs to be increased to avoid punching shear failure. It is important to note that such large shear stresses in the slab at the corner connection were not seen in the FEM analysis results.

$\gamma_f M_{unb}$ of 550 kN.m and 228 kN.m in the loading direction should be resisted by moment capacities of top and bottom reinforcement along the slab moment transfer width $(c+2.5h)$ respectively (Figure 4.15). Therefore, required total moment capacities can be found as $333\,\text{kN.m/m}$ and $138\,\text{kN.m/m}$ by Equation 4.18, for top and bottom slab reinforcement under load combination 3 (Table 4.11). The required amount of slab flexural

reinforcement found according to FEM analysis results is not enough to overcome the flexural demands in the slab either. Therefore, the TEC 2018 eccentric shear stress method requires additional slab flexural reinforcement (within the slab moment transfer width) compared to FEM results, and also requires increasing column cross-sectional dimensions to decrease shear stresses in the slab.

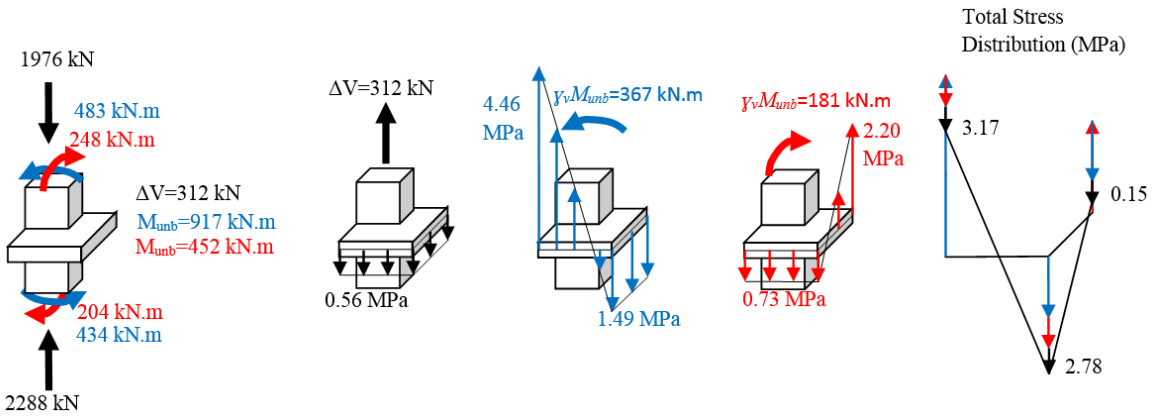

Figure 4.14. Distribution of unbalanced moments at a corner column.

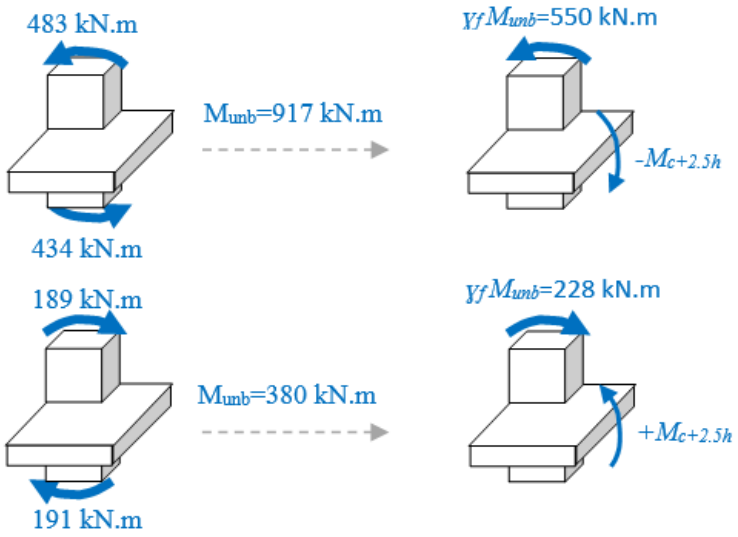

Figure 4.15. Distribution of unbalanced moments at corner column.

In second design approach, overstrength factor *D* is neglected, but γ_f is again taken as 1.0 at exterior connections, similarly to ACI 318. In the third design approach, *D* is

considered in slab shear stress calculations; however, γ_f is calculated by Equation 2.5 for both exterior and interior connections, according to TEC 2018. A corner column calculation is investigated thoroughly as part of the third approach, to show slab shear stress distribution and magnitude. Calculated reinforcement amounts for all three design approaches are listed in Table 4.12, with respect to both the eccentric shear stress method and FEM analysis.

Table 4.12. Slab reinforcement configurations.

	Interior connection and Edge connection loading direction parallel to the edge			Corner connection and Edge connection loading direction perpendicular to the edge			
	Add. Top Rein. (mm)	Top Rein (mm).	Bottom Rein. (mm)	Add. Top Rein. (mm)	Top Rein. (mm)	Add. Bottom Rein. (mm)	Bottom Rein. (mm)
FEM	ϕ14/150	ϕ10/150	ϕ12/150	ϕ14/150	ϕ10/150	-	ϕ12/150
ESSM 1	ϕ16/150	ϕ10/150	ϕ14/150	ϕ24/80	ϕ10/150	ϕ18/150	ϕ14/150
ESSM 2	ϕ14/150	ϕ10/150	ϕ12/150	ϕ22/100	ϕ10/150	-	ϕ12/150
ESSM 3	ϕ14/150	ϕ10/150	ϕ12/150	ϕ14/150	ϕ10/150	-	ϕ12/150

In the design using the eccentric shear stress (ESS) method and design approach 3 (named as design case ESSM3, based on TEC 2018), corner slab-column connection C7 at 63 m elevation has 1300 mm x 1300 mm column cross-sectional dimensions (increased from 900 mm to 1300 mm to avoid punching shear failure), 2870 mm punching perimeter (u_p), and 270 mm effective slab depth carries 318 kN unbalanced axial load. This unbalanced axial load is transferred to the punching perimeter surface as 0.41 MPa uniformly distributed gravity shear stresses calculated using Equation 4.14 (Figure 4.16). Column C7 has factors $\gamma_f \approx 0.6 \, and \, \gamma_v \approx 0.4$ calculated by Equation 2.5 and 2.6 respectively. Under loading combination 3 (Table 4.11), obtained M_{unb} is 492 kN.m in the

loading direction and 283 kN.m in the perpendicular direction. $\gamma_v M_{unb}$, causes shear stresses of 1.26 MPa and 0.72 MPa in the loading direction and perpendicular to loading direction (Equation 4.15). In ESSM 3, larger corner and edge column dimensions (1300 mm instead of 900 mm in all other design approaches) are necessary to decrease slab shear stress at corner and edge connections. Therefore, it is seen that the maximum total shear stress is 1.07 MPa, which is lower than the design tensile strength of concrete, not necessitating punching shear reinforcement at the connection.

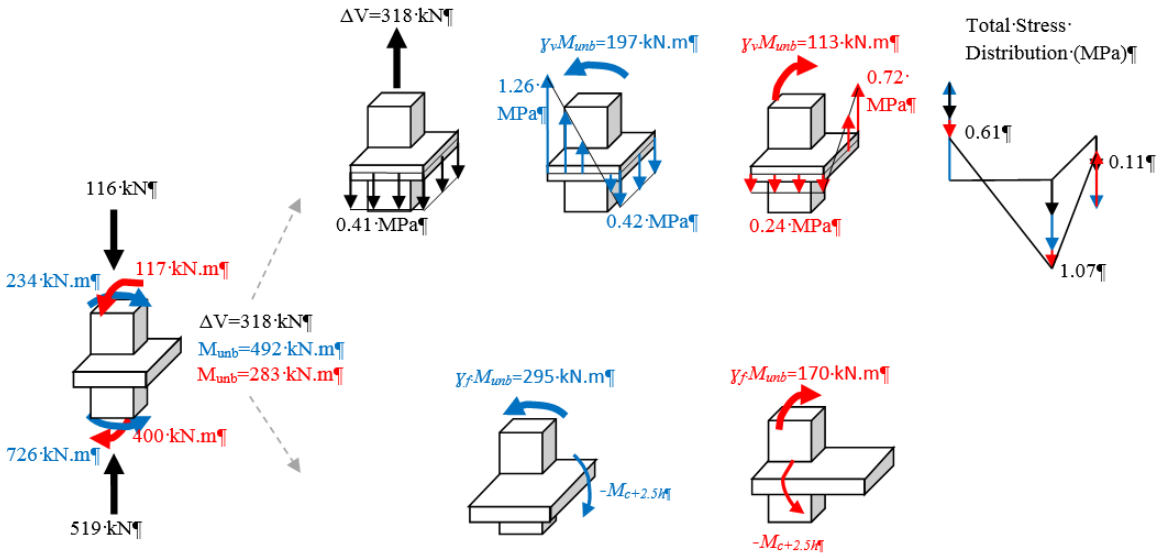

Figure 4.16. Distribution of unbalanced moments at a corner column.

In this case, $\gamma_f M_{unb}$ values of 295 kN.m and 170 kN.m must be resisted by slab moment capacities within the moment transfer width $(c+2.5h)$. Therefore, required moment capacities can be found as 144 kN.m/m and 83 kN.m/m using Equation 4.18 for the both directions under load combination 3 (Table 4.11). Required slab flexural reinforcement found by FEM analysis results is adequate to develop these capacities.

Therefore, the TEC 2018 approach using the eccentric shear stress method for slab-column connection design can be deemed safe. However, it may require significant increase in the cross-sectional dimensions of edge and corner columns in order to satisfy punching shear requirements in the slabs.

4.3.3. Drift-Based Check and Comparative Evaluation

In RSA results, maximum drift ratios in the X and Y directions are around 0.011 and 0.012. Necessity of punching shear reinforcement for an interior column C10 (Figure 4.11) is evaluated using Equation 2.13 in compliance with ACI 318. Gravity shears on columns are drawn from combination $G+Q+0.2S+0.3E_d^{(Z)}$ and strength reduction factor, ϕ and v_c are taken as 0.75 and 2.33 MPa respectively. Gravity shear ratio calculation details are in Table 4.13.

Table 4.13. Gravity shear ratio details.

Story	Dimension (cm)	$V_{ug}\ (kN)$	$u_p d\ (mm^2)$	$\frac{v_{ug}}{\phi v_c}$
20th NF	90x90	1099	1263600	0.50
19th NF	90x90	1085	1263600	0.49
18th NF	90x90	1088	1263600	0.49
17th NF	90x90	1089	1263600	0.49
16th NF	90x90	1090	1263600	0.49
15th NF	90x90	1092	1263600	0.49
14th NF	90x90	1094	1263600	0.50
13th NF	90x90	1096	1263600	0.50
12th NF	90x90	1099	1263600	0.50
11th NF	90x90	1102	1263600	0.50
10th NF	100x100	1105	1371600	0.46
9th NF	100x100	1107	1371600	0.46
8th NF	100x100	1111	1371600	0.46
7th NF	100x100	1114	1371600	0.46
6th NF	100x100	1118	1371600	0.47
5th NF	110x110	1124	1479600	0.43
4th NF	110x110	1127	1479600	0.44
3rd NF	110x110	1131	1479600	0.44
2nd NF	110x110	1135	1479600	0.44
1st NF	120x120	1142	1587600	0.41

Design story drift ratio under DD2 level ground motion and shear gravity ratio are parameters to define shear reinforcement requirement using Equation 2.13 (Figure 4.17). Around 0.50 gravity shear ratio for interior 90 cm x 90 cm columns at 56 m elevation is slightly above the limit so that punching shear reinforcement must be used at those stories. In FEM results that were discussed in slab design section, a small region (stress concentration) was above the concrete design tensile strength for the interior column at 56 m elevation (Figure 4.8). It can be considered as below the limit or with a conservative approach, punching shear reinforcement can be used. CSI ETABS can do the punching check automatically and gives the demand-to-capacity ratio as 0.93 for the interior columns as shown in Figure 4.11. As a fourth alternative, using the eccentric shear stress method gives around 1.85 MPa shear stresses, which is just above the limit for the interior column at the same elevation and shear reinforcement is therefore also needed (Figure 4.12). Overall, it can be concluded that the four different design approaches give similar outcomes for the interior columns.

For the edge and corner columns using Equation 2.13 underestimates shear stresses because corner and edge columns have smaller tributary area so that they have smaller gravity shear ratio, and as a result they are below the limit. However, Equation 2.13 is probably derived to evaluate the entire system or an entire story in terms of punching shear. And only result can be derived as system is around the limits. In FEM, nearly half of the mesh is above the design tensile strength for edge and corner columns at 56 m elevations but it may be deemed acceptable, or to be on the safe side, punching shear reinforcement can be used (Figure 4.8). CSI ETABS software calculates demand-to-capacity ratio for punching shear as around 1.0 for the corner columns, as shown in Figure 4.11. However, using the eccentric shear stress method, obtained shear stresses are too large to resist even with shear reinforcement (Figure 4.14). This problem can be solved two ways, either all unbalanced moment that causes high shear stresses should be resisted by added flexural reinforcement within slab moment transfer width with the assumption of $\gamma_f = 1$ (the ACI 318-14 approach), or slab shear stresses should be decreased by increasing column cross-sectional dimensions or slab thickness, while still using the assumption that $\gamma_f \approx 0.6$ (the TEC 2018 approach), which is less preferable design. It should be noted that

FEM results and ESSM results for punching shear stresses around edge and corner columns maybe significantly different.

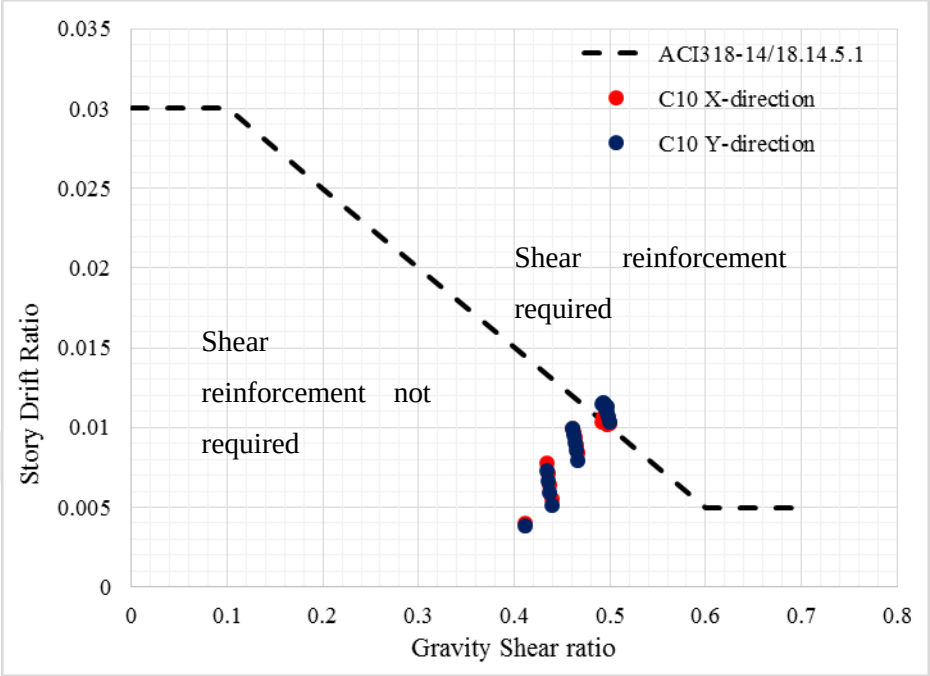

Figure 4.17. Design story drift ratio versus gravity shear ratio.

5. SEISMIC PERFORMANCE OF THE PROTOTYPE STRUCTURE

5.1. Nonlinear Modeling

Realistic simulation of a structure's nonlinear behavior is overcome complicated process. Ideally, nonlinear behavior of every structural member must be modeled to obtain the most reliable nonlinear response prediction, both for individual members and for the overall structural system. Uncertainty in the expected ground motion characteristic is other difficulty that further complicates the performance assessment. Moreover, nonlinear response history analysis of structures is a time consuming and computationally demanding process. Therefore, to expedite the analyses, some of the structural (e.g., slabs, basement walls) and non-structural (e.g. partition walls) elements are defined with linear elastic behavior, or even excluded from the analytical model. Despite all these complexities, it is still possible to construct a nonlinear model that can reliably simulate the nonlinear seismic response of real-life structure, with recent enhancements in computational tools and experimental observations on the nonlinear behavior of structural components and systems.

In this study, nonlinear modeling and analysis of the prototype building structure is conducted using the most commonly-employed industry-standard commercial software, CSI Perform 3D. In nonlinear modeling and performance assessment, specifications in TEC 2018 and recommendations in ASCE 41 are both utilized.

5.1.1. Material Properties

As expected material strengths, expected compressive strength of concrete, f_{ce}, is calculated as 65 MPa, and expected yield strength of reinforcement, f_{sye}, is calculated as 504 MPa with respect to TEC2018.

5.1.1.1. Elastic Material for Fiber Sections. Nonlinear behavior of basement walls is not expected due to large cross sections and capacities. Therefore, these elements are modeled

using linear elastic wall elements. Modulus of elasticity of the linear elastic elements is defined as $E_{ce} = 38574\,\text{MPa}$, using Equation 5.1 of TS EN 1992-1-1 (Turkish Standard Institute, 2009).

$$22000\left(\frac{f_{ce}}{10}\right)^{0.3} \tag{5.1}$$

5.1.1.2. Elastic Shear Modulus of Walls. Capacity design approach was used in shear design of structural walls. Nonlinear shear deformation is not expected in structural walls and walls shear behavior is modeled linear elastically by defining an Elastic Shear Material in CSI Perform 3D, using Equation 4.2, with a shear modulus of $G_{ce} = 16072\,\text{MPa}$.

5.1.1.3. Elastic Modulus for Slabs. In design, slabs are not considered as a part of the seismic load resisting system, so they are usually not included in nonlinear models, or they are modeled using linear elastic shell elements .In this study, some of the models generated have linear elastic slab elements for comparison with other models that consider nonlinearity in slabs. Elastic Material for the slabs is defined as $E_{ce} = 38574\,\text{MPa}$ in the models with linear elastic slab elements.

5.1.1.4. Concrete. A theoretical stress-strain model for both unconfined and confined concrete is used in nonlinear response history analysis (Mander *et al.*, 1988). To generate the confined and unconfined concrete stress-strain relationships defined in the model, Equation 5.2 is used, which is also suggested in TEC 2018.

$$f_c = \frac{f_{cc}xr}{r-1+x^r} \tag{5.2}$$

Relationship between f_{cc} and f_{co} is shown by Equation 5.3:

$$f_{cc} = \lambda_c f_{co} \tag{5.3}$$

where λ_c is calculated by Equation 5.4,

$$\lambda_c = 2.254\sqrt{1+7.94\frac{f_e}{f_{co}}} - 2\frac{f_e}{f_{co}} - 1.254 \tag{5.4}$$

where effective confining pressure, f_e , is found from Equation 5.5 and 5.6 below:

$$f_{ex} = k_e \rho_x f_{yw} \tag{5.5}$$

$$f_{ey} = k_e \rho_y f_{yw} \tag{5.6}$$

Then, the confinement effectiveness coefficient, k_e , is formulated as

$$k_e = \left(1-\frac{\sum a_i^2}{6b_o h_o}\right)\left(1-\frac{s}{2b_o}\right)\left(1-\frac{s}{2h_o}\right)\left(1-\frac{A_s}{b_o h_o}\right)^{-1} \tag{5.7}$$

Finally, to generate stress-strain relationship, Equations 5.8 to 5.10 are needed.

$$x = \frac{\varepsilon_c}{\varepsilon_{cc}} \tag{5.8}$$

$$\varepsilon_{cc} = \varepsilon_{co}\left[1+5\left(\lambda_c - 1\right)\right] \tag{5.9}$$

$$r = \frac{E_c}{E_c - E_{\text{sec}}} \tag{5.10}$$

where the secant modulus of elasticity of confined concrete is defined as in Equation 5.11.

$$E_{\text{sec}} = \frac{f_{cc}}{\varepsilon_{cc}} \tag{5.11}$$

In the concrete stress-strain calculations, unconfined concrete modulus of elasticity is calculated as $E_c = 40311\,\text{MPa}$, using Equation 5.12.

$$E_c = 5000\sqrt{f_{co}} \tag{5.12}$$

After plotting the concrete stress-strain relationships for the fiber sections, stress-strain curves are converted to simplified polylines and linearized stress-strain models are categorized to minimize number of typical fiber models according to their similarity (Figure 5.1 and Table 5.1). Cyclic degradation of concrete stress-strain behavior and the tensile strength of concrete are ignored in the fiber models adopted for structural walls.

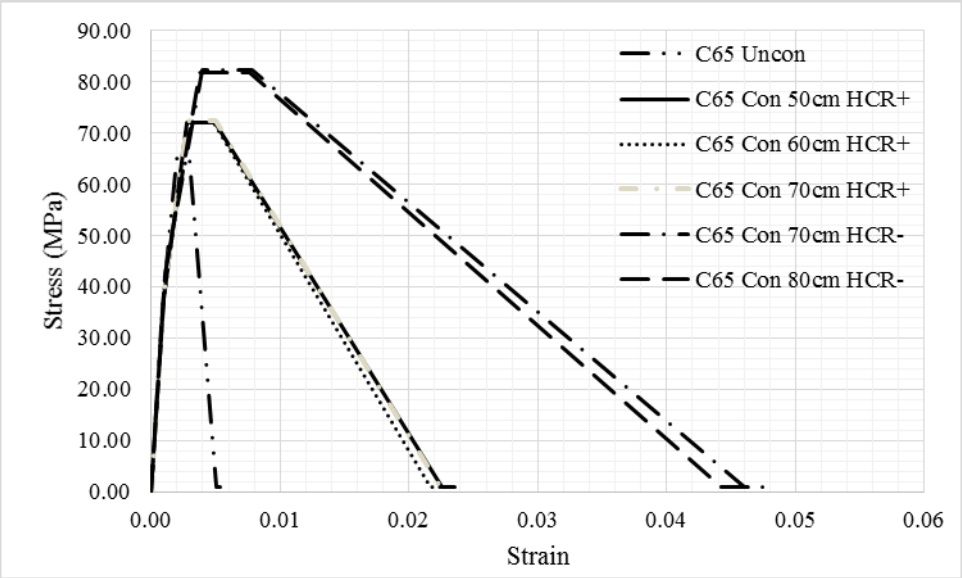

Figure 5.1. Linearized stress-strain relationship of concrete.

Table 5.1. Fiber modeling parameters for concrete material.

Material Label	DY	DU	DL	DR	DX	FY	FU=FL	FR=FX
C65 Unconfined	0.0009	0.0020	0.0030	0.0050	0.0053	36.29	65.00	0.98
C65 Confined 50cm HCR+	0.0009	0.0028	0.0049	0.0226	0.0236	37.67	72.12	1.01
C65 Confined 60cm HCR+	0.0009	0.0028	0.0048	0.0217	0.0229	37.58	71.88	1.01
C65 Confined 70cm HCR-	0.0011	0.0040	0.0078	0.0460	0.0485	42.78	82.36	0.99
C65 Confined 80cm HCR-	0.0011	0.0038	0.0076	0.0442	0.0465	42.44	81.73	0.98
C65 Confined 70cm HCR+	0.0009	0.0028	0.0050	0.0224	0.0236	37.74	72.26	1.01

5.1.1.5. Reinforcement. B420C reinforcing steel stress-strain model is generated according to TEC 2018. Modulus of elasticity, $E_s = 200000\,\text{MPa}$, expected yield strength, $f_{sye} = 504\,\text{MPa}$, and expected ultimate strength, $f_{sue} = 605\,\text{MPa}$, are taken as shown in Table 5.2. The stress-strain relationship is plotted according to Equations 5.13 to 5.15 (Figure 5.2). Buckling behavior of reinforcing steel is neglected in modeling.

$$f_s = E_s \varepsilon_s \qquad \left(\varepsilon_s \le \varepsilon_{sy}\right) \tag{5.13}$$

$$f_s = f_{sy} \qquad \left(\varepsilon_{sy} < \varepsilon_s \le \varepsilon_{sh}\right) \tag{5.14}$$

$$f_s = f_{su} - \left(f_{su} - f_{sy}\right)\frac{\left(\varepsilon_{su} - \varepsilon_s\right)^2}{\left(\varepsilon_{su} - \varepsilon_{sh}\right)^2} \qquad \left(\varepsilon_{sh} < \varepsilon_s \le \varepsilon_{su}\right) \tag{5.15}$$

Table 5.2. Steel mechanical properties.

Steel Class	E_s (MPa)	f_{sye}	ε_{sh}	ε_{su}	f_{sue}/f_{sye}
B420C	200000	504	0.008	0.08	1.2

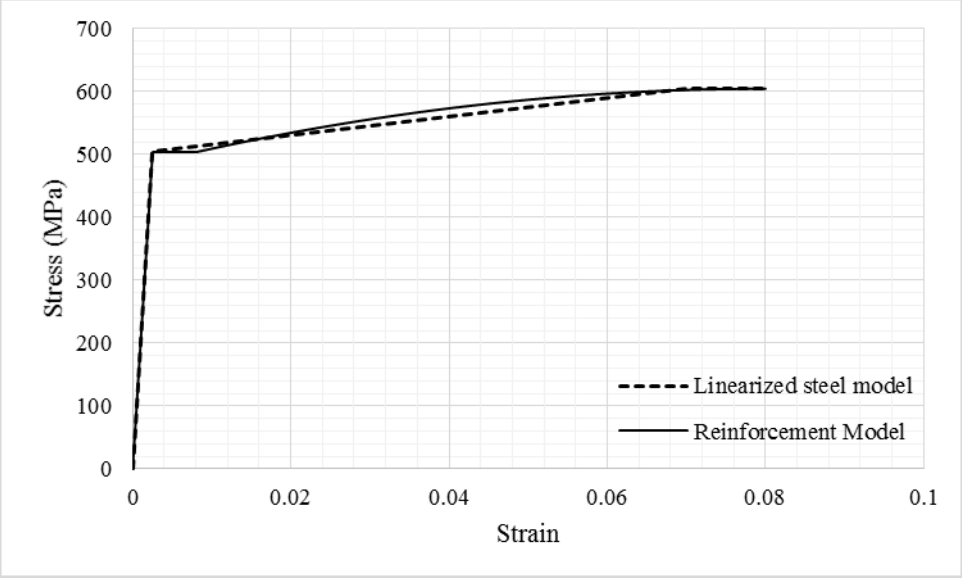

Figure 5.2. Stress-strain relationship of reinforcement.

5.1.2. Gravity Loads

Nonlinear behavior of columns and structural walls are highly dependent on gravity loads. Second order effects on the structure are also dependent on gravity loads. Therefore, determination of gravitational loads is an important stage of nonlinear analysis. In addition, seismic masses are defined from the gravity loads. Therefore, the assigned gravity load values in the model must be as realistic as possible. Similarly to linear elastic analysis, self weight and superimposed dead loads are assigned directly to the model, whereas live loads are assigned after live load participation factors are applied.

5.1.3. Seismic Loads

5.1.3.1. Determination of Target Spectrum. A similar procedure to generating the elastic design spectrum is followed for determining the target spectrum for nonlinear analysis, except a different earthquake hazard level, a different damping ratio, and other relevant specifications for performance based design.

Short and long period spectral acceleration coefficients are obtained from the Turkish Earthquake Hazard Map website for the hypothetical project location (41°00’00.0”N, 28°42’00.0”E) and the DD1 ground motion level, which is defined in TEC 2018 as a ground motion with probability of exceedance of 2% in 50 years, and reoccurrence period of 2475 years (Table 5.3).

Table 5.3. Spectral acceleration coefficients for DD1 at hypothetical project location.

	S_S	S_1
DD1	2.045	0.567

Design spectral accelerations are calculated using Equations 4.3 and 4.4 considering suitable local soil effect coefficients which are $F_s = 1.2$ for short period and $F_1 = 1.433$ for one second period at the site location (Table 5.4)

Table 5.4. Design spectral accelerations for DD1 ground motion level.

	S_{DS}	S_{D1}
DD1	2.454	0.813

Finally, the target spectrum is generated using Equations 4.5 to 4.8, and as a last step, the generated spectrum is increased by 1.3 times between $0.2T_p$ and $1.5T_p$, where T_p is the first mode fundamental natural vibration period of the building ($T_{x,1}$ = 3.081 s and $T_{y,1}$ = 3.065 s). Spectral accelerations in the average resultant spectrum of selected ground motions, where the resultants are calculated using the SRSS rule, must not be smaller than the increased target spectrum, as stated in TEC 2018. Both the target spectrum and the increased target spectrum are presented in Figure 5.3.

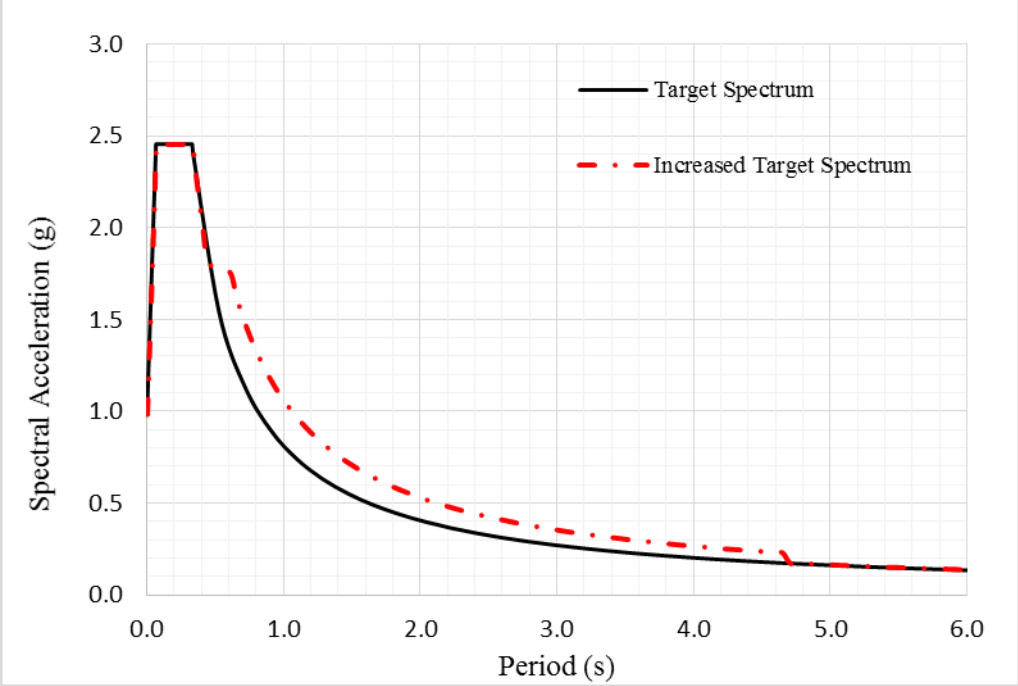

Figure 5.3. Target spectra for DD1 ground level motion.

5.1.3.2. Selection and Scaling of Earthquake Ground Motion Records. Ground motion records should be chosen carefully to obtain reliable results from nonlinear response history analysis. In selecting ground motions from a database, there some key parameters

that must be considered, such as fault mechanism, magnitude, shear wave velocity ($V_{s,30}$), and closest distance from project location to projection of rupture surface (R_{JB}).

Many records are listed in databases according to these parameters. A statistical method (mean square error, MSE) is used to decide the most suitable set of ground motions. Mean squared error is a method to calculate the mean error with respect to differences between spectral accelerations of a record and target spectrum, for a specified period range, using Equation 5.16. NGAWest2 Ground Motion Database (PEER, 2013) is used to select the earthquake ground motion records.

$$MSE = \frac{1}{N}\sum_{i=1}^{N} w_i \left(S_{aeT} - S_{aeR}\right)^2 \tag{5.16}$$

After choosing the most suitable records for the target spectrum, ground motions are linearly scaled to match target spectrum (amplitude scaling). According to TEC 2018, at least 22 ground motion record pairs must be chosen and a maximum three of record pairs can be chosen from the same earthquake. Lastly, average SRSS spectrum of the selected ground motion records must not be smaller than the increased target spectrum.

Filtering parameters for DD1 level ground motions are as follows:

- Mechanism: Strike-slip
- Magnitude range: 6.5-7.4
- $V_{s,30}$ range: 350-750 m/s
- R_{JB}: 10-65 km

Mean of the SRSS acceleration and displacement spectra calculated for the scaled ground motions are compared with the increased target acceleration and displacement response spectra in Figure 5.4 and 5.5. The selected ground motions and their characteristics are listed in Table 5.5.

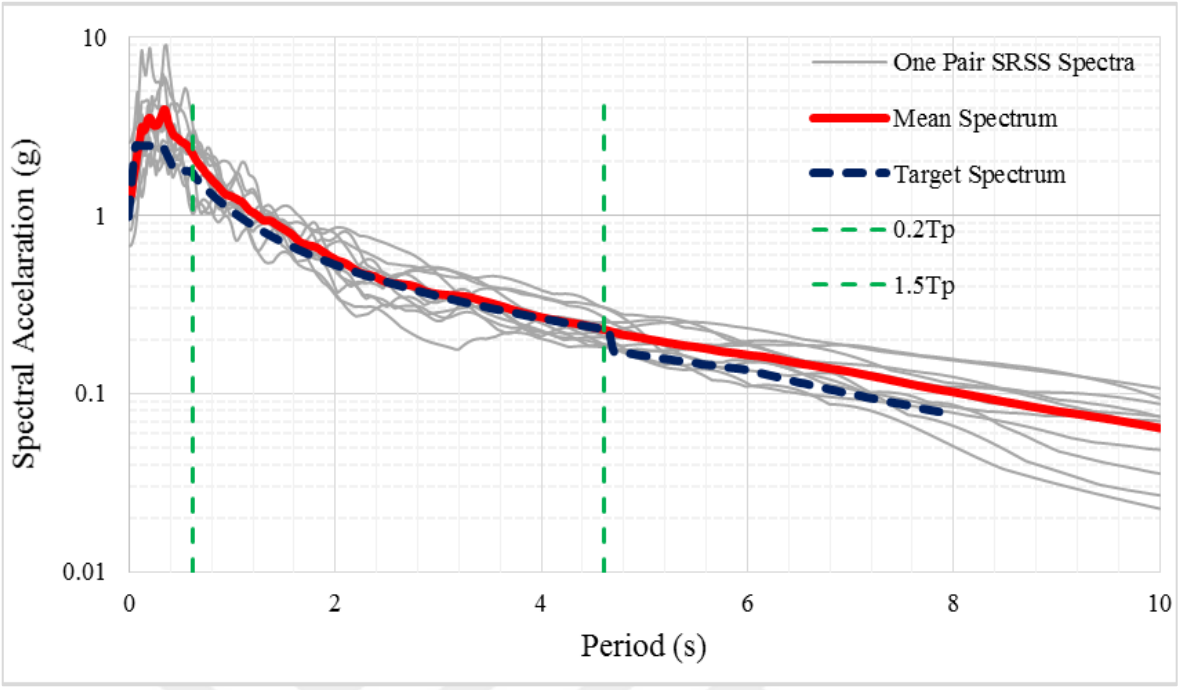

Figure 5.4. Mean and target acceleration spectra for DD1 ground motion level.

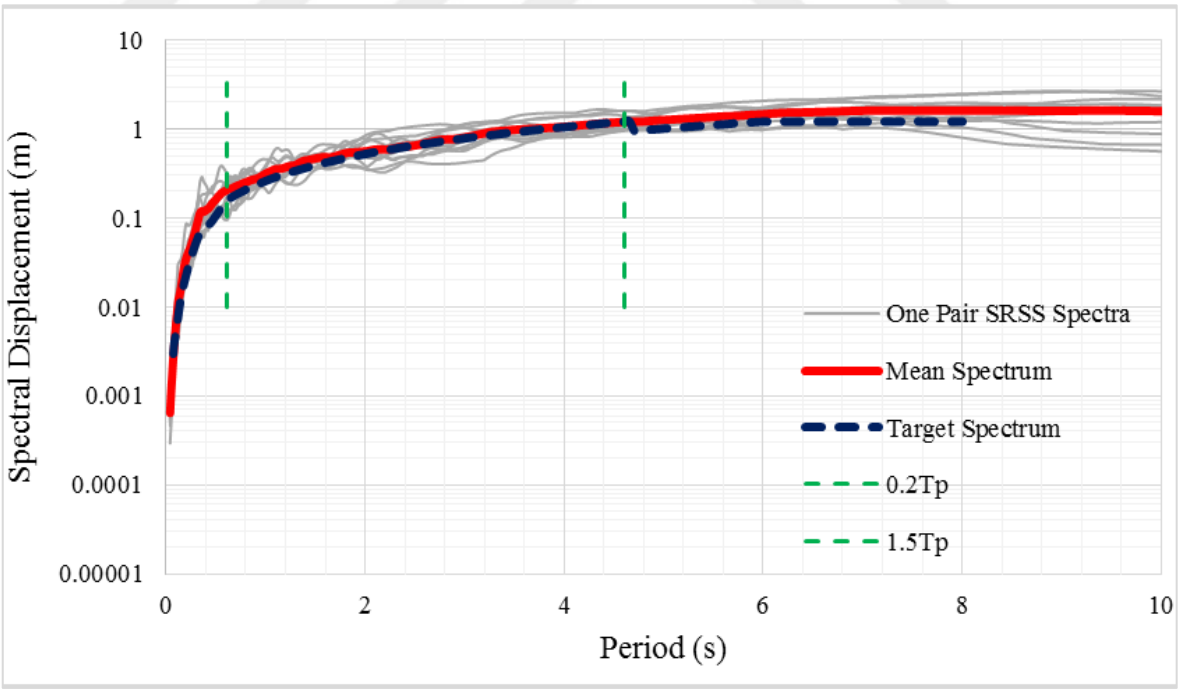

Figure 5.5. Mean and target displacement spectra for DD1 ground motion level.

Table 5.5. Ground motion properties for DD1 earthquake level.

Record Sequence Number	Earthquake Name	Scale Factor	Magnitude	Mechanism	R_{JB} (km)	$V_{s,30}$ (m/s)
RSN164	Imperial Valley	4.78	6.53	Strike-Slip	15.2	472
RSN762	Loma Prieta	7.32	6.93	Reverse Oblique	39.3	368
RSN1614	Duzce	7.50	7.14	Strike-Slip	11.5	481
RSN1633	Manjil	1.80	7.37	Strike-Slip	12.6	724
RSN1768	Hector Mine	8.62	7.13	Strike-Slip	61.2	370
RSN1770	Hector Mine	6.70	7.13	Strike-Slip	61.9	407
RSN1816	Hector Mine	7.75	7.13	Strike-Slip	61.9	368
RSN3749	Cape Mendocino	2.57	7.01	Reverse	16.5	355
RSN3752	Landers	8.09	7.28	Strike-Slip	45.3	436
RSN4852	Chuetsu-oki	8.16	6.80	Reverse	30.3	606
RSN6948	Darfield	6.62	7.00	Strike-Slip	30.6	482

5.1.4. Load Combinations

In the nonlinear analysis model, dead loads, live loads, and earthquakes loads are combined using Equation 5.17 and 5.18, according to TEC 2018.

$$G + Q_e + 0.2S + E_d^{(H)} \tag{5.17}$$

where

$$Q_e = nQ \tag{5.18}$$

5.1.5. Masses

Automatically-assigned joint masses by CSI ETABS software in the linear elastic analysis model are exported to CSI Perform 3D software for assembling the nonlinear analysis model. Masses are assigned in both directions of the model.

5.1.6. Modeling of Structural Elements

Nonlinear behavior of the members can be modeled using two different approaches, the lumped plasticity model (plastic hinge model) and the distributed plasticity model (fiber model). In the lumped plasticity approach, plastic hinges are placed in zones where damage (nonlinear behavior) expected. Then, force vs. plastic deformation (e.g., moment vs. plastic rotation) relationships are introduced to the hinges to represent nonlinear behavior of that region. In the distributed plasticity approach, a cross section is divided into fibers (using the plane sections remain plane assumption) where uniaxial fiber behavior consists of simplified material stress-strain models, and the fiber element represents both axial and bending behavior of the structural member distributed along its length. Nonlinear behavior of structural walls are modeled using the distributed plasticity method (fiber elements) and nonlinear behavior of effective slab beams, coupling beams, and columns are represented using the lumped plasticity method in this study.

5.1.6.1. Structural Walls. Structural walls are main members that provide lateral rigidity and lateral load resisting capacity of tall building systems. Therefore, the seismic response of the structure is highly dependent on structural wall modeling.

In CSI Perform 3D, distributed plasticity can be applied with two options, as auto size and fixed size. In the auto size option, users are able to define fiber faster and automatically, but only one concrete material can be assigned to a cross section in this option so that there is not a difference of boundary and web regions. Therefore, to be able to use different concrete materials at different wall regions, fixed size fiber modeling option is used. Cracked flexural rigidity is calculated by the program automatically in fiber models.

Strain limits for concrete and reinforcements are defined based on TEC 2018. Strain gage elements are placed at structural wall ends to measure strains and evaluate acceptance criteria.

5.1.6.2. Columns. Hysteretic behavior of columns is dependent on axial load that cross sections carry. Hence, PMM hinges are used to capture nonlinear response of columns.

PMM hinges show biaxial bending under axial loads. Sectional analysis is performed to define the PMM yield surface at the beginning of nonlinear deformation. Plastic rotation capacities are defined using Equation 5.19 in TEC 2018.

$$\theta_p^{(CP)} = \frac{2}{3}\left[\left(\phi_u - \phi_y\right) L_p \left(1 - 0.5\frac{L_p}{L_s}\right) + 4.5\phi_u d_b\right] \tag{5.19}$$

Columns are modeled in CSI Perform 3D as two PMM hinges placed at the end of rigid end zones and one elastic cross section is defined between the two PMM hinges (Figure 5.6). Elastic section effective flexural rigidity $(EI)_e$ is defined using Equations 5.20 and 5.21.

$$(EI)_e = \frac{M_y L_s}{\theta_y 3} \tag{5.20}$$

$$\theta_y = \frac{\phi_y L_s}{3} + 0.0015\eta\left(1 + 1.5\frac{h}{L_s}\right) + \frac{\phi_y d_b f_{ye}}{8\sqrt{f_{ce}}} \tag{5.21}$$

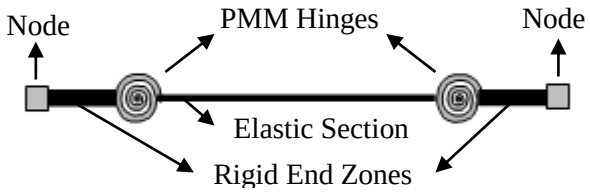

Figure 5.6. Columns modeling.

5.1.6.3. Coupling Beams. Coupling beams with diagonal reinforcement are modeled using plastic shear hinges. Effective rigidity of the section is found using Equation 5.20 and plastic rotation capacity of coupling beams is calculated by Equation 5.22.

$$\theta_p^{(CP)} = \frac{\varepsilon_c^{(CP)} L_p}{h\cos(\alpha_{cb})} \tag{5.22}$$

Coupling beams are modeled in CSI Perform 3D with using two elastic line elements and one shear hinge. Coupling beam modeling is shown in Figure 5.7.

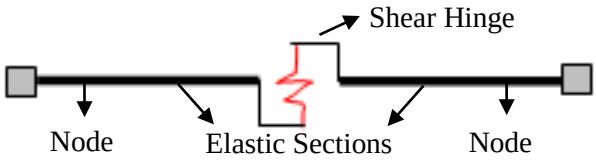

Figure 5.7. Modeling of coupling beams.

5.1.6.4. Elastic Slabs. Slabs are modeled elastically in one of the nonlinear models of structure to add rigidities of slab elements to total structural system rigidity. In that model, elastic slab (shell) elements are used with effective flexural rigidities defined according to Table 4.9.

5.1.6.5. Effective Slab-Beams. Most of the nonlinear analytical models are generated using effective slab-beams for the slab elements. Nonlinear modeling of effective slab-beams depend on the connection type (e.g. slab-column connection, slab-wall connection), connection class (e.g. weak or strong connection), and the type of the vertical element connected to (e.g. wall or column).

If the effective slab-beam is connected to a weak slab-column connection, modeling of effective the slab-beam consist of an elastic beam element that is linked to the column intersection node using the proposed an equivalent shear hinge model. Deformation capacity of model is taken from Table 2.2, based on the gravity shear ratio, as defined in ASCE 41-17. Strength (moment capacity) of equivalent shear hinge model is calculated using Equations 2.10, 2.11 and 2.12 (Figure 5.8).

If the effective slab-beam is connected to strong slab-column connection, a moment hinge (CS hinge) is assigned at the end of the elastic beam element. CS hinge's deformation capacity is defined from Table 2.2, considering the gravity shear ratio of

connection, and the CS hinge capacity is calculated using the moment capacity of the slab along the CS width (Figure 5.8).

In this study, bottom bars at weak and strong slab-column connections are used to resist bending moment and also as integrity reinforcement to exhibit more ductile behavior under earthquake loads and to avoid progressive collapse.

If effective slab-beam is connected to a slab-wall connection, a moment hinge (CS hinge) is assigned at the end of elastic beam element. Capacity of the hinge is defined with section analysis of the CS cross section. Plastic rotation capacity of such CS hinges is defined using Equation 5.23 (Figure 5.8).

$$\theta_p = \left(\phi_u - \phi_y\right) L_p \tag{5.23}$$

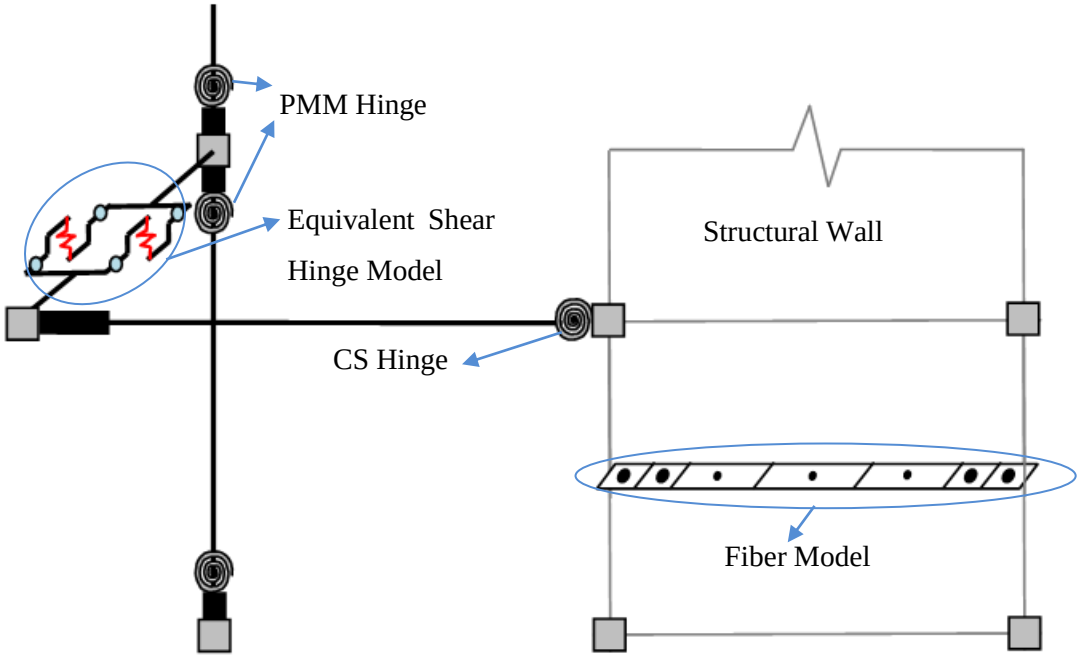

Figure 5.8. Modeling of effective slab-beam.

5.1.7. Damping

Hysteretic behavior of structural elements absorbs most of the seismic energy, when they undergo damage (plastic deformation). However, all energy dissipation sources are

not included in analytical model, such as internal friction and nonstructural elements. 2.5% viscous damping is therefore recommended for nonlinear analysis of high-rise buildings by TEC 2018, to consider non-hysteretic energy dissipation. In the Perform 3D model, 2.5% damping is assigned as a total of 2.4% modal damping, and 0.1% Rayleigh damping, in order to dissipate very high modes in the response.

5.1.8. Nonlinear Models

Since construction of a structural system in CSI Perform 3D is cumbersome process, a linear elastic model is first generated in CSI ETABS to simplify the modeling process. Then, the CSI ETABS model is transferred to CSI Perform 3D program. In the nonlinear models, the foundation is not included similarly to the linear model. Fixed supports are assigned at the foundation model. Five nonlinear models are generated; one with rigid diaphragms (no slabs), one with elastic (shell) slab elements, and the last three with effective slab-beams to simulate the slabs, representing three different building configurations designed using the three different punching shear design approaches (ACI 318, ACI 318 with overstrength, TEC 2018) described in the previous chapter (Figure 5.9 and 5.10).

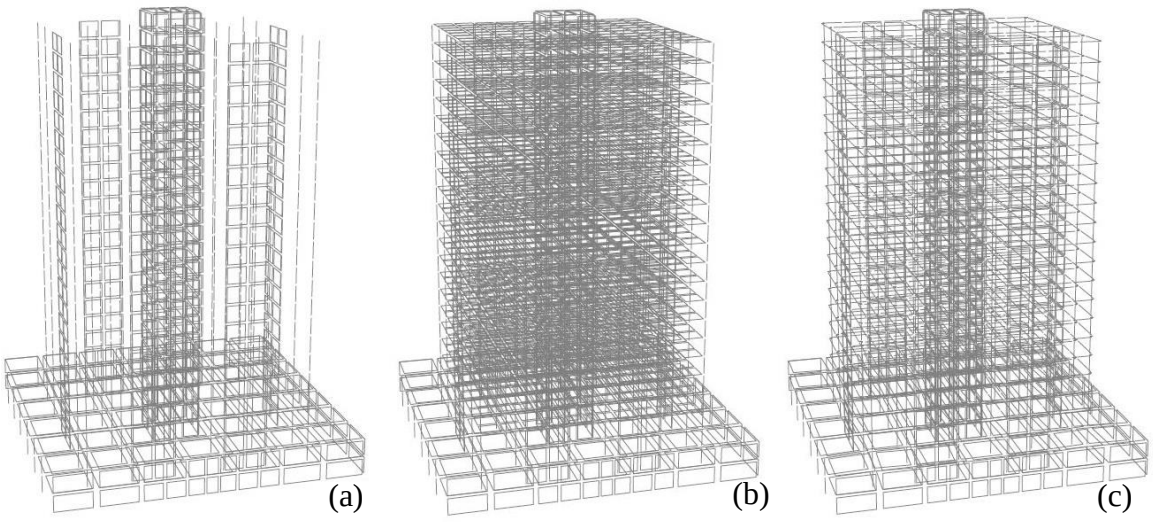

Figure 5.9. 3D views of models.

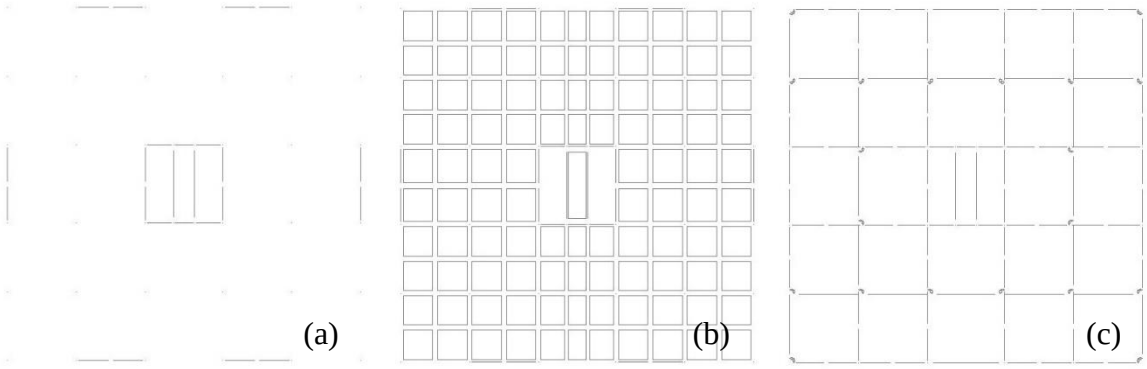

Figure 5.10. Plan views of models.

5.2. Analysis Method and Results

5.2.1. Nonlinear Response History Analysis Method

NLRHA is a method for evaluation of dynamic structural response under ground motion time histories. In NLRHA, the equation of motion is solved by numerical integration for each time step of ground motion, considering stiffness matrix changes. In this study, the five aforementioned nonlinear models are analyzed using the nonlinear response history method in CSI Perform3D software.

5.2.2. Nonlinear Response History Analysis Results

In this section, comparison of analysis results obtained from the five different models analyzed under the DD1 level ground motion records, using NLRHA, is presented. Story drift ratios, structural wall shear forces, compressive concrete strains and tensile reinforcing steel strains in the longitudinal direction of structural walls, coupling beam chord rotations, and slab-column connection plastic rotations are presented as critical response parameters for the rigid diaphragm (no slabs), elastic diaphragm (elastic slabs) and effective slab-beam models. Column plastic rotations obtained from all analyses are close to zero as expected. Plastic rotations are concentrated at the equivalent shear hinge elements at the slab-column connections. Therefore column plastic rotations are not presented in the analysis results.

Story drift ratios are checked at the geometric centroid and at one corner of the floor plan. (Figure 5.11) in both X and Y directions. Acceptance criteria for story drift ratios obtained from mean value of 22 pairs of ground motions are taken as 0.03 for collapse prevention (CP) and 0.02 for life safety (LS) performance levels. Mean values obtained from the 22 pairs of ground motions are presented in Figure 5.12 in both X and Y directions. The three effective slab-beam models undergo almost the same drift ratio as expected, since the models have almost the same structural stiffness, except one model has different cross-sectional dimensions for edge and corner columns (1300 mm versus 900 mm). Other than that, the only difference between the three effective-slab-beam models is slab reinforcement amount and configuration. Comparison of the so-called "noshell", "shell", and the three effective slab-beam models in terms of story drift ratios shows that the effective slab-beam models are stiffer than both the noshell model (as expected) and the shell model. Therefore, in the model with elastic shell elements for the slabs (shell model), using an effective flexural stiffness modifier of 0.25 is appears to be a feasible solution in checking of story drift ratios. This is partially because CSI Perform 3D analysis software cannot transfer bending moments from the slabs to the structural walls in the strong direction of the walls. Overall, all five models satisfy the CP performance level in terms of story drift ratios.

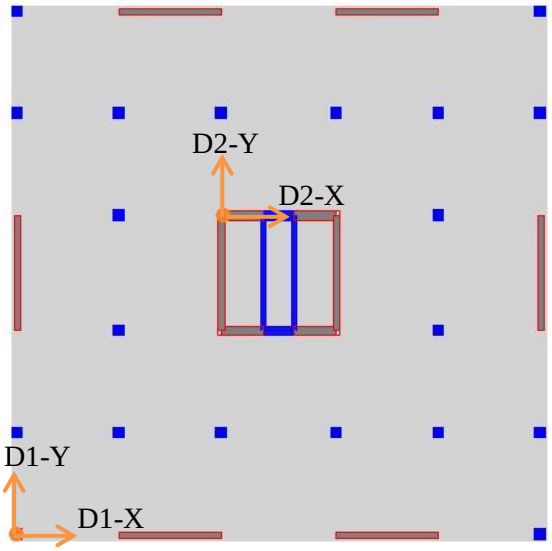

Figure 5.11. Control points of story drift ratios.

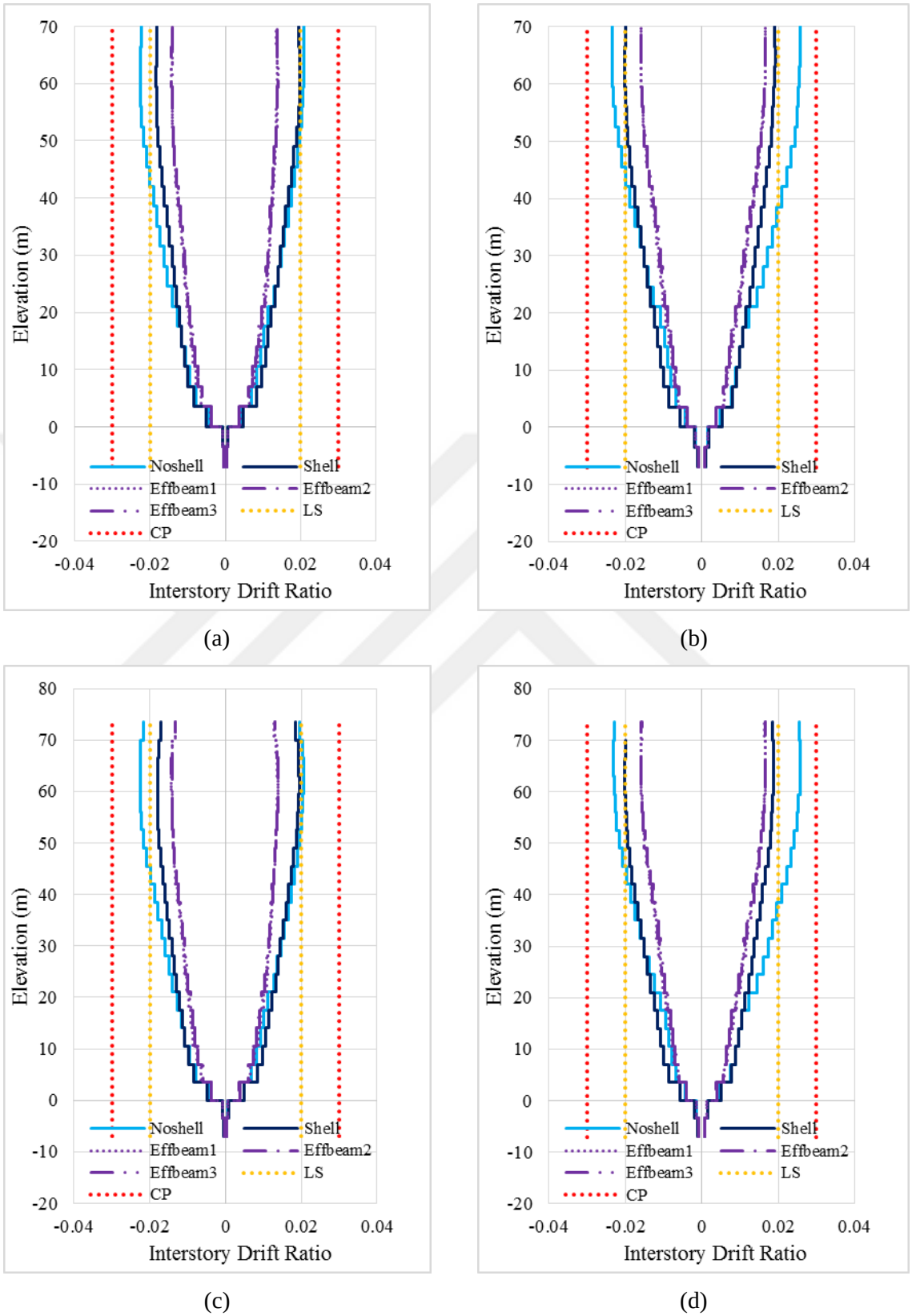

Figure 5.12. Interstory drift ratios for all models (a) D1-X, (b) D1-Y, (c) D2-X, (d) D2-Y.

Coupling beam plastic chord rotations and rotation demand-to-capacity ratios are presented in Figure 5.13 and Figure 5.14. In the figures, each point is the mean value of 22 pairs of earthquake ground motions for a coupling beam. CP and LS limits are defined as 0.05 rad and 0.0375 rad, coupling beams rotations are around 0.01 rad, which satisfies LS performance limits.

The model in which corner and edge slab column connections are designed considering overstrength coefficient *D* and $\gamma_f = 1$, is labeled as Effbeam 1, the other model in which corner and edge slab column connections are designed neglecting overstrength and taking $\gamma_f = 1$ is (ACI 318 design) is labeled as Effbeam 2, and the third model where corner and edge slab column connections are designed considering overstrength coefficient *D* and taking $\gamma_f = 0.6$ (TEC 2018 design) is labeled as Effbeam 3.

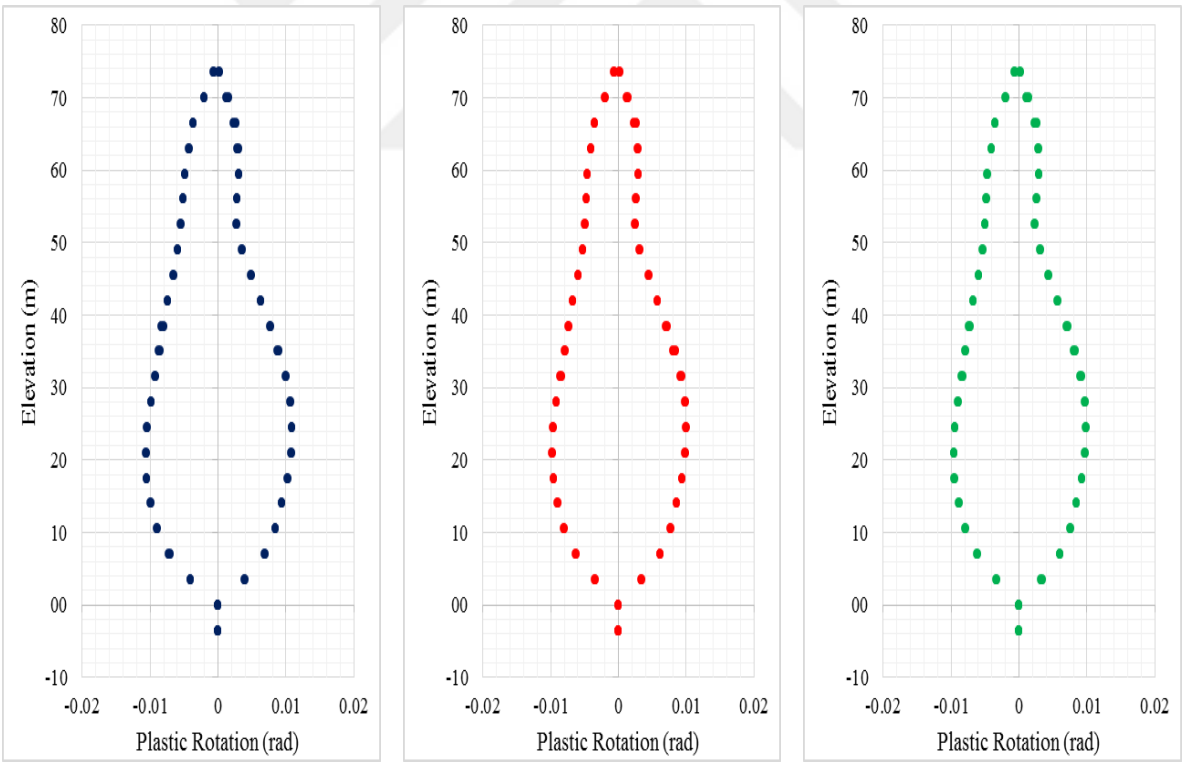

(a) (b) (c)

Figure 5.13. Plastic rotations of coupling beam (a) Effbeam1, (b) Effbeam2, (c) Effbeam3.

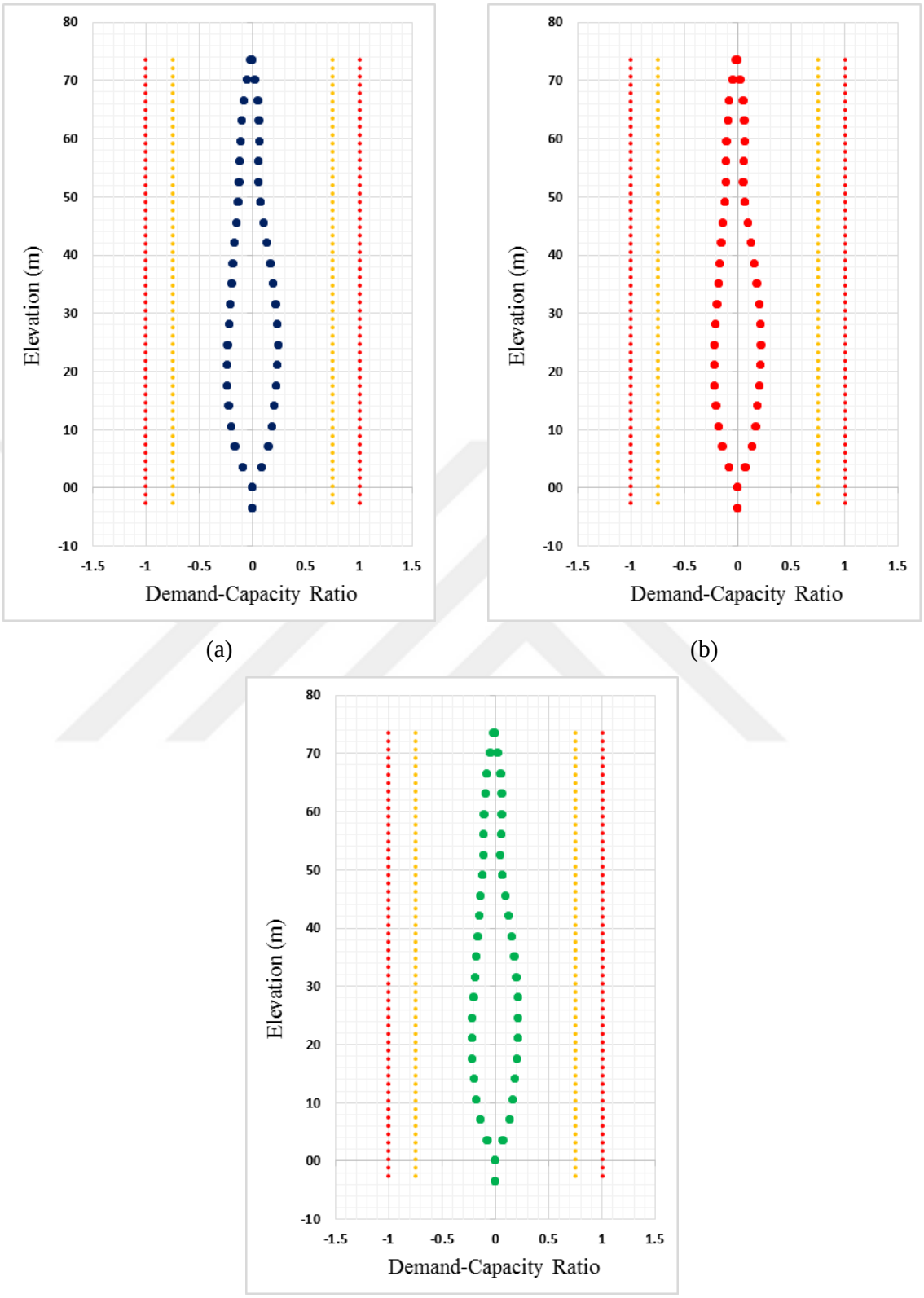

Figure 5.14. Demand-capacity ratios of coupling beam (a) Effbeam1, (b) Effbeam2, (c) Effbeam3.

To avoid brittle shear failure of structural walls under earthquake actions, the shear capacity of walls should be adequate to resists the wall shear forces obtained from NLRHA of the structure. Mean wall shear forces for the five models under 22 pairs of ground motions are compared with the maximum permitted wall shear capacity of $0.85\sqrt{f_{ce}}$ defined in TEC 2018. Structural wall names and locations are presented in Figure 5.15. The structural walls names that are typed in red are selected for presenting the shear forces shown in Figure 5.16.

Analysis results show that in all models, the structural walls on the exterior axis of the building have adequate maximum shear capacity; however, for the core walls, wall thickness can be slightly increased to provide adequate shear capacity, as observed from Figure 5.16.

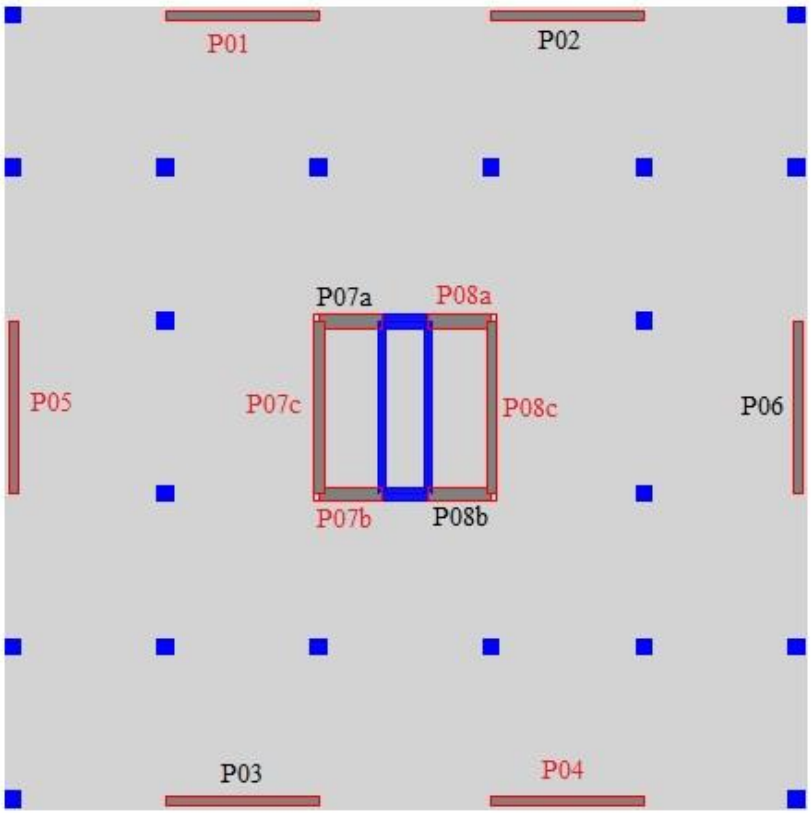

Figure 5.15. Structural wall names and locations.

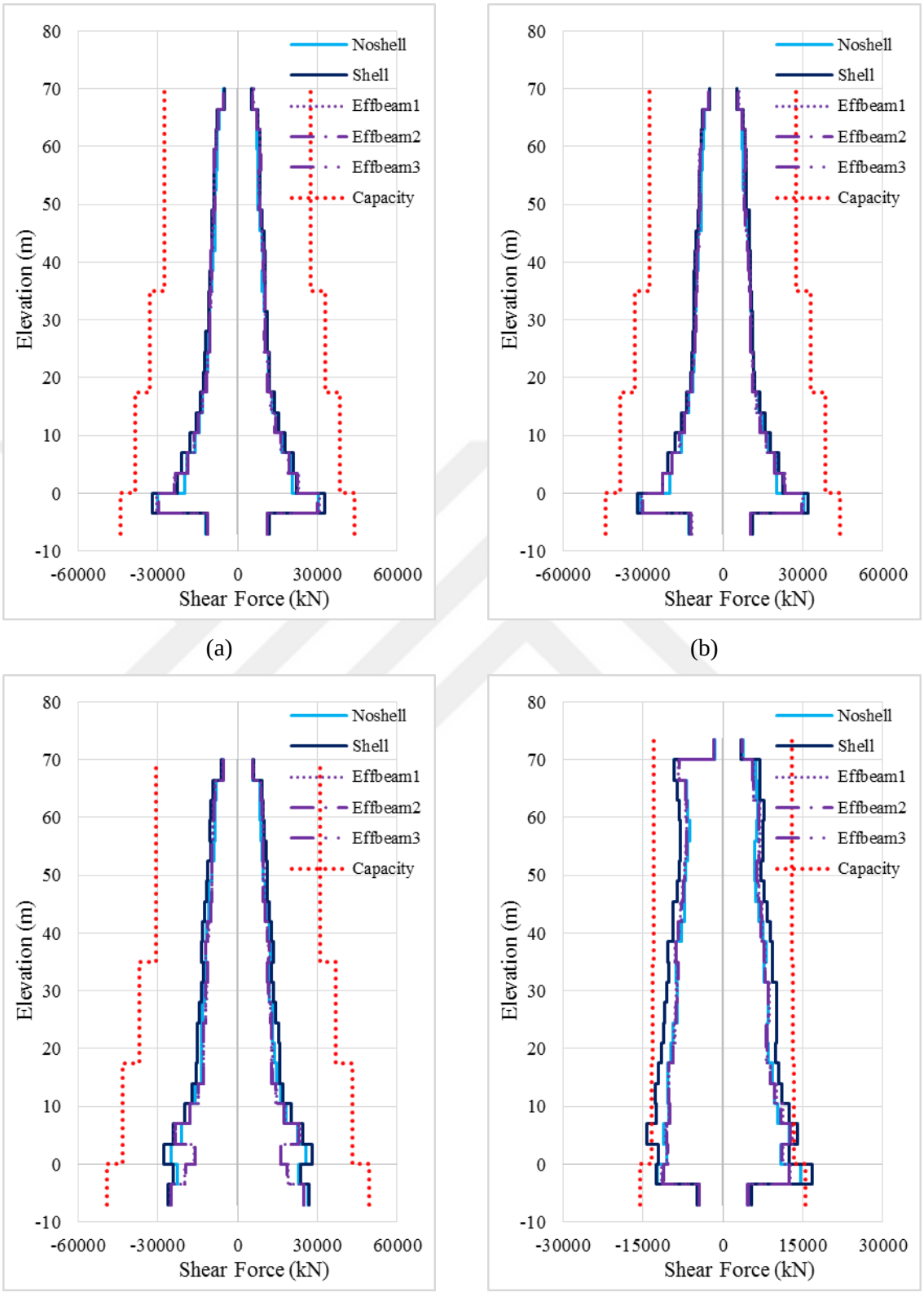

Figure 5.16. Structural wall shear forces at (a) P01, (b) P04, (c) P05, (d) P07b, (e) P07c, (f) P08a, (g) P08c.

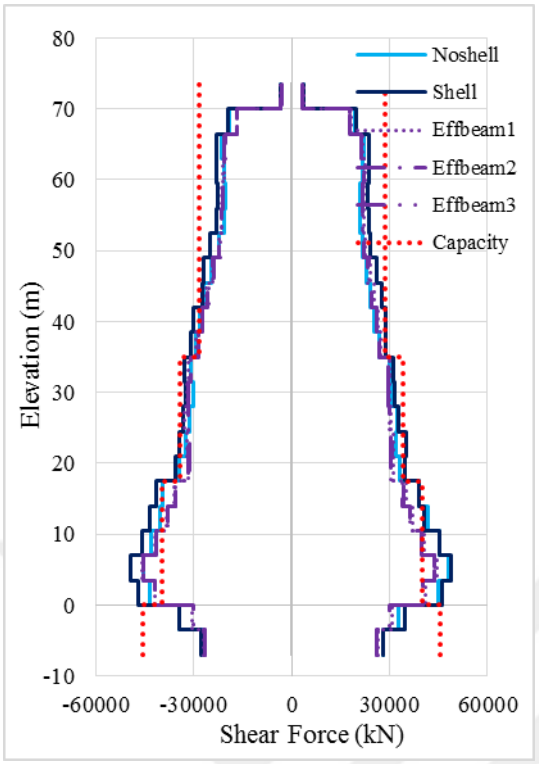

(e)

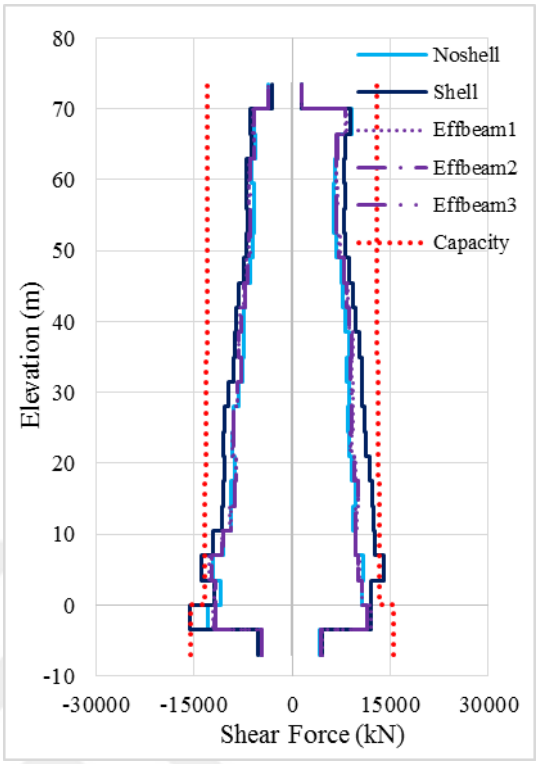

(f)

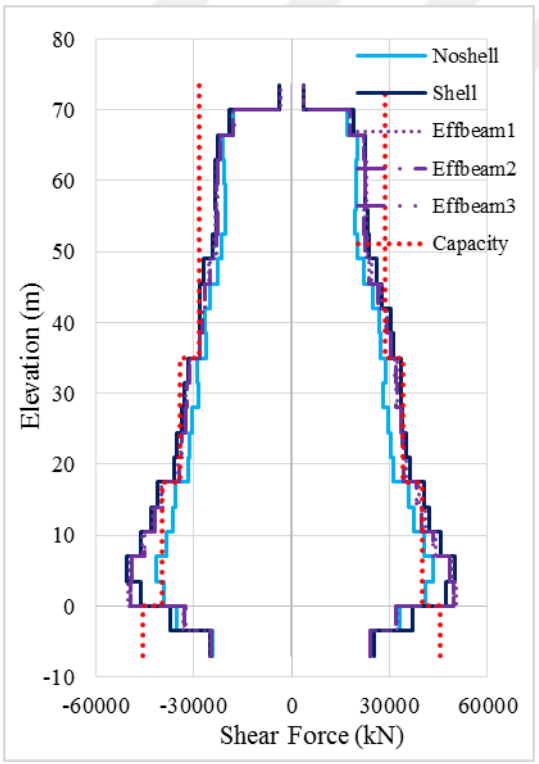

(g)

Figure 5.16. Structural wall shear forces at (a) P01, (b) P04, (c) P05, (d) P07b, (e) P07c, (f) P08a, (g) P08c (cont.).

Wall end longitudinal strains are checked to evaluate the performance of the structural walls. The strain measurement locations on building plan are shown in Figure 5.17. Performance limits for wall longitudinal strains are defined according to TEC 2018, as listed in Table 5.6. Average strain values from the 22 pairs of ground motions for the 5 models are compared to the immediate occupancy (IO) performance level strain limit in Figure 5.18. LS and CP performance limits are not included in Figure 5.18, since the strains are closer to the IO performance limit. The three effective beam models satisfy the IO performance criteria, whereas the "noshell" and "shell" models satisfy the LS performance level, in terms longitudinal strains on structural walls.

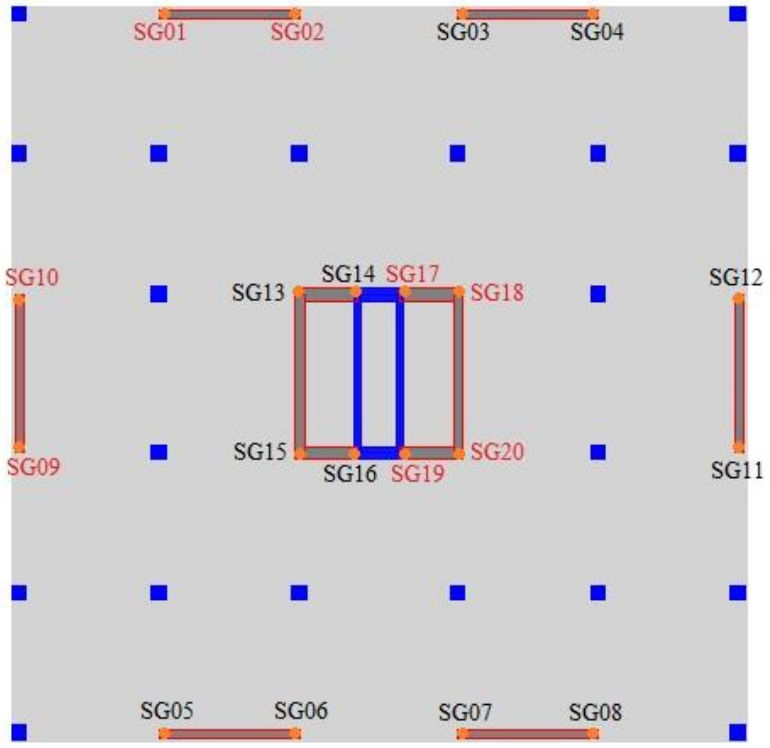

Figure 5.17. Strain measurement locations on floor plan.

Table 5.6. Performance limits for tension and compression strains on walls.

Performance Criteria	Compression	Tension
IO	-0.0025	0.0075
LS	-0.0135	0.0240
CP	-0.0180	0.0320

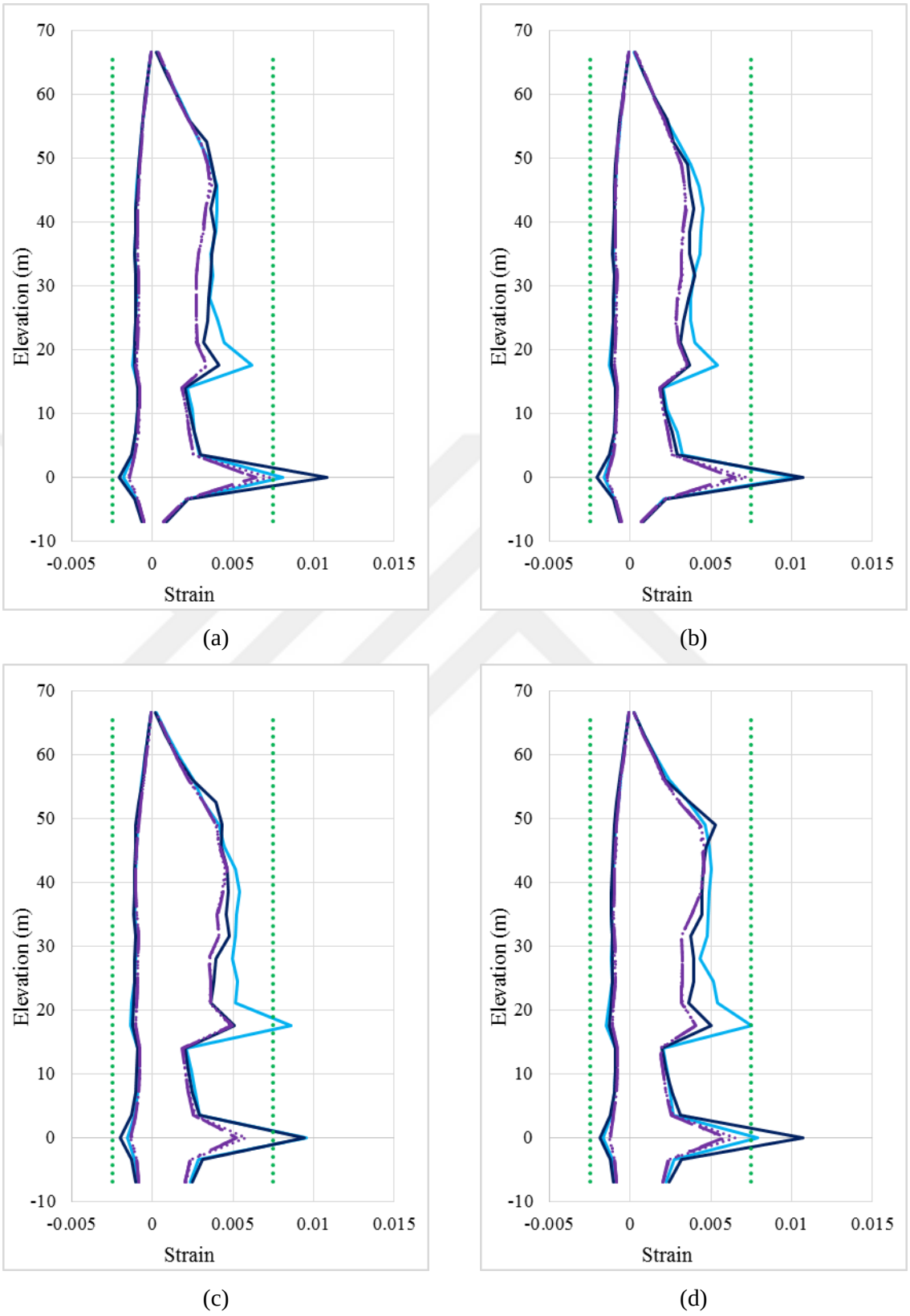

Figure 5.18. Structural wall strains (a) SG01, (b) SG02, (c) SG09, (d) SG10, (e) SG17, (f) SG18, (g) SG19, (h) SG20.

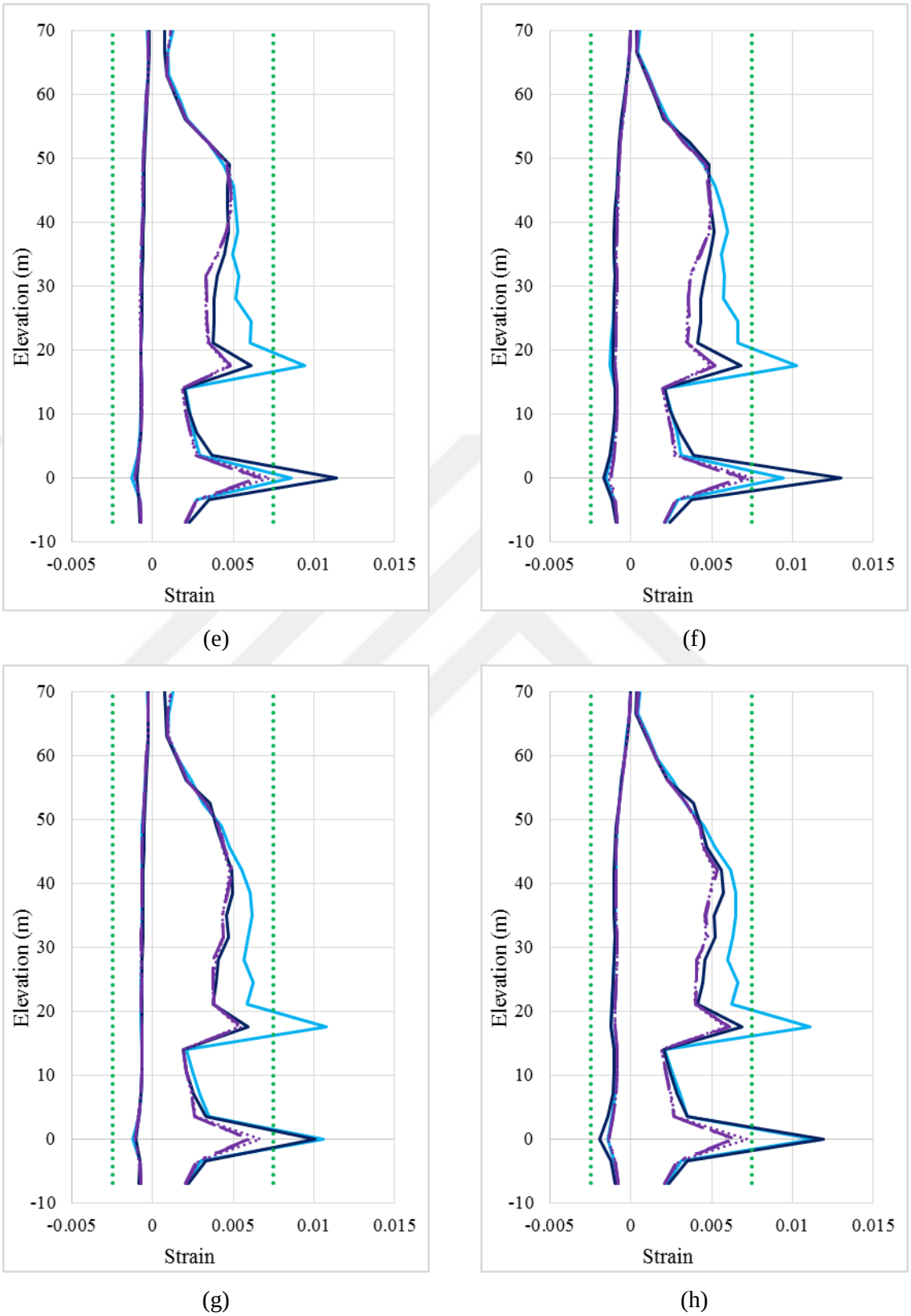

Figure 5.18. Structural wall strains (a) SG01, (b) SG02, (c) SG09, (d) SG10, (e) SG17, (f) SG18, (g) SG19, (h) SG20 (cont.).

Effective slab-beam element plastic hinge names and locations on the floor plan of the building are shown in Figure 5.19 at the slab-column and slab-wall connections. Plastic rotation limits for the slab-column hinges at the weak connections (equivalent shear hinges shown in orange) and the column strip hinges at the strong connections (moment hinges shown in red) are taken from Table 2.2, whereas the plastic rotation limits for the column strip hinges at the slab-wall connections (moment hinges shown in blue) are calculated using Equation 5.23, as described previously.

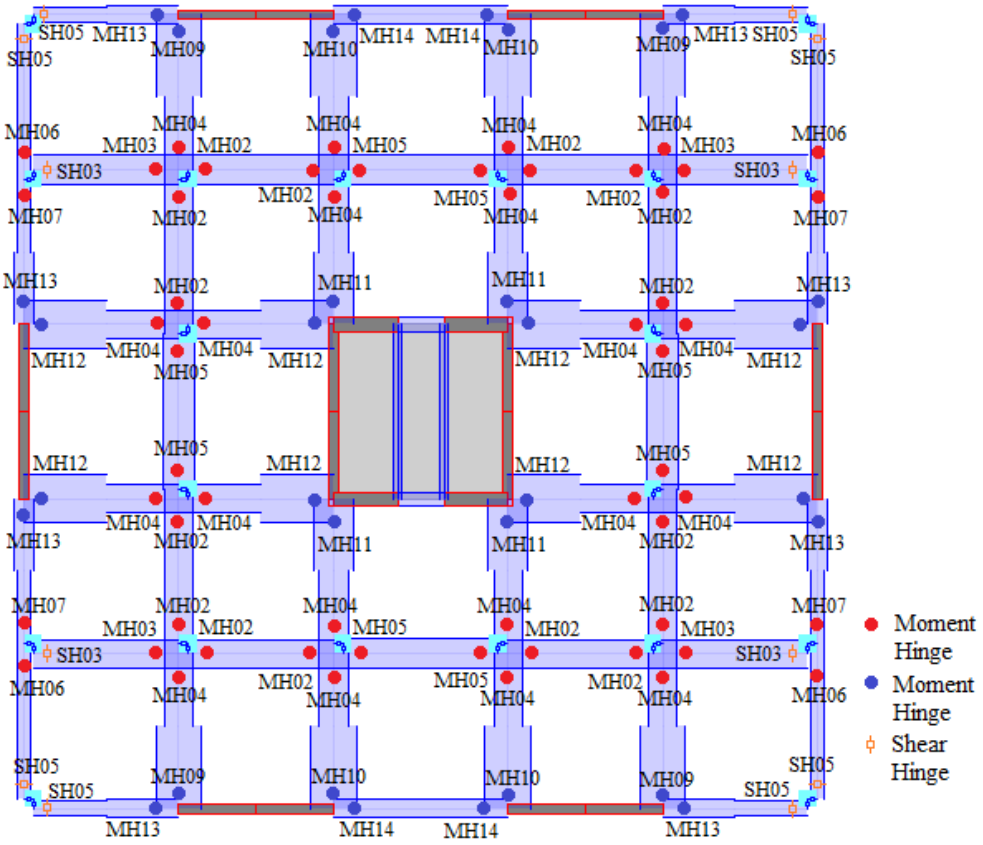

Figure 5.19. Hinge name and locations at slab-column and slab-wall connections.

NLRHA results for the effective beam model 1 ($\gamma_f = 1$ at edge and corner joints and *D* is considered in design) indicate that column strip hinges at interior (strong) slab-column connections located on slab beams that are connected to another column at the other end (e.g., MH02), rotate by a maximum of around 0.01 rad. However, if the slab beam is connected to a wall at the other end, the column strip hinge at the slab-column connection (e.g., MH04) can rotate by up to 0.04 rad. Similar results are obtained for edge columns in

parallel direction to the edge. Column strip hinges on slab beams connected to another column (e.g., MH06) rotate by less than 0.01 rad, whereas those on slab beams connected to walls at the other end (e.g., MH07) rotate as much as 0.026 rad, as shown in Figure 5.20. All of these rotations are below or very close to CP performance limits.

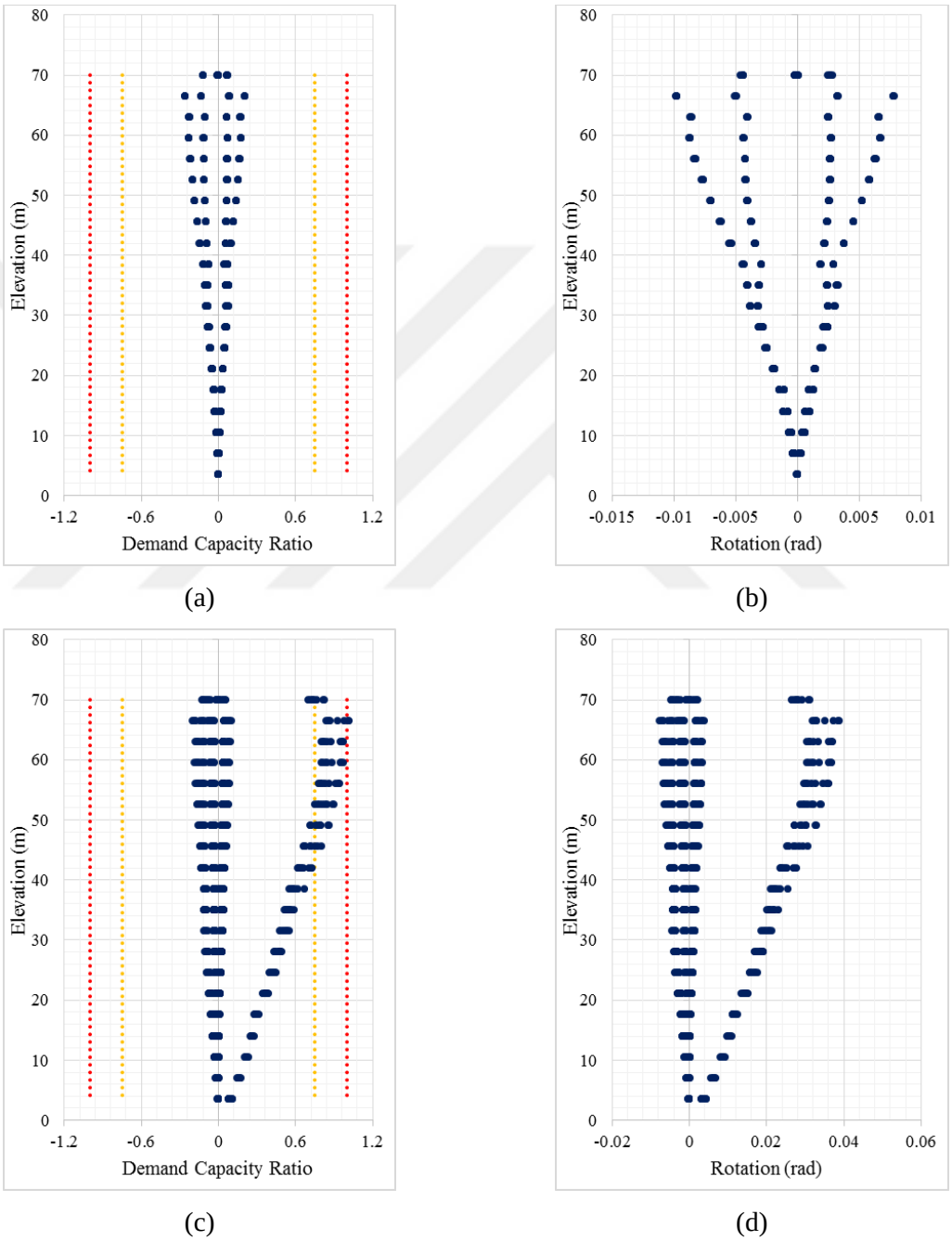

Figure 5.20. Rotations and demand/capacity ratios for effective beam model 1 (a) and (b) MH02, (c) and (d) MH04, (e) and (f) MH06, (g) and (h) MH07.

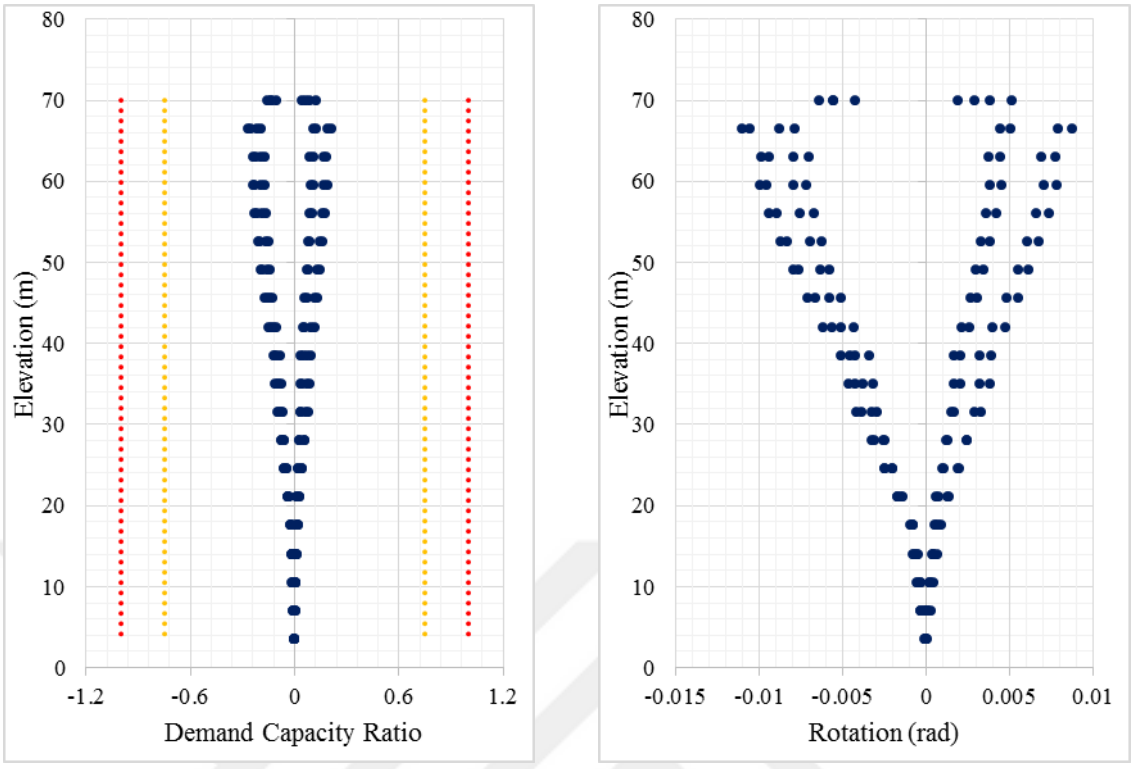

(e) (f)

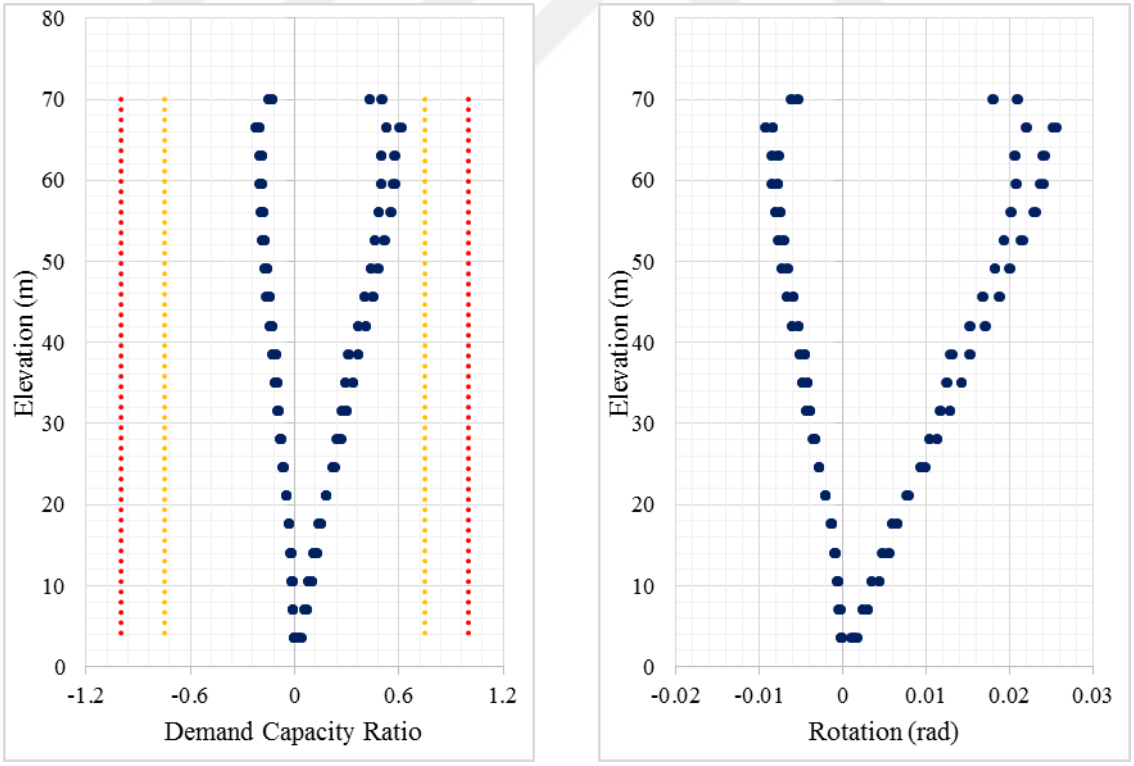

(g) (h)

Figure 5.20. Rotations and demand/capacity ratios for effective beam model 1 (a) and (b) MH02, (c) and (d) MH04, (e) and (f) MH06, (g) and (h) MH07 (cont.).

Overall, around 0.02 and 0.03 rad plastic rotations are obtained from column strip moment hinges at slab-wall connections (e.g., MH12 and MH13), which are well below CP performance limits (Figure 5.21).

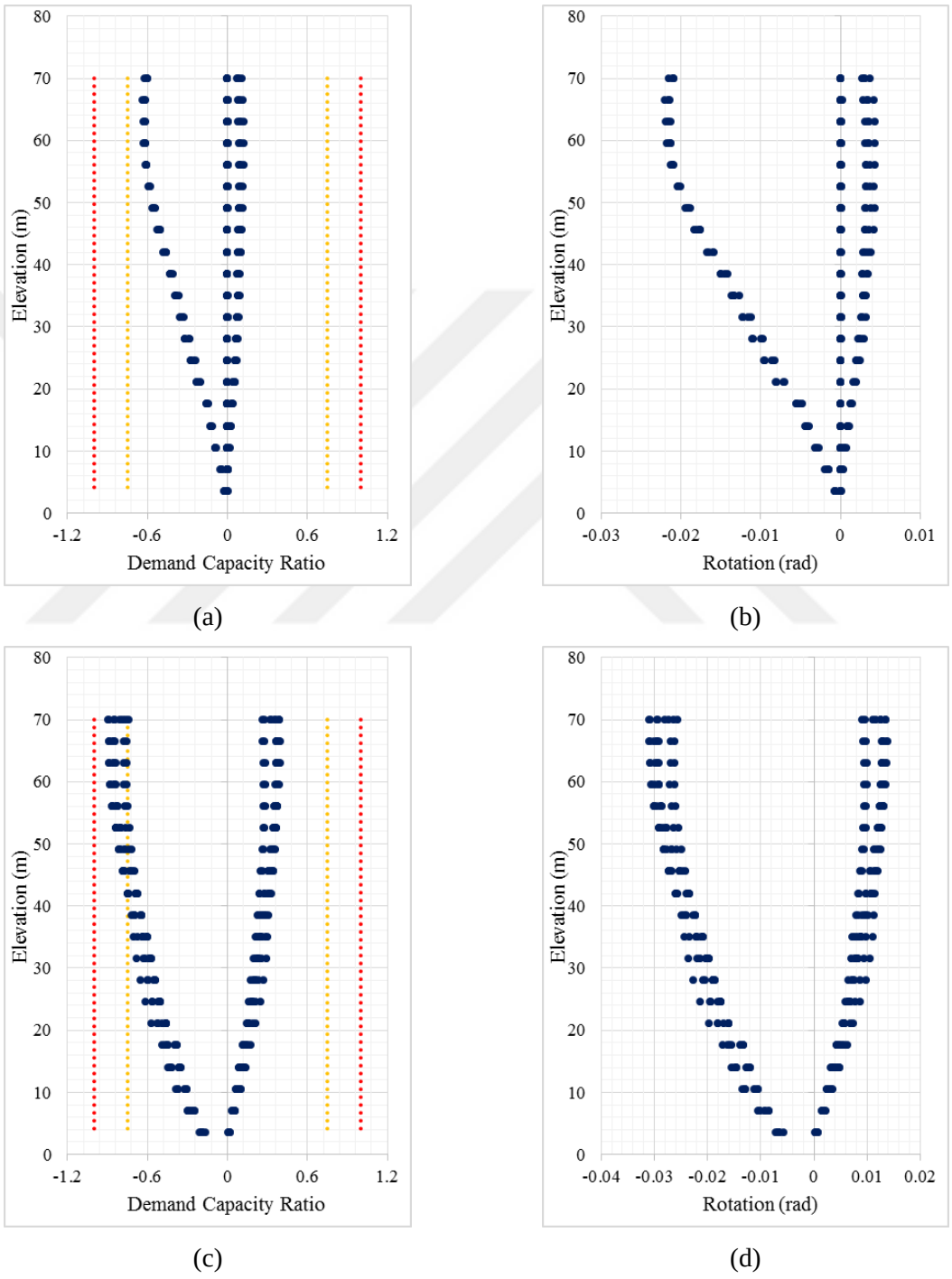

Figure 5.21. Rotations and demand/capacity ratios for effective beam model 1 (a) and (b) MH12, (c) and (d) MH13.

All edge and corner slab-column connections that were modeled using the proposed eccentric shear hinge model (SH03 and SH05) rotate by 0.01–0.015 rad, which satisfies the LS performance level in the effective beam model 1 configuration ($\gamma_f = 1$ at edge and corner joints and *D* is considered in design) (Figure 5.22).

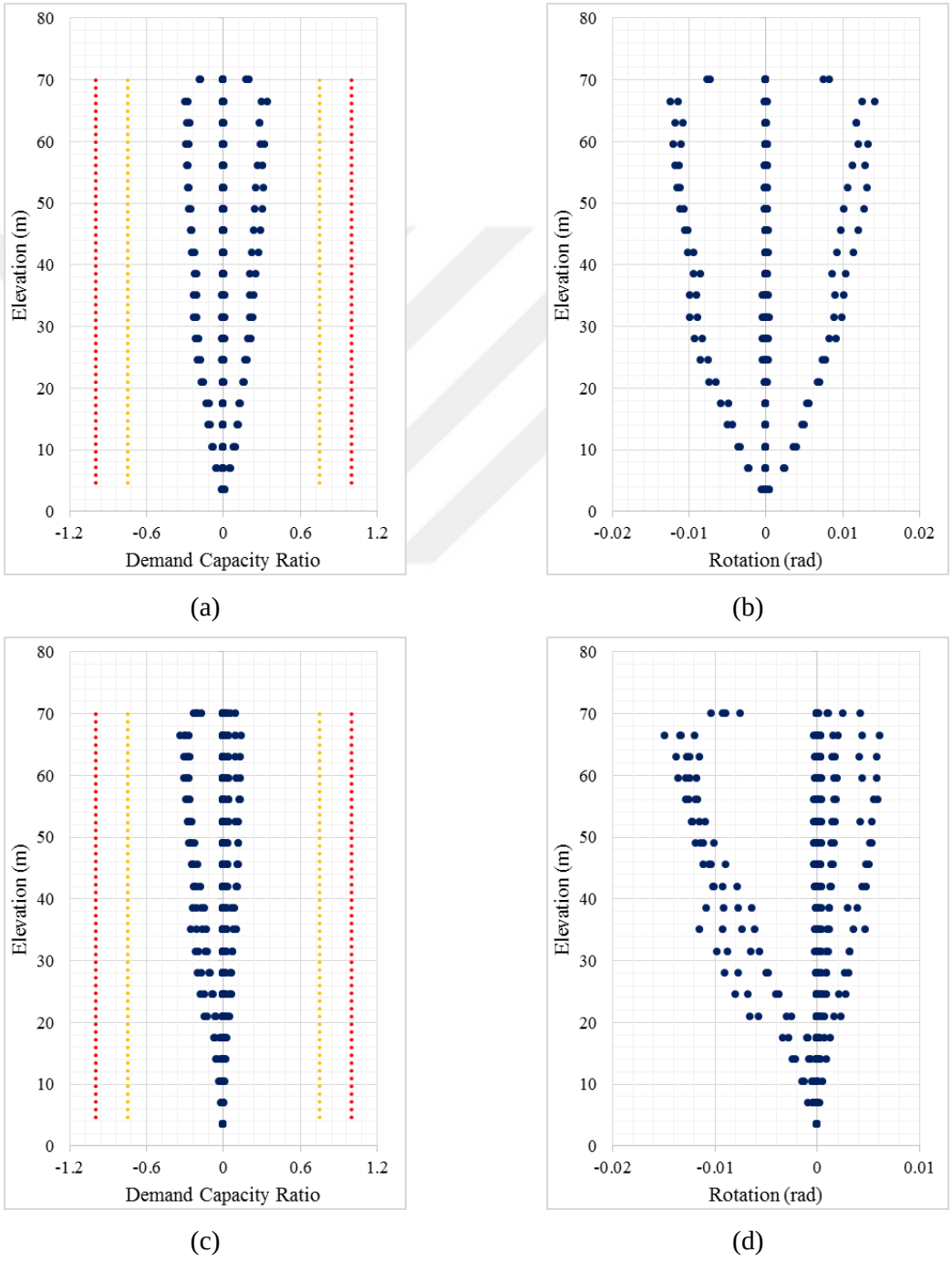

Figure 5.22. Rotations and demand/capacity ratios for effective beam model 1 (a) and (b) SH03, (c) and (d) SH05.

NLRHA results for the effective beam model 2 ($\gamma_f = 1$ at edge and corner joints and *D* is not considered in design – ACI 318 approach) indicate that column strip hinges at interior (strong) slab-column connections located on slab beams that are connected to another column at the other end (e.g., MH02), rotate by a maximum of around 0.01 rad at that slab-column connection.

However, if the slab beam is connected to a wall at the other end, the column strip hinge at the slab-column connection (e.g., MH04) can rotate by up to 0.04 rad. Similar results are obtained for edge columns in parallel direction to the edge. Column strip hinges on slab beams connected to another column (e.g., MH06) rotate by 0.022 rad at most, whereas those on slab beams connected to walls at the other end (e.g., MH07) rotate as much as 0.028 rad, as shown in Figure 5.23. All of these rotations are below or very close to CP performance limits.

In this case, plastic rotations of column strip moment hinges at slab-wall connections (e.g., MH12 and MH13), are significantly larger that those obtained for the previous case (effective beam model 1), since a lower amount of slab flexural reinforcement is used in this case at the slab wall connections The plastic rotations slightly exceed the CP performance limit in this case (Figure 5.24).

For all edge slab-column connections the maximum plastic rotation obtained in this case is 0.028 rad, which satisfies the LS performance criterion. However, at the corner slab-column connections, plastic rotations of around 0.05 rad are obtained, which are 20% above the limiting demand-to-capacity ratio of 1.0 (Figure 5.25).

Therefore, results obtained using the effective beam model 2 configuration ($\gamma_f = 1$ at edge and corner joints and *D* is not considered in design; ACI 318 approach) indicate that when designing slab-column connections, neglecting seismic overstrength in design of slab flexural reinforcement at the connection region (moment transfer width; $c+5h$) may occasionally not satisfy the targeted performance criteria.

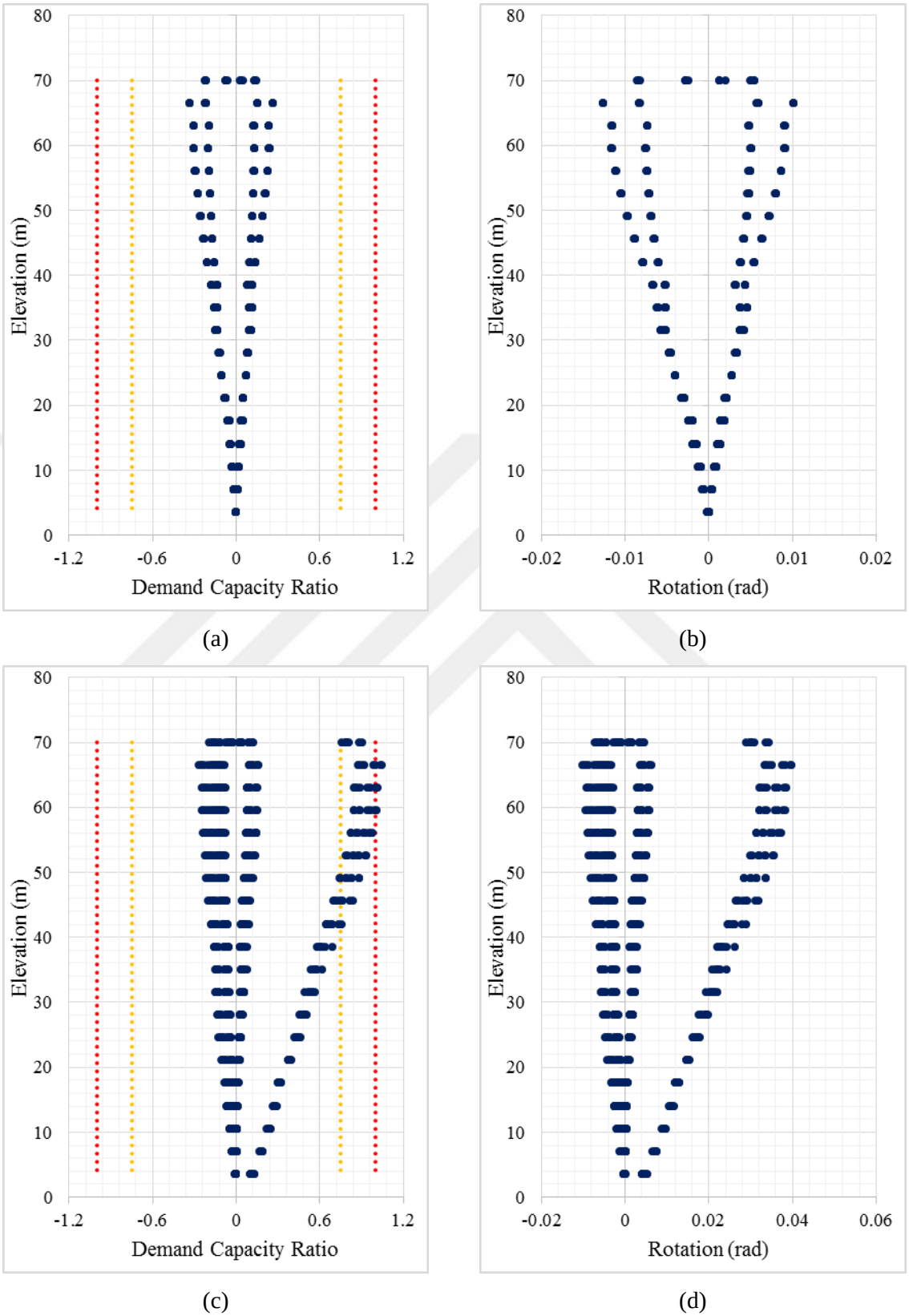

Figure 5.23. Rotations and demand/capacity ratios for effective beam model 2 (a) and (b) MH02, (c) and (d) MH04, (e) and (f) MH06, (g) and (h) MH07.

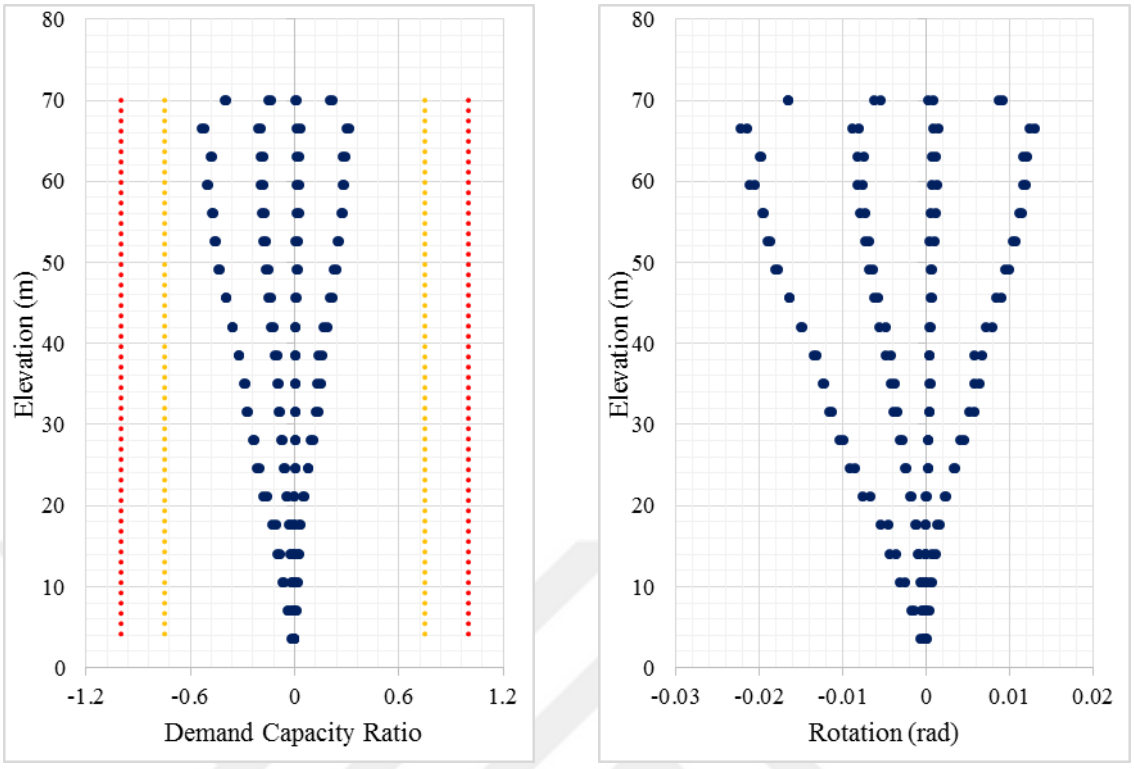

(e) (f)

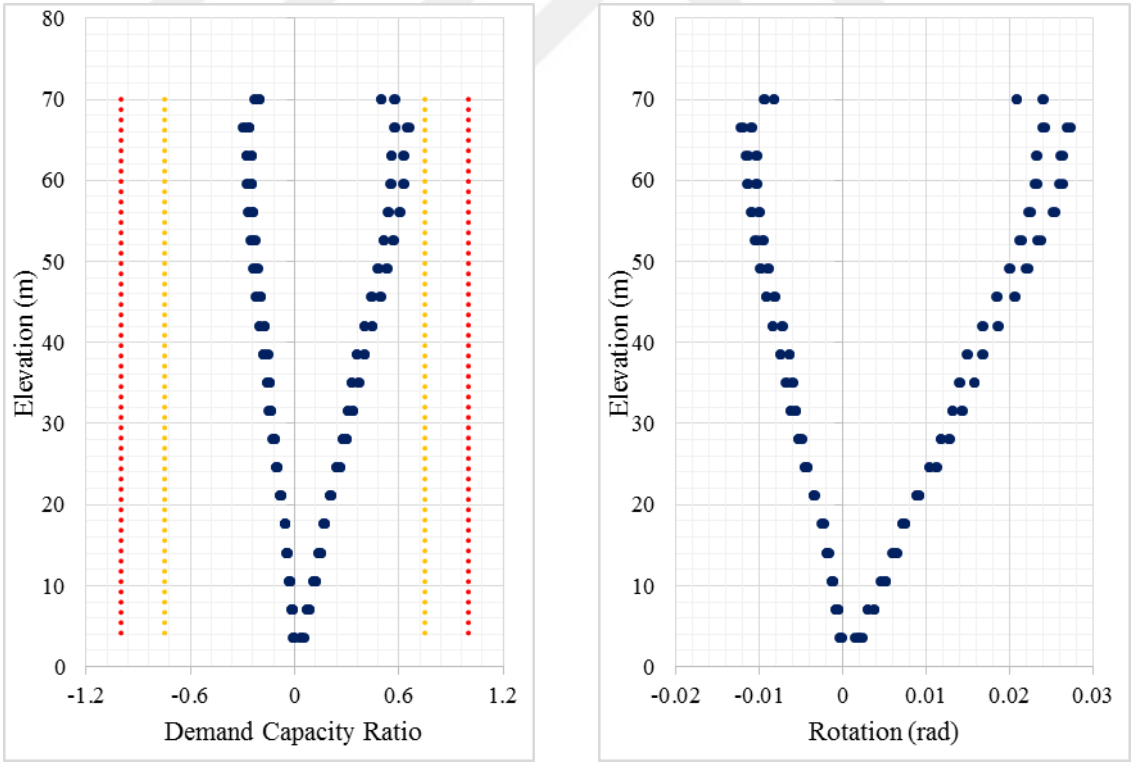

(g) (h)

Figure 5.23. Rotations and demand/capacity ratios for effective beam model 2 (a) and (b) MH02, (c) and (d) MH04, (e) and (f) MH06, (g) and (h) MH07 (cont.).

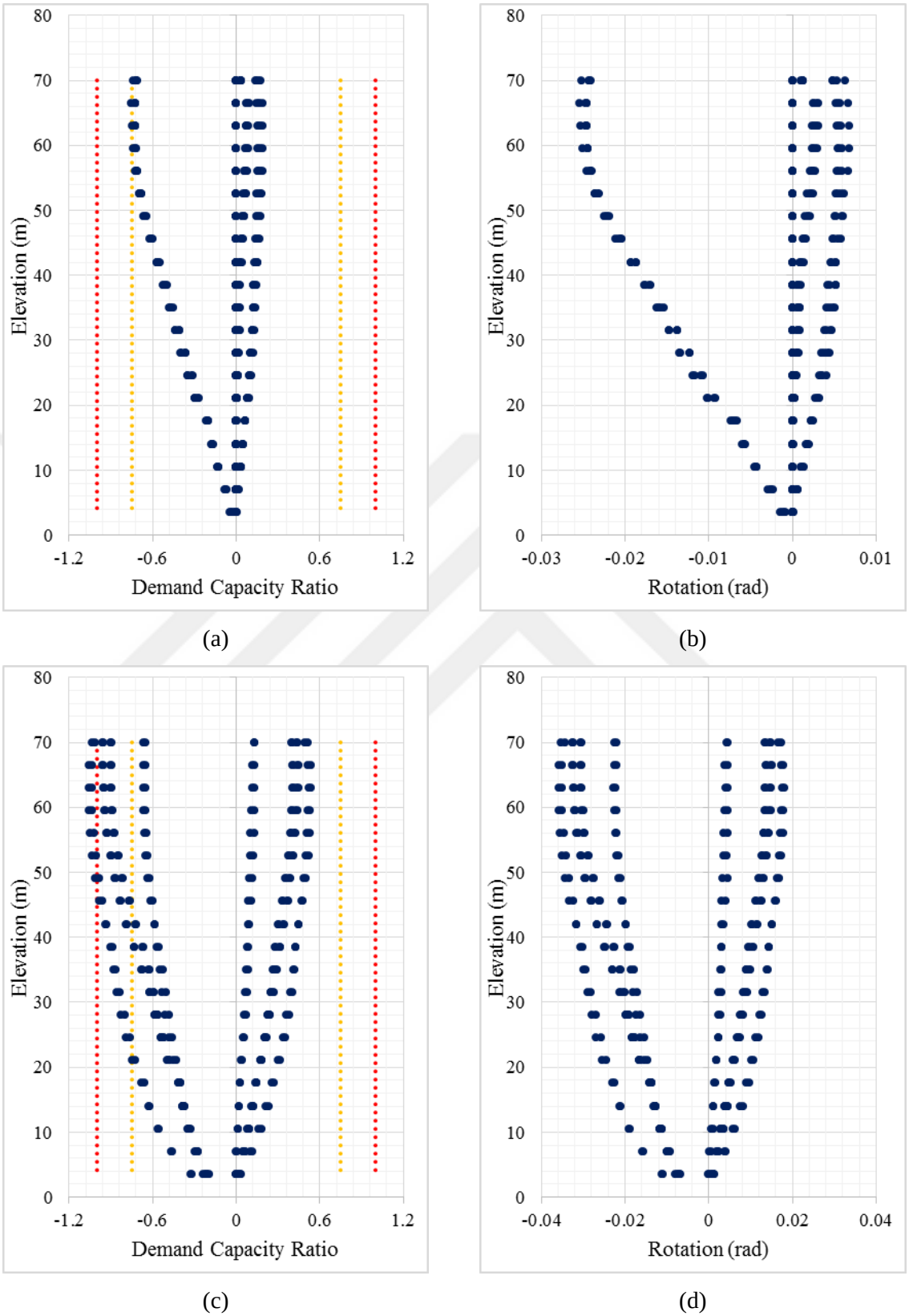

Figure 5.24. Rotations and demand/capacity ratios for effective beam model 2 (a) and (b) MH12, (c) and (d) MH13.

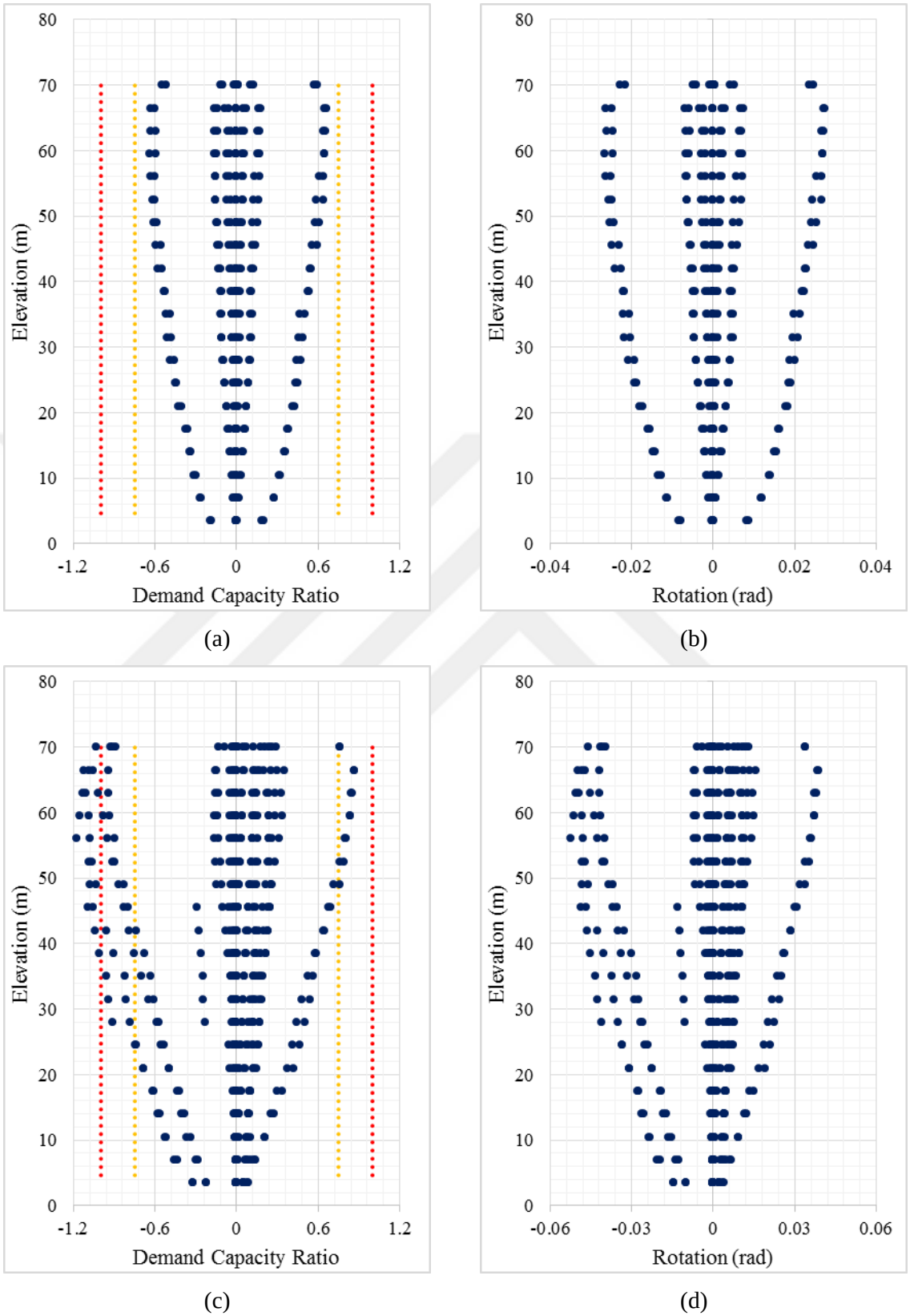

Figure 5.25. Rotations and demand/capacity ratios for effective beam model 2 (a) and (b) SH03, (c) and (d) SH05.

In the third model configuration (effective beam model 3, $\gamma_f = 0.6$ at edge and corner joints and *D* is considered in design – TEC 2018 approach), fixed 1300 mm x 1300 mm column cross sections have to be used for the edge and corner columns to comply with TEC 2018 provisions (versus 900 mm x 900 mm dimensions in the previous two cases). Therefore, all slab-column connections become strong connections, and column strip moment hinges are used also at the edge and corner joints, instead of the equivalent shear hinges used in the previous cases. The names and locations of the hinges for this case are illustrated in Figure 5.26.

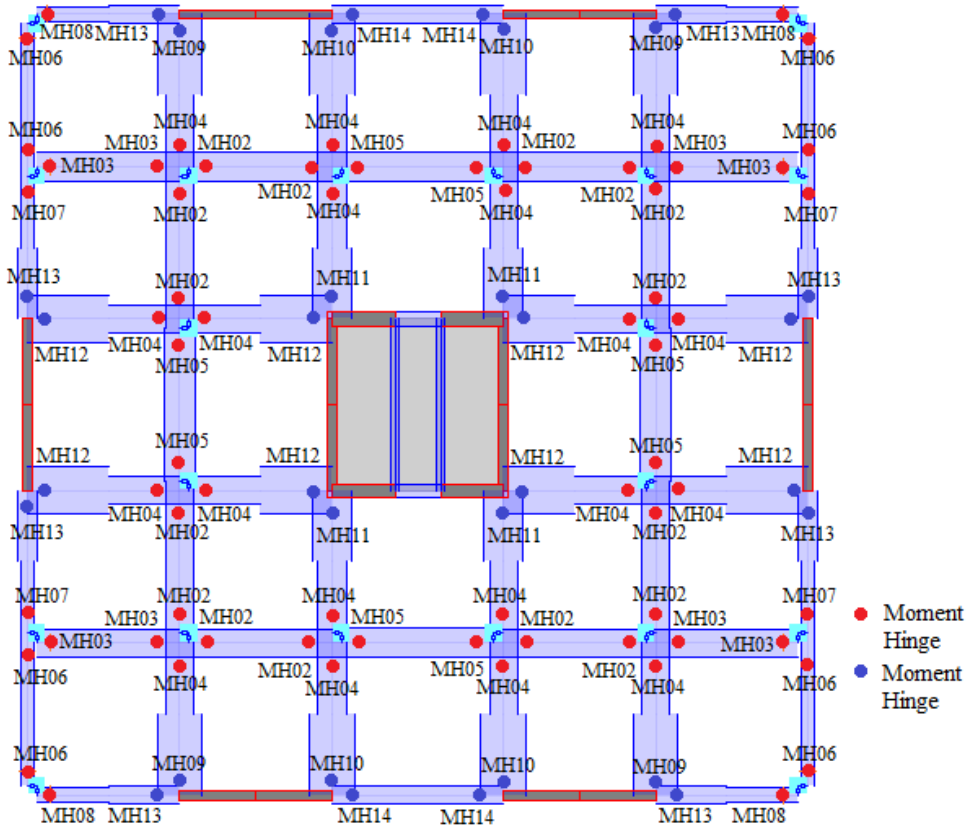

Figure 5.26. Hinge names and locations for slab-column and slab-wall connections.

NLRHA results for the effective beam model 3 ($\gamma_f = 0.6$ at edge and corner joints and *D* is considered in design) indicate that column strip hinges at interior slab-column connections located on slab beams that are connected to another column at the other end (e.g., MH02), rotate by a maximum of around 0.0125 rad. However, if the slab beam is connected to a wall at the other end, the column strip hinge at the slab-column connection

(e.g., MH04) can rotate by up to 0.04 rad. Similar results are obtained for edge columns in parallel direction to the edge. Column strip hinges on slab beams connected to walls at the other end (e.g., MH07) rotate as much as 0.03 rad, as shown in Figure 5.27. All of these rotations are below or very close to CP performance limits.

Plastic rotations at column strip moment hinges at slab – core wall connections (e.g., MH12) do not exceed 0.026 rad, which satisfies the performance LS performance limit, whereas in column strip moment hinges connected to edge rectangular walls in their strong directions (e.g., MH13), plastic rotations reach 0.032 rad, which does not exceed the CP performance limit (Figure 5.28).

Plastic rotations at column strip moment hinges at the edge and corner beam column connections (e.g., MH03, MH06, MH08) vary between 0.01 to 0.015 rad from the 10th story of the building to the top of the building, which falls below the LS performance limit (Figure 5.29).

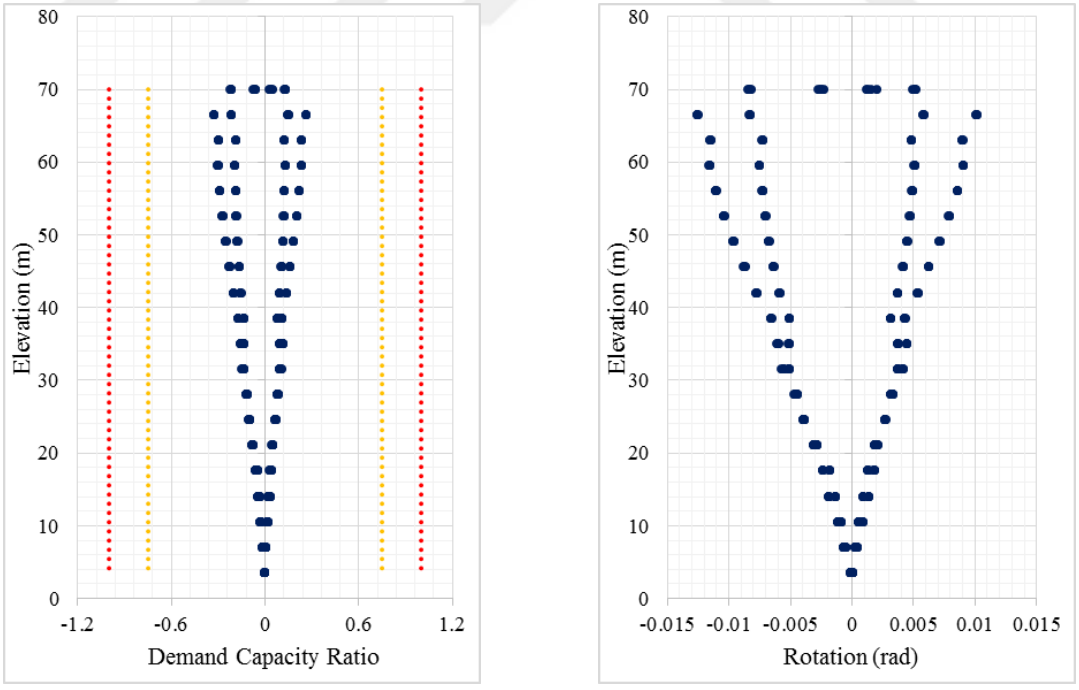

(a) (b)

Figure 5.27. Rotations and demand/capacity ratios for effective beam model 3 (a) and (b) MH02, (c) and (d) MH04, (e) and (f) MH07.

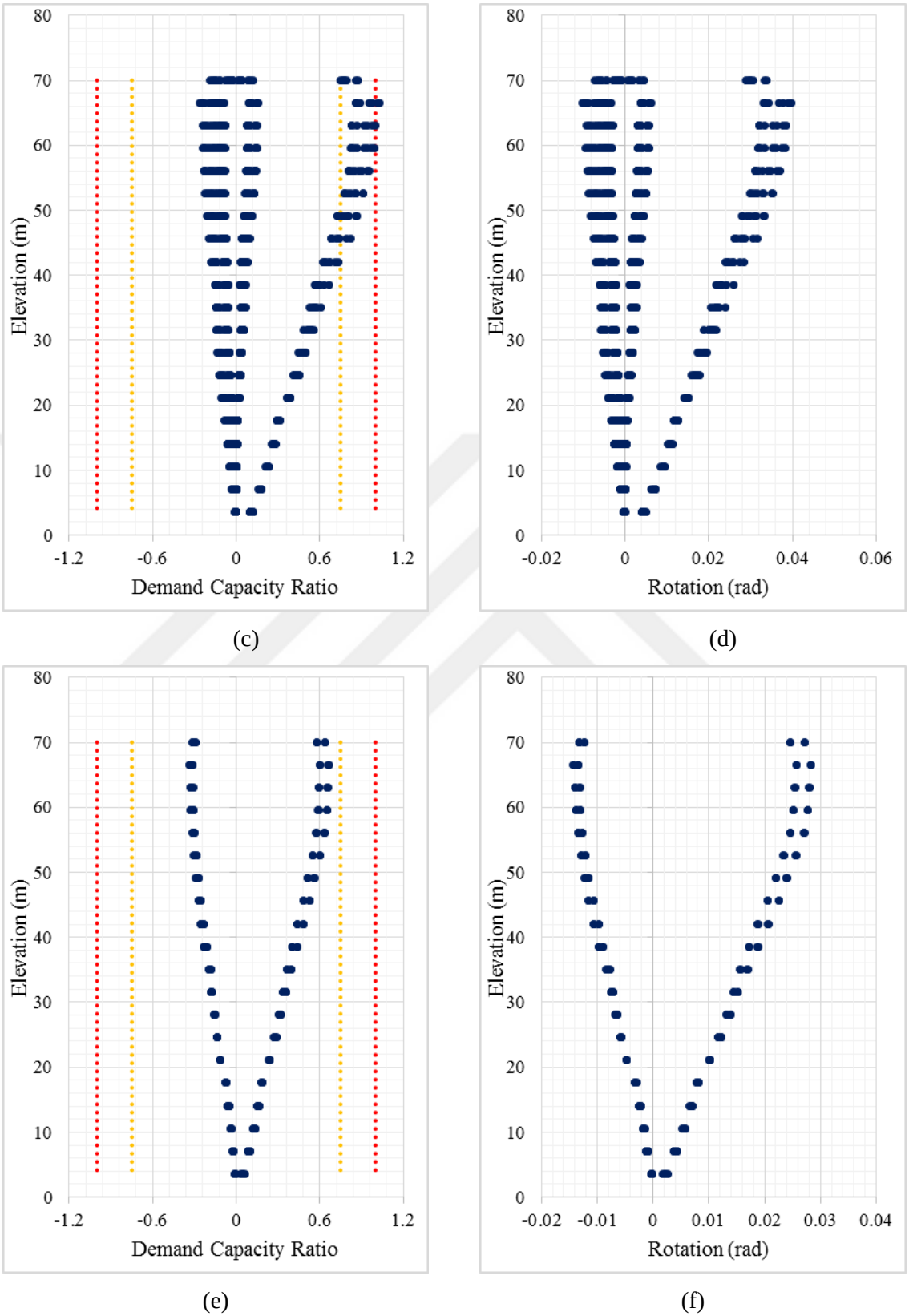

Figure 5.27. Rotations and demand/capacity ratios for effective beam model 3 (a) and (b) MH02, (c) and (d) MH04, (e) and (f) MH07 (cont.).

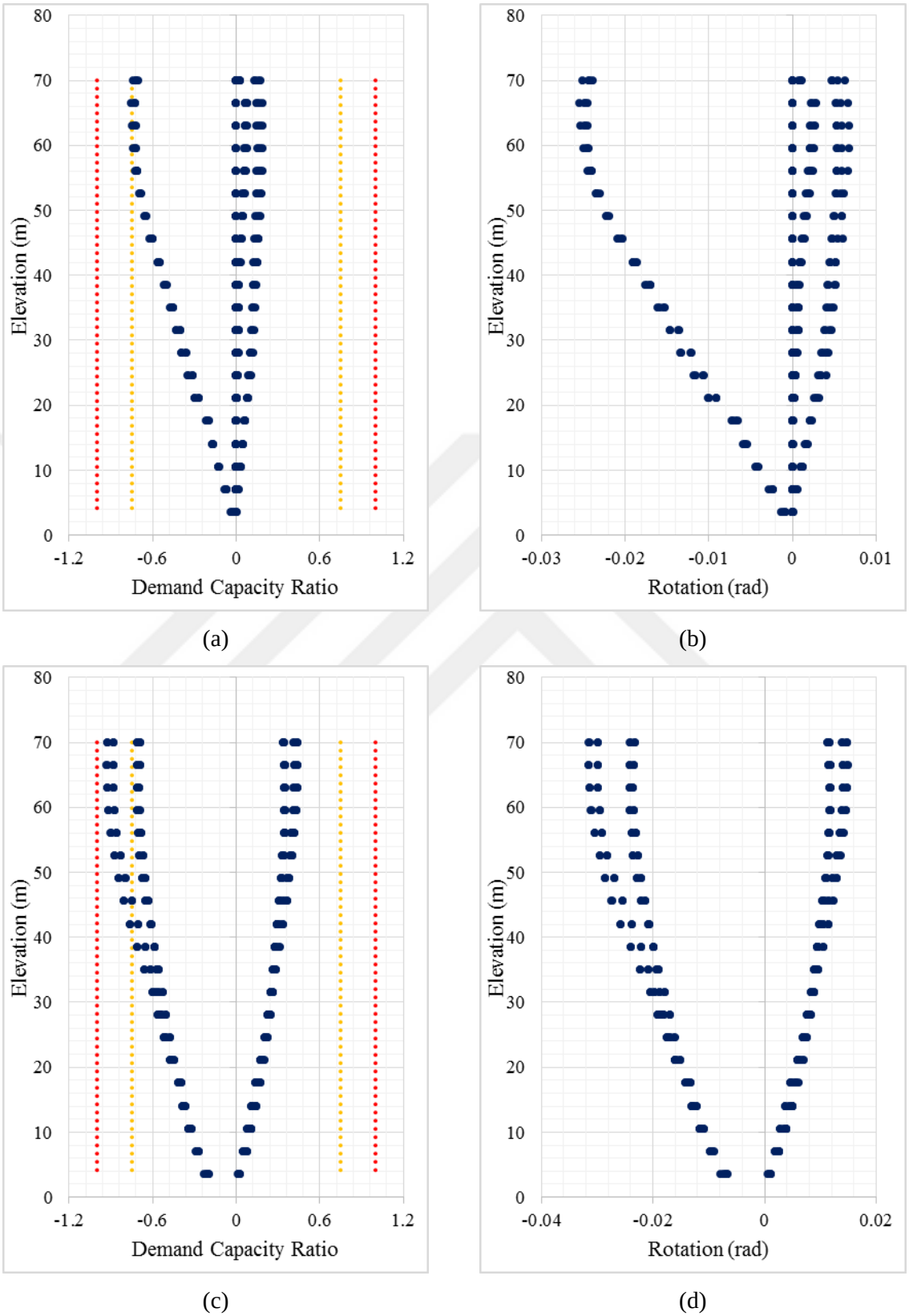

Figure 5.28. Rotations and demand/capacity ratios for effective beam model 3 (a) and (b) MH12, (c) and (d) MH13.

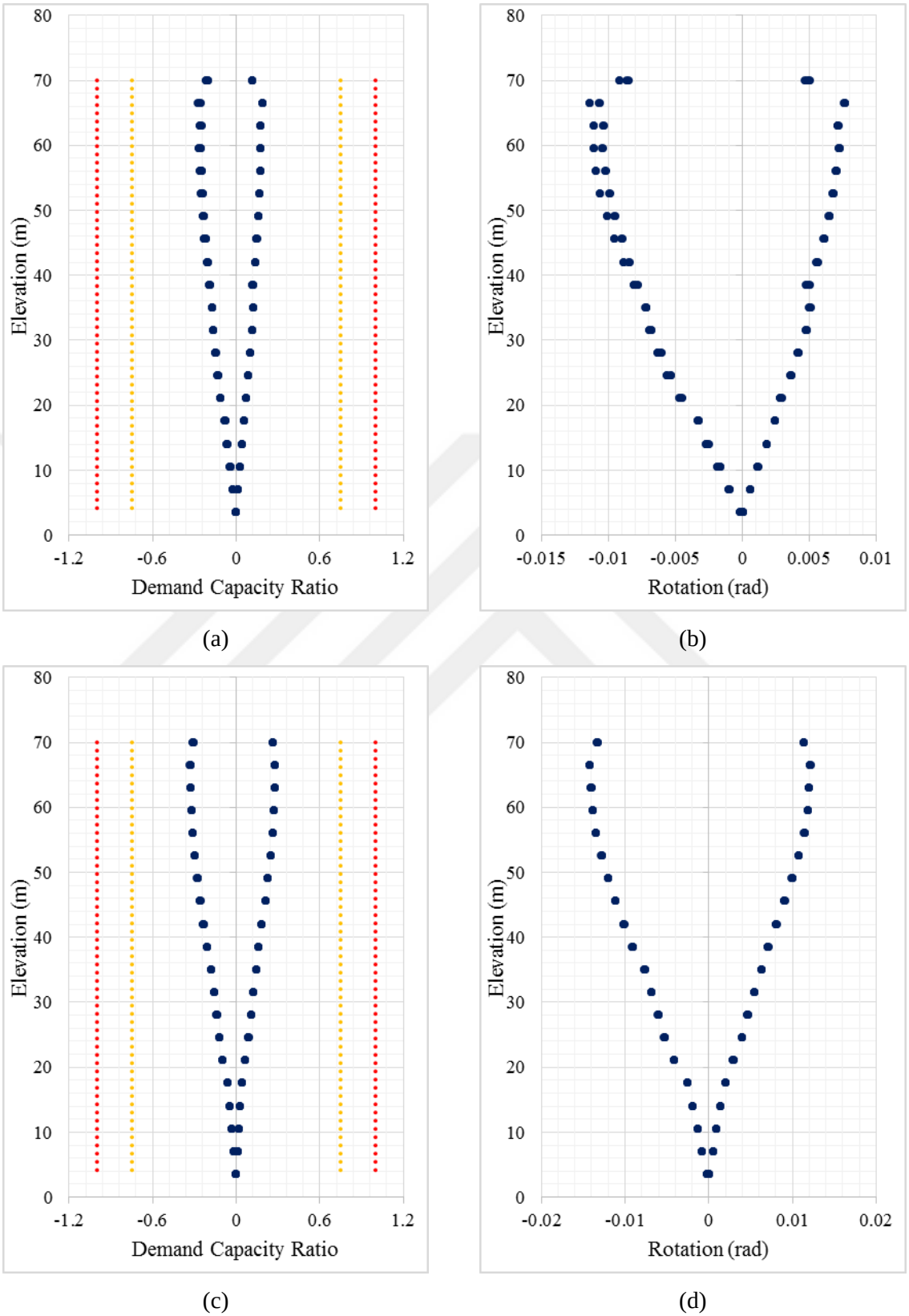

Figure 5.29. Rotations and demand/capacity ratios for effective beam model 3 (a) and (b) MH03, (c) and (d) MH06, (e) and (f) MH08.

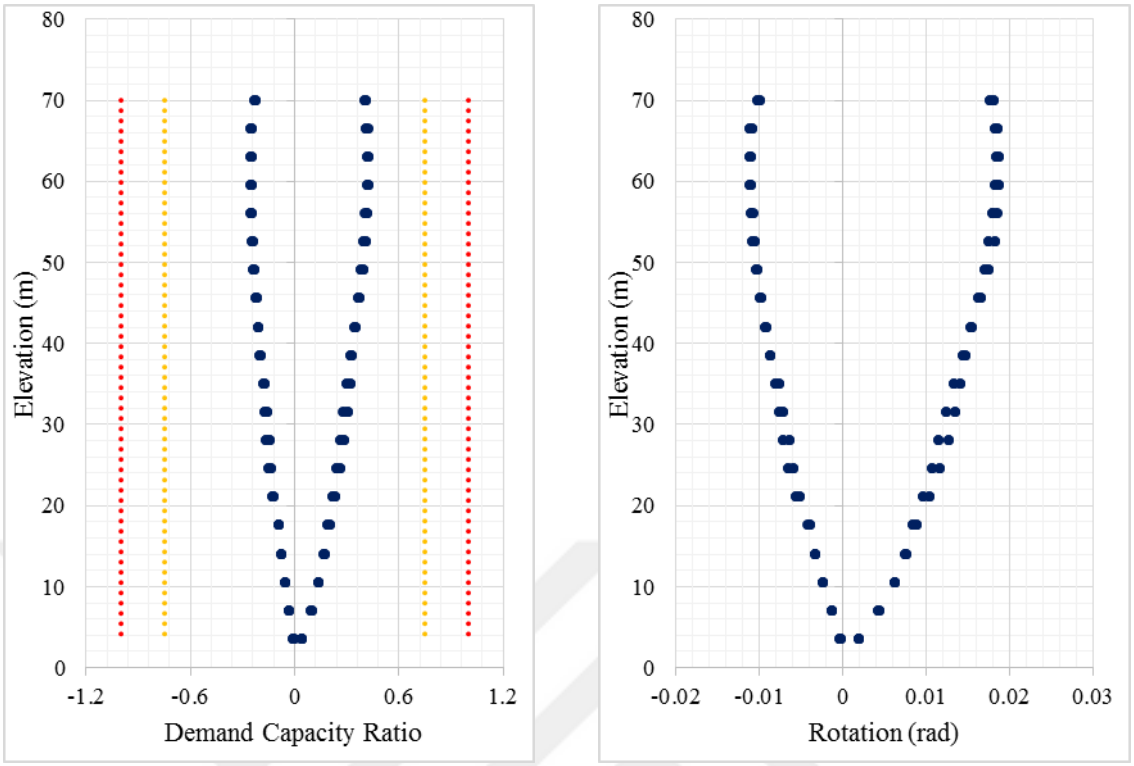

(e) (f)

Figure 5.29. Rotations and demand/capacity ratios for effective beam model 3 (a) and (b) MH03, (c) and (d) MH06, (e) and (f) MH08 (cont.).

Therefore, results obtained using the effective beam model 3 configuration ($\gamma_f = 0.6$ at edge and corner joints and *D* is considered in design) the TEC 2018 approach for designing slab-column connections provides adequate seismic performance at the connections; however, it may require unnecessary increase in the cross-sectional dimensions of edge and corner columns.

6. SUMMARY AND CONCLUSIONS

6.1. Overview

In this study, first, an equivalent shear hinge modeling approach, which is fully applicable in commercial analysis software, is proposed to simulate the nonlinear behavior of slab-column connections. Validation of the proposed model is performed with existing shake table test data and other modeling methods presented in the literature. Afterwards, a hypothetical flat plate tall building is designed using different linear elastic analysis methods and code-compliant design approaches. Using the proposed nonlinear modeling method for the slab-column connections, nonlinear models of the building are then generated, with modeling parameters and acceptance criteria that are based on ASCE 41 and TEC 2018. The first two building configurations follow the ACI 318 approach for punching shear design. In one building configuration, seismic overstrength is considered in the punching shear design, whereas it is not included in the second. The third configuration represents TEC 2018 design for punching shear, and gives bigger column cross-sectional dimensions for the edge and corner columns. Furthermore, two additional nonlinear models are generated, one with no slab elements and the second with elastic shell elements for the slabs. Nonlinear response history analyses are performed on all five building configurations using CSI Perform 3D analysis software. Seismic performance of building configurations is evaluated based on the analysis results, with emphasis on the performance of the slab-column connections that were designed using different approaches

6.2. Conclusion

Based on the linear and nonlinear analysis results obtained from various analytical models, main conclusions that can be reached are listed below:

- The proposed equivalent shear hinge model to replace a torsional hinge in the commercial analysis software has been shown to be a successful and effective approach to simulate the nonlinear behavior of slab-column connections towards improving the performance evaluation of the entire structural system.

- Different analysis methods, including the finite element method, eccentric shear stress method, and ACI 318 empirical method (Equation 2.13), provide almost the same results for punching shear design at interior slab-column connections.

- Story drifts obtained for the building modeled using effective beam models for the slabs are smaller than the model with an elastic slab with a flexural stiffness modifier of 0.25. This is partly because linear elastic slab elements in CSI Perform 3D does not transfer bending moments to structural walls elements in the strong direction of the walls. Excluding the slabs from analytical model naturally tends to give larger drift ratios. It may be concluded that for tall buildings with core walls, using linear elastic and cracked shell elements for the slabs is suitable for story drift checks.

- Design based on TEC 2018 and design according to ACI 318 with included overstrength factor in punching shear design of slabs give similar nonlinear deformation (rotation) levels at slab-column connections. Obtained plastic rotations are around 0.01 radians for the interior connections, around 0.012 radians for the edge connections, and around 0.015 radians for corner connections, which plastic rotation demand-to-capacity ratios of around 25%, 30% and 33% respectively. Overall acceptable results, which exceed rotation limits 20% in some of the corner joints, are obtained from the design that complies with ACI 318 (with overstrength neglected in design of slabs). Interior connections that are adjacent to a wall in the strong direction undergo more plastic rotations than interior connections that are in-between other columns.

- Models with natural periods from largest to smallest values are the no-shell model, elastic shell model, and effective (nonlinear) beam model. However, shear forces developing in structural walls do not follow a consistent (opposite) trend with the natural periods ($V_{noshell} < V_{effbeams} < V_{shell}$). Shear forces resisted by structural walls in the effective beam models are smaller than shell models because slab-column connections in effective beam models work as frame assemblies and help reduce the shear force demands on the structural walls.

6.3. Future Recommendations

The following recommendations can be made for future studies related with the scope of this thesis:

- Result of the thesis can be generalized by applying the methodology to the other building configurations with different floor plans and number of stories.

- Taking $\gamma_f = 1$ is suggested for edge and corner slab-column connections in design process if satisfies required conditions.

- More studies need to be conducted about necessity of applying overstrength factor (D) in the punching shear design.

REFERENCES

Allen, F., and P. Darvall, 1977, "Lateral Load Equivalent Frame", *ACI Journal*, Vol. 74, No. 7, pp. 294-298.

ACI Committee 318, 2015, *Building Code Requirements for Structural Concrete (ACI 318M-14) and Commentary (ACI 318RM-14)*, American Concrete Institute, Farmington Hills, MI.

Applied Technology Council, 2010, *Modeling and Acceptance Criteria for Seismic Design and Analysis of Tall Buildings (ATC 72-1)*, Pacific Earthquake Engineering Research Center, Redwood City, California.

ASCE/SEI, 2017, *Seismic Evaluation and Retrofit of Existing Buildings (ASCE/SEI 41-17)*, American Society of Civil Engineers, Reston, VA.

CSI Etabs Ultimate v16.2.1., 2017, Integrated Building Design Software, Computers and Structures, Inc, California, USA.

CSI Perform 3D V7.0.0., 2018, Nonlinear Analysis and Performance Assessment for 3D Structures, Computer and Structures, Inc., California, USA.

Disaster and Emergency Management Presidency, 2018, *Turkish Earthquake Hazard Map*, https://tdth.afad.gov.tr, accessed in January 2019.

Elwood, K. J., A. B. Matamoros, J. W. Wallace, D. E. Lehman, J. A. Heintz, A. D. Mitchell, M. A. Moore, M. T. Valley, L. N. Lowes, C. D. Comartin, and J. P. Moehle, 2007, "Update to ASCE/SEI 41 Concrete Provisions", *Earthquake Spectra*, Vol. 23, No. 3, pp. 493-523.

Hanson, N. W., and J. M Hanson, 1968, "Shear and Moment Transfer between Concrete Slabs and Columns", *Journal of the PCA Research and Development Laboratories,* Vol. 10, No. 1, pp. 2-16.

Hwang, S. J., and J. P. Moehle, 2000, "Models for Laterally Load Slab-Column Frames", *ACI Structural Journal,* Vol. 97, No. 2, pp. 345-353.

Hwang, S. J., and J. P. Moehle, 2000a, "Vertical and Lateral Load Tests of a Nine-Panel Flat-Plate Frames", *ACI Structural Journal,* Vol. 97, No. 1, pp. 193-210.

Kang, T. H. K., 2004, *Shake Table Tests and Analytical Studies of Reinforced and Post-Tensioned Concrete Flat Plate Frames,* Ph. D Thesis, University of California.

Kang, T. H. K., and J. W. Wallace, 2006, "Punching of Reinforced and Post-Tensioned Concrete Slab-Column Connections", *ACI Structural Journal,* Vol. 103, No. 4, pp. 531-540.

Kang, T. H. K., J. W. Wallace and K. J. Elwood, 2009, "Nonlinear Modeling of Flat-Plate Systems", *ASCE Journal of Structural Engineering,* Vol. 135, No. 2, pp. 147-158.

Los Angeles Tall Buildings Structural Design Council, 2015, *An Alternative Procedure for Seismic Analysis and Design of Tall Buildings Located in the Los Angeles Region*, Los Angeles Tall Buildings Structural Design Council, California.

Mander, J. B., M. J. N. Priestley, and R. Park, 1988, "Theoretical Stress-Strain Model for Confined Concrete", *ASCE Journal of Structural Engineering,* Vol. 114, No. 8, pp. 1804-1826.

Moehle, J., 2015, *Seismic Design of Reinforced Concrete Buildings,* McGraw-Hill Education.

Pasific Earthquake Engineering Research Center, 2010, *Guidelines for Performance-Based Seismic Design of Tall Buildings*, Report PEER-2010/05, Pasific Earthquake Engineering Research Center, University of California.

Pasific Earthquake Engineering Research Center, 2013, *Next Generation Attenuation-West2*, https://ngawest2.berkeley.edu, accessed in March 2019.

The Council on Tall Buildings and Urban Habitat, 2008, *Recommendations for the Design of High-Rise Buildings*, The Council on Tall Buildings and Urban Habitat, Chicago.

Turkish Earthquake Code, 2018, *Specifications for Structures to be Built in Disaster Areas*, Disaster and Emergency Management Presidency, Ankara.

Turkish Standards Institute, 1997, *Design Loads for Buildings (TS 498)*, Turkish Standards Institute, Ankara.

Turkish Standards Institute, 2000, *Requirements for Design and Construction of Reinforced Concrete Structure (TS 500)*, Turkish Standards Institute, Ankara.

Turkish Standards Institute, 2009, *Design of Concrete Structures-Part 1-1: General Rules and Rules for Buildings (TS EN 1992-1-1)*, Turkish Standards Institute, Ankara.

Stasio, J. D., and M. R. V. Buren, 1960, "Transfer of Bending Moment between Flat Plate Floor and Column", *ACI Structural Journal*, Vol. 57, No. 3, pp. 299-314.